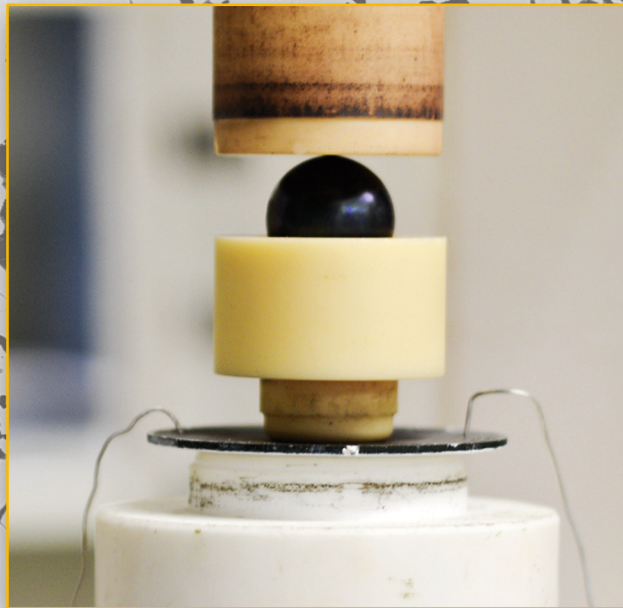


# Mechanical and Thermochemical Properties of Nano-structured Membranes for Gas Separation in Fossil-fired Power Plants

Jizu Zhang



Energie & Umwelt/  
Energy & Environment  
Band/ Volume 311  
ISBN 978-3-95806-126-2





Forschungszentrum Jülich GmbH  
Institute of Energy and Climate Research (IEK)  
Microstructure and Properties of Materials (IEK-2)

# Mechanical and Thermochemical Properties of Nano-structured Membranes for Gas Separation in Fossil-fired Power Plants

Jizu Zhang

Schriften des Forschungszentrums Jülich  
Reihe Energie & Umwelt / Energy & Environment

Band / Volume 311

---

ISSN 1866-1793

ISBN 978-3-95806-126-2

Bibliographic information published by the Deutsche Nationalbibliothek.  
The Deutsche Nationalbibliothek lists this publication in the Deutsche  
Nationalbibliografie; detailed bibliographic data are available in the  
Internet at <http://dnb.d-nb.de>.

Publisher and  
Distributor: Forschungszentrum Jülich GmbH  
Zentralbibliothek  
52425 Jülich  
Tel: +49 2461 61-5368  
Fax: +49 2461 61-6103  
Email: [zb-publikation@fz-juelich.de](mailto:zb-publikation@fz-juelich.de)  
[www.fz-juelich.de/zb](http://www.fz-juelich.de/zb)

Cover Design: Grafische Medien, Forschungszentrum Jülich GmbH

Printer: Grafische Medien, Forschungszentrum Jülich GmbH

Copyright: Forschungszentrum Jülich 2016

Schriften des Forschungszentrums Jülich  
Reihe Energie & Umwelt / Energy & Environment, Band / Volume 311

ISSN 1866-1793  
ISBN 978-3-95806-126-2

The complete volume is freely available on the Internet on the Jülicher Open Access Server (JuSER)  
at [www.fz-juelich.de/zb/openaccess](http://www.fz-juelich.de/zb/openaccess).

Neither this book nor any part of it may be reproduced or transmitted in any form or by any  
means, electronic or mechanical, including photocopying, microfilming, and recording, or by any  
information storage and retrieval system, without permission in writing from the publisher.

## Kurzfassung

Mechanische und thermochemische Eigenschaften nanostrukturierter poröser SiO<sub>2</sub>-Membranen mit keramischem und metallischem Substrat wurden zur Anwendung für die CO<sub>2</sub>-Abtrennung im Pre-Combustion-System in fossil gefeuerten Kraftwerken untersucht.

Da die dünne Membranschicht ein mechanisch robustes Substratmaterial erfordert, wurden Materialien aus Alumina als vielversprechendste Substrate mit unterschiedlicher Porosität und Porengrößen in Bezug auf die mechanischen Eigenschaften charakterisiert. In der asymmetrischen Gastrennmembran, sollte die Porosität des Substrats so hoch wie möglich sein, um dessen Widerstand gegen die Permeation zu minimieren. Jedoch resultiert die Erhöhung der Porosität in der Regel in einem reduzierten Young-Modul und Bruchfestigkeit des Substratmaterials. In der vorliegenden Arbeit wurden zwei Alumina Substrattypen mit ähnlicher Porosität, jedoch jeweils mikroporöser bzw. nanoporöser Mikrostruktur untersucht, um den Einfluss der Porengröße auf die mechanischen Eigenschaften zu bestimmen.

Als alternatives Substratmaterial wurde ein poröses metallisches Intermediate-Temperatur-Metall (ITM), beschichtet mit  $\gamma$ -Al<sub>2</sub>O<sub>3</sub>-Zwischenschicht und funktioneller SiO<sub>2</sub>-Membran, im Hinblick auf seine mechanischen Eigenschaften untersucht. Dabei wurde ein Schallemissionstest zur Bestimmung des Zusammenhangs zwischen Verformungs- Versagensverhalten dieser Verbundmembran adaptiert.

Ein weiterer Schwerpunkt der Arbeit war die Messung der Membran- Permeabilität hinsichtlich verschiedener SiO<sub>2</sub>-Membran und amino-modifizierter SiO<sub>2</sub>-Membran, jeweils für Einzelgas, binäres Mischgas und binäres Mischgas mit Wasserdampf. Dabei wurde der Gastransportmechanismus anhand von Permeationstests mit Einzelgas untersucht. Die Anwendung der Membranen im Rauchgas wurde durch die Permeationstests mit binärem Mischgas und Wasserdampf simuliert. Dabei wurde die verbesserte Affinität von CO<sub>2</sub> im Fall der amino-modifizierten SiO<sub>2</sub>-Membranen auch unter Bedingungen mit und ohne Wasserdampf anhand von Auslagerungsversuchen und Infrarotspektroskopie analysiert.

Des Weiteren wurde der Einfluss von mechanischer Vorverformung auf das Membransystem anhand von Permeationstests untersucht, dabei erlaubte ein Vergleich mit den Permeationsergebnissen einer entsprechenden unverformten Proben mit metallischem Substrat Rückschlüsse auf die Änderung des Gastransportmechanismus.



## Abstract

The mechanical and thermochemical properties of nano-structured porous SiO<sub>2</sub>-membrane layers with porous ceramic and metallic substrates were studied aiming at their applications for the carbon dioxide separation in the pre-combustion systems in fossil-fired power plants.

Since the thin membrane layers demand a mechanically robust substrate material, alumina materials as promising substrates with different porosity and pore sizes were characterized with respect to their mechanical properties. In the asymmetric gas separation membrane, the porosity of the substrate should be maximized in order to minimize its resistance against permeate gas. However, an increase in porosity usually reduces Young's moduli and fracture stress of the substrate material. In this study, two types of alumina substrate materials with similar porosity but micro-porous and nano-porous microstructure, respectively, were investigated in order to assess the influence of the pore size on mechanical properties.

As an alternative substrate material, porous metallic Intermediate Temperature Metal (ITM) coated with  $\gamma$ -Al<sub>2</sub>O<sub>3</sub> interlayer and functional SiO<sub>2</sub>-membrane was also investigated with respect to its mechanical properties. An acoustic emission test was adopted to determine the correlation deformation- failure behaviour of this composite membrane system.

Another focus of the work was a determination of the gas permeability of various gases through SiO<sub>2</sub> and amino-modified SiO<sub>2</sub> membranes, in which the adopted gas systems were single gas, binary gas mixtures and binary gas mixtures plus water vapour. The gas transport mechanism was investigated via the single gas permeation tests. The application of membranes in the flue gas was simulated by permeation tests with binary gas mixture plus water vapour. Meanwhile, the enhanced affinity of CO<sub>2</sub> towards amino-modified SiO<sub>2</sub>-membranes with and without water vapour was also investigated via annealing tests and infrared spectroscopy.

Furthermore, the effect of mechanical pre-deformation onto the membrane system was also investigated via the permeation tests. A change of gas transport mechanism through the membranes was analysed by comparing the permeation results of non-deformed and pre-deformed specimens with metallic substrate.



---

## Contents

1	Introduction .....	1
2	Scope of work.....	3
3	Fundamentals.....	5
3.1	CO <sub>2</sub> capture and storage technologies (CCS).....	5
3.1.1	Pre- combustion process.....	5
3.1.2	Oxyfuel process .....	6
3.1.3	Post-combustion process .....	8
3.2	Membrane technology for gas separation .....	9
3.2.1	Membranes .....	9
3.2.2	Requirements for membranes .....	10
3.2.3	Characteristics .....	12
3.2.4	Mechanism of gas separation and transport.....	12
3.3	Porous membranes .....	16
3.3.1	Structure of porous membrane.....	16
3.3.2	Porous silica membranes .....	18
3.3.3	Porous silica membranes modified with amino-group .....	18
3.3.4	Synthesis of porous silica membranes.....	19
3.3.5	Degradation of silica membrane with water vapour .....	23
4	Literature review of investigated materials' properties.....	25
4.1	Substrate.....	25
4.1.1	Ceramic substrate – porous $\alpha$ -Al <sub>2</sub> O <sub>3</sub> .....	25
4.1.2	Metallic substrate – porous ITM (Intermediate temperature metal).....	27
4.2	Membrane .....	28
4.2.1	Porous silica membrane.....	28
4.2.2	Amino-modified silica membrane .....	29
5	Materials and experimental methods.....	31
5.1	Characterization of membranes with different substrates .....	31
5.1.1	Membranes with Atech substrate .....	31
5.1.2	Membranes with IEK-1 substrate .....	32
5.1.3	Membranes with metallic ITM substrate.....	33
5.1.4	Mercury porosimetry .....	34
5.2	Determination of membrane permeability .....	35
5.2.1	Setup of single gas permeation tests.....	35
5.2.2	Set-up of mixed gas permeation tests .....	35

5.2.3	Performance of permeation measurements.....	41
5.3	Thermal stability evaluation.....	42
5.4	Determination of mechanical properties .....	44
5.4.1	Ring-on-ring bending test.....	44
5.4.2	Acoustic emission test.....	47
5.4.3	Indentation test.....	49
5.5	Microstructure identification.....	50
5.5.1	Scanning electron microscopy (SEM).....	50
5.5.2	Infrared spectroscopy .....	51
6	Results and discussion.....	53
6.1	Characterization of membranes with different substrates .....	53
6.1.1	SiO <sub>2</sub> -membrane with ceramic Atech substrate .....	53
6.1.2	SiO <sub>2</sub> -membrane with ceramic IEK-1 substrate.....	53
6.1.3	SiO <sub>2</sub> -membrane with metallic ITM substrate .....	54
6.1.4	Porosity of Atech substrate and IEK-1 substrate.....	55
6.2	Mechanical properties .....	56
6.2.1	Mechanical properties of porous ceramic substrates .....	56
6.2.2	Mechanical properties of porous metallic substrate .....	70
6.3	Permeability .....	79
6.3.1	SiO <sub>2</sub> -membrane on ceramic Atech substrate .....	79
6.3.2	SiO <sub>2</sub> -membrane with ceramic IEK-1 substrate.....	81
6.3.3	Amino-modified SiO <sub>2</sub> -membrane on ceramic IEK-1 substrate.....	91
6.3.4	Permeability of SiO <sub>2</sub> -membrane on porous metal substrates .....	98
6.4	Thermochemical stability.....	101
6.4.1	SiO <sub>2</sub> -membrane with ceramic Atech substrate and ceramic IEK-1 substrate.	101
6.4.2	Amino-modified SiO <sub>2</sub> -membrane with ceramic IEK-1 substrate.....	104
7	Conclusions .....	109
	References .....	111
	Symbol index.....	123
	Figure index.....	127
	Table index.....	131
	Acknowledgements .....	133





# 1 Introduction

Global warming is nowadays a serious issue induced by increasing greenhouse gas concentration in the atmosphere. In order to control associated greenhouse effects, the emission of carbon dioxide, which is a major greenhouse gas, should be limited. This led to the signing of the Kyoto protocol by which it was committed to reduce greenhouse gas emissions worldwide and since 1997 it has been ratified by more than 170 countries [1].

Meanwhile, it has been estimated in a scenario of the International Energy Agency (IEA) that the world primary energy consumption will increase by more than 50 % by 2030 [2], obviously enlarging the worldwide demand for electrical energy.

To meet this growing electricity demand, additional power plant capacity predicted to be more than 2,000 GW in 2020 is required. But only a limited amount of the additional energy can be supplied by the regenerative energy, requiring continuation of the usage of fossil energy sources, which are the main sources of CO<sub>2</sub> emission and on the other side support currently 60 % of the world's electrical energy demand [3]. The predicted rising energy demand will lead to an increased greenhouse gas emissions [4]. In order to satisfy the necessary energy requirements, in accordance with climate policy, the emission of CO<sub>2</sub> must be reduced in an effective way. This raises the necessity to improve existing power plant technology and to enhance requirements for future power plant designs.

There are two principles that should be followed [5]: first, is to convert the fossil fuels more efficiently and second, to put an emphasis on CO<sub>2</sub> capture i.e. there are many technologies developed for gas separation, which are mainly based on three processes: pre-combustion, oxyfuel process and post-combustion.

The pre-combustion is based on gasification of carbon with air or oxygen and CO<sub>2</sub> removal from the synthetic gas. After the burning with pure oxygen a CO<sub>2</sub> rich flue gas is produced. Water vapour in the flue gas is condensed. Finally the CO<sub>2</sub> rich gas will be liquefied [6, 7].

Through oxyfuel combustion, the nitrogen is removed from air before combustion and the fuel is combusted in pure oxygen rather than air. This technology can enhance the efficiency of combustion significantly. The further advantage of oxyfuel combustion is substantial reduction of NO<sub>x</sub> emissions [8].

In post-combustion process the CO<sub>2</sub> is extracted from the exhaust gas of a traditional fossil power plant. A typical process for CO<sub>2</sub> capture in the chemical industry is amine wash. But

this method results in an increased power plant efficiency loss from 8.2 % to 14 % [6, 7]. Moreover, it requires massive consumption of toxic chemicals. Hence, the substitution via a membrane technology has potentially many advantages with respect to energy efficiency arrangement and environmental friendliness.

Although, as one candidate, polymer membranes proved to have promising separation properties, polymer membranes exhibit chemical instabilities above 100 °C and can be damaged irreversibly. Therefore, as alternative, ceramic membranes have been considered, which have a high thermal and chemical stability [9]. Additionally, it is necessary to deposit the ceramic membrane on the ceramic or metal substrate in order to build an asymmetric structure with support of sufficient mechanical strength. Hence, in addition to a careful assessment of permeation properties, asymmetric membranes require also a consideration of mechanical aspects of layers and supports. In the current study, the mechanical behaviour and thermochemical properties of the selected materials were investigated to assess their suitability for future application in the fossil power plants.

## 2 Scope of work

The main aim of this work is to determine mechanical properties and permeability of micro-porous SiO<sub>2</sub> membranes on either porous ceramic and metal substrates, which are promising for the application in the CO<sub>2</sub> separation in the post-combustion process [10]. Since the thickness should be as thin as possible to increase the gas transport in advanced membrane designs, thin layers need to be deposited on porous substrates that act as mechanical support. In this study,  $\alpha$ -Al<sub>2</sub>O<sub>3</sub> ceramic and ITM (Intermediate- Temperature- Metal) metallic substrates have been chosen as the promising porous supports, hence in addition to the permeation properties of the layer, the mechanical properties of the substrates are highly relevant, i.e. the substrate should have in particular a high fracture or yield strength in the case of ceramic or metallic materials, respectively.

As main aspect for the application, permeability and selectivity of the membranes for CO<sub>2</sub> should be sufficient. Therefore, single-gas and mixed-gas tests focused on a determination of the gas separation mechanism of porous SiO<sub>2</sub> membranes. In addition, thermochemical properties of the membrane were considered, which are important for the long term stability, especially at elevated temperatures in the presence of water vapour, which might induce changes of the pore structure of the silica membranes. This can eventually result in permeation of other gases through the membrane and therefore affect the selectivity.

However, one aspect of this work was also the evaluation of the mechanical behaviour of the selected substrate materials by biaxial bending tests. Furthermore, the bonding between substrate and membrane coating system, which consists of interlayers and function layer, should be sufficient, especially during deformation induced by gas pressure differences between feed and sweep side. This aspect has been analysed micro-mechanically by indentation testing.

Bearing in mind the different deformation and failure behaviour of metal and ceramic, the impact of deformation of the whole membrane system with porous metallic substrate on the gas separation property was assessed by a comparison of the permeation and selectivity before and after pre-deformation.

This work was carried out within the framework of the project Metpore II “nano-structured, metal-supported ceramic membranes for gas separation in fossil power plants”, financially supported by German Federal Ministry for Economy Affairs and Technology (BMWi).



### 3 Fundamentals

#### 3.1 CO<sub>2</sub> capture and storage technologies (CCS)

The main reason for the global warming appears to be related to greenhouse gases, e.g. carbon dioxide CO<sub>2</sub> and methane CH<sub>4</sub>. The continuing emission of such gases will lead to an enhancement of the greenhouse effect. Here, CO<sub>2</sub> is particularly critical since it contributes to the greenhouse effect by up to 80% [11]. Almost 30% of CO<sub>2</sub> is emitted from fossil power plants [12]. Therefore, in future fossil power plant design, large scale application of CO<sub>2</sub> capture and storage (CCS) technologies can contribute to the protection of the environment. The purpose of CO<sub>2</sub> capture is to produce a highly concentrated gas stream of CO<sub>2</sub> that can be transported economically to storage sites. For this purpose, three main processes can be implemented: pre-combustion, oxyfuel and post-combustion [13].

##### 3.1.1 Pre-combustion process

The principle of the pre-combustion process is based on the formation of CO<sub>2</sub> from the fossil energy carrier and the subsequently separation of CO<sub>2</sub> before combustion (Fig. 1). The fossil fuel is first gasified under a high pressure of 65 bar [14] and sub-stoichiometric amount of air synthesizing a gas mixture composed of CO and H<sub>2</sub>. Then the stream is passed through a series of catalyst beds. In the CO-shift-reaction with water vapour, the CO is converted to CO<sub>2</sub>.

The produced CO<sub>2</sub> is separated from the gas mixture with H<sub>2</sub>. Therefore, mainly H<sub>2</sub> remains in the fuel gas for the following combustion and finally the CO<sub>2</sub> free exhaust gas can directly be emitted into the environment [14].

Traditionally, most CO<sub>2</sub> separation technologies related to the pre-combustion process are based on the use of solvents, i.e. chemical and physical solvents [15]. More than 90% of the CO<sub>2</sub> gas can be removed with such solvents, especially with physical solvents which are typically used for such separation procedures, where, at elevated temperatures, CO<sub>2</sub> is dissolved in the solvent. When the external conditions are changed, e.g. via increasing the temperature or decreasing pressure, the CO<sub>2</sub> will be released from this sorbent. The advantage of this separation procedure by physical solvents is the possibility of recycling of the solvents without additional high consumption of energy, compared to the post-combustion process. Among the physical solvents, the process based on methanol was found to have the most promising performances in terms of energy penalty (reduction in the power stations electrical efficiency) [16]. Compared to CO<sub>2</sub> capture solvents, membranes appear to be more

economical in cases where the  $\text{CO}_2$  concentration is high enough in the gas [17]. Amelio et al. compared the pre-combustion process based on classical  $\text{CO}_2$  adsorption removal with innovative membrane separation technologies [18]. In this work, several options of membrane technologies considering  $\text{CO}_2/\text{H}_2$  separation with amine-containing membranes [19], membranes containing potassium carbonate-glycerol [20], dendrimer-containing membranes [21] etc., are described.

However, the pre-combustion process leads to high production costs and additional efficiency losses not only related to the shift reaction but due to the capture process. In spite of the disadvantages, the pre-combustion process produces a high concentration and pressurized  $\text{CO}_2$ , being the advantage of this separation procedure [17].

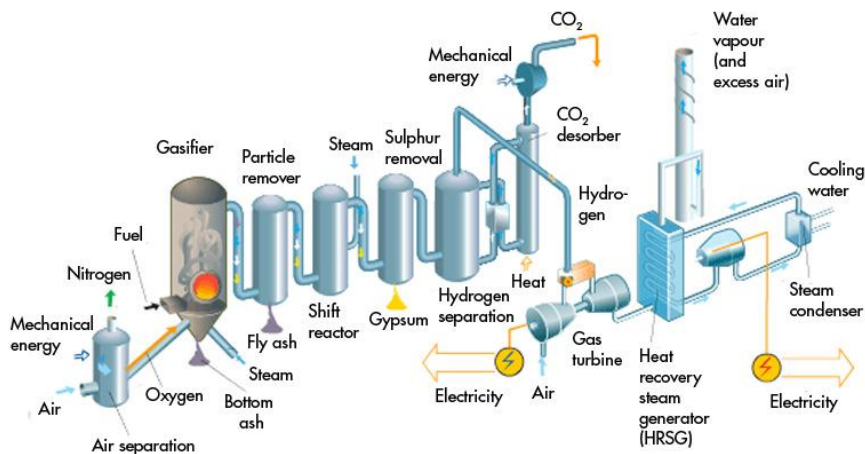


Fig. 1 Schematic diagram of a power plant with the pre-combustion process (Source: Vattenfall).

### 3.1.2 Oxyfuel process

In the oxyfuel process, fossil fuel is combusted in an oxygen rich atmosphere which is produced from the air and therefore the exhaust gas contains mainly  $\text{CO}_2$  and water vapour. Through this technology, the fuel gases cannot be diluted by nitrogen, which is supplied with the air in conventional combustion processes. Hence, the partial pressure of  $\text{CO}_2$  is significantly increased in the exhaust gas, leading to three advantages. First, the driving force for  $\text{CO}_2$  separation can be increased and therefore the carbon capture process can be facilitated. Second, the energy consumption for  $\text{CO}_2$  capture is lower than that for removal of nitrogen from the exhaust gases. Third, because of the larger thermal capacity of  $\text{CO}_2$  and

water vapour compared to nitrogen, heat transfer in the convective section of the boiler is significantly increased [22]. Considering efficiency and costs, the oxyfuel process appears to be competitive with amine-based post-combustion [15].

A schematic diagram of a fuel-fired oxyfuel boiler is shown in Fig. 2. After combustion, the  $\text{CO}_2$  content is about 75 % in the wet exhaust gas. The  $\text{CO}_2$  content can subsequently reach 80-90 % after condensation of water vapour from the flue gas and subsequent separation from the mixture. Other gases such as nitrogen and sulphur produced from combustion must be removed in the flue gases in a washing process in a conventional fossil-fired power plant [13].

However, several aspects should be taken into account with respect to the oxyfuel process and parameters related to  $\text{CO}_2$  capture rate in order to optimize the purity of oxygen in the boiler and of the  $\text{CO}_2$  product. Air separation units can supply the oxygen with a purity of 95-99 % in most current oxyfuel process designs, due to the good oxygen permeability and low efficiency losses of oxygen transport membranes in the temperature range 800 to 1000 °C [23, 24]. But air separation units require additional energy, which leads to a net efficiency loss of the power plant. Furthermore, this technique also requires the solution of problems related to the impact of dust, steam and degradation of membranes [17, 24].

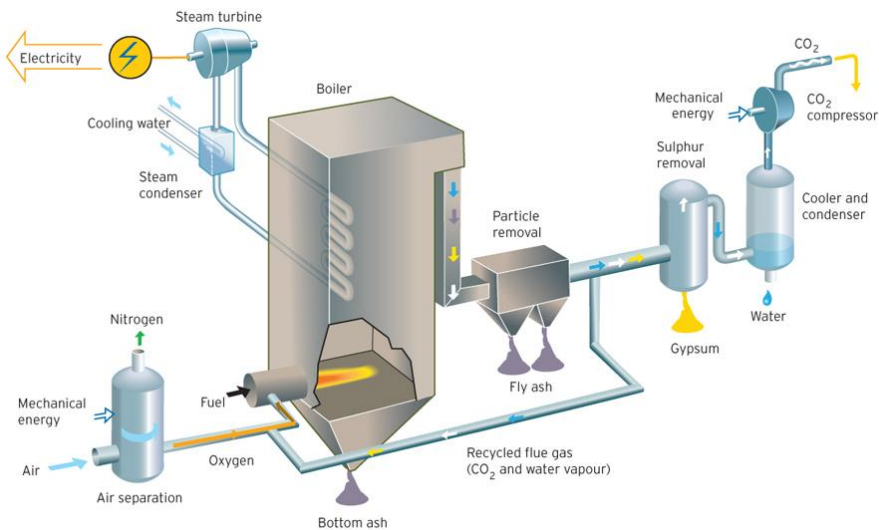


Fig. 2 Schematic diagram of a power plant with oxyfuel process (Source: Vattenfall).

### 3.1.3 Post-combustion process

In the post-combustion process, the CO<sub>2</sub> is separated from the flue gas of conventional power plants. The process is shown schematically in Fig. 3. The heat energy produced during the combustion of the fossil energy carrier with air is used to generate water vapour. The hot water vapour drives the gas turbine, which generates subsequently electrical current. The flue gas produced in the combustion process is transferred into the environment after the corresponding cleaning, which consists of three steps, i.e. denitrification, dedusting and desulfurization [25].

**Denitrification:** Reduction of nitric oxide can be realized through a firing procedure [26, 27] as well as by post-denitrification. In the case of post-denitrification the nitric oxide is converted with ammonia using catalysis into water and nitrogen. A typical catalyser is mostly titan oxide with additives from the compounds of vanadium, tungsten and molybdenum additives [28].

**Dedusting:** The separation of dust can be realized through mechanical or electrical method. In an electrical process the dust particles are charged and therefore can be extracted at the negative electrode [25].

**Desulfurization:** The desulfurization process is implemented in a wash tower. The flue gas, which has been cooled down is sprayed into the lime solution. The sulphur oxide is dissolved in the solvent and turned into calcium sulphite. With air injection, calcium sulphite that is accruing in the lower part of solvent, is converted to calcium sulphite dehydrate [28].

The aim of the post-combustion process is an enrichment of CO<sub>2</sub> from a relatively low content of 5-15 % [29, 30] towards a CO<sub>2</sub> stream with high purity. One of the post-combustion process's advantages is that it can be in principle retrofitted to any existing power plant without substantial change of the basic set-up. Until now, chemical sorption methods with alkyl ammonia solvents, e.g. mono-ethane-amine-based, are still the most widely used implementation of the post-combustion CO<sub>2</sub> separation process. In this ammonia washing, the flue gas is transferred into the liquid solvent at temperatures between 40 and 65 °C [28]. CO<sub>2</sub> is absorbed by a reversible combination with the amino group in the solvent. Desorption occurs when the temperature of the water vapour stripping the combined CO<sub>2</sub> reaches between 100 and 120 °C. The washing solvent can be recycled after regeneration. However, this chemical process requires a large amount of energy to regenerate the solvent. The consumption of the energy for this process is about 80 % of the total process amount [22].

Membrane based set-ups seem to be suitable to improve the post-combustion process [31]. However, no special improvement in the energy efficiency of the overall power plant process can be achieved through this approach. Nevertheless, with the purpose of replacing the traditional gas-liquid absorption process, techniques based on membrane separation are currently under development [32].

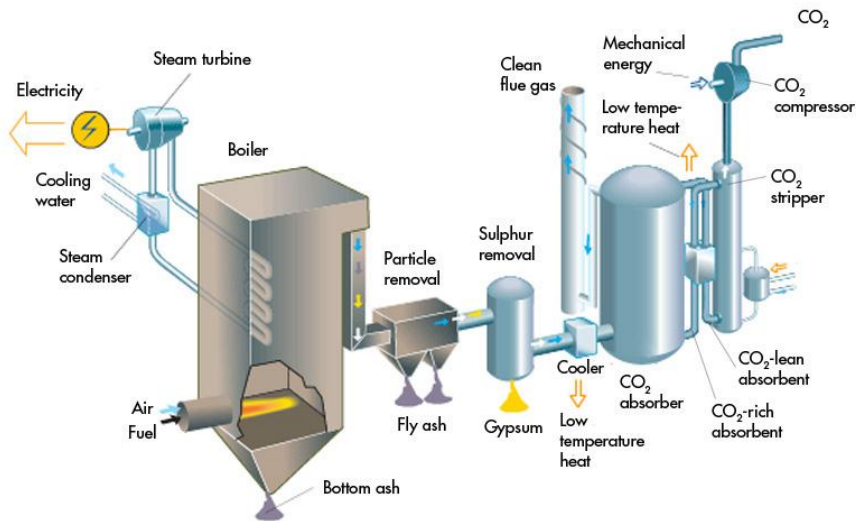


Fig. 3 Schematic diagram of a power plant with the post-combustion process (Source: Vattenfall).

## 3.2 Membrane technology for gas separation

### 3.2.1 Membranes

One of the first industrial applications of ceramic membranes was realized in the separation of different uranium isotopes via Knudsen diffusion [33]. Because the separation factor of the gaseous isotopes  $^{235}\text{UF}_6$  and  $^{238}\text{UF}_6$  was only 1.0064, multiple of separation units had to be connected in series. This cascading required high energy consumption and hence could only be implemented for military interest.

To increase gas separation efficiency micro-porous membranes have been developed over recent years [34]. The operation is based essentially on the size exclusion of gas molecules, which can lead to apparently high separation effects. Today membranes can be found in the application for the separation of smaller gas molecules such as in hydrogen production from natural gas or for the separation of helium and nitrogen [35].

Generally, a membrane can be seen as a semi-permeable layer and also be considered as a barrier between two phases [33, 36]. In a separation process, the membrane is located between feed and permeate. Typically micro-porous membranes are rather thin and deposited on a porous substrate. The free surface of the membrane faces feed side for sealing reasons. A driving force is required so that the component in the feed mixture to be separated passes through the membrane. This driving force depends on the environmental conditions and can be differences in temperature, pressure, concentration or electric fields that exist between each of the phases. In the case of gas separation using porous membranes, a pressure gradient is preferred as driving force rather than a concentration gradient [33].

In separation processes there are principally two membrane assemblies named dead-end and cross-flow respectively [37]. Contrary to the cross-flow method, only the permeate component can leave the module in the dead-end method. Hence, the retentate collected on the feed side must be removed by rinsing. This disadvantage of gas blocking is absent in the case of the cross-flow method, since the membrane surface is flowed over and deposition is hardly possible. However, the cross-flow has also disadvantages since the overflowing of the feed gas on the membrane surface requires also energy.

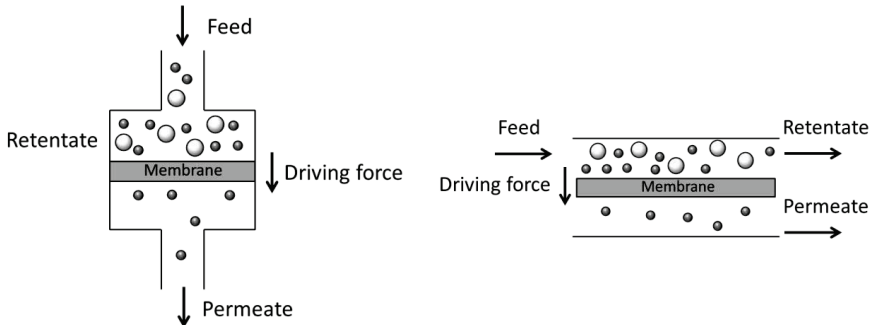


Fig. 4 Two gas separation method with membrane: Dead-end-method (left) and Cross-flow-method (right).

### 3.2.2 Requirements for membranes

For the application of membranes there are three requirements: selectivity, permeability and stability. Selectivity means the ability to separate the wanted component from the feed mixture. This characteristic factor is represented by selectivity  $\alpha$ . In the case of binary mixture selectivity  $\alpha$  can be defined through the following equation [38-40]:

$$\alpha = \frac{y_m}{x_m} \cdot \frac{y_n}{x_n} \quad \text{or} \quad \alpha = \frac{y_m}{1 - y_m} \cdot \frac{1 - x_n}{x_n} \quad (\text{Equ. 1})$$

where  $m$  and  $n$  are mixed components,  $x$  and  $y$  are the material fraction of the components in the feed and sweep mixture, respectively. The selectivity is also usually described as ideal selectivity that is calculated by quotient of a single gas permeation of both components [39]:

$$\alpha = \frac{F_m}{F_n} \quad (\text{Equ. 2})$$

where  $F_m$  and  $F_n$  [ $\text{mol}\cdot\text{s}^{-1}\cdot\text{m}^{-2}\cdot\text{bar}^{-1}$ ] are the permeation of the pure components and represent the performance of the flow rate  $J$  [ $\text{mol}\cdot\text{s}^{-1}\cdot\text{m}^{-2}$ ] normalised by pressure, according to a convention of IUPAC (International Union of Pure and Applied Chemistry) [41].

The selectivity has a higher importance, since it reflects the actual separation success and the quality of a membrane. With respect to the envisaged commercial application, it is clear that the quantitative aspect must be considered as well the qualitative aspect. From the economic point of view, the flow rates have also a large importance, since they have a direct impact onto the dimension of the necessary membrane surface area. However, both targets, selectivity and permeation, cannot be maximized simultaneously for a micro-porous membrane due to its intrinsic properties. If the pore sizes are reduced exactly to the size of the permeate component, the flow resistance increases. Consequently, an increase in the selectivity can only be achieved through smaller diffusion rates within a certain margin. This link between selectivity and permeation is exemplified in Fig. 5 [40, 42].

The stability of the membrane can be specified with respect to different aspects (e.g., chemical, thermal, hydrothermal). It determines the suitability of membranes under the intended application conditions and consequently influences the lifetime of the membrane system. For a membrane materials with lower stability, the application might be realized theoretically by changing the exposure conditions, but this would obviously is connected to a high effort and cost [4].

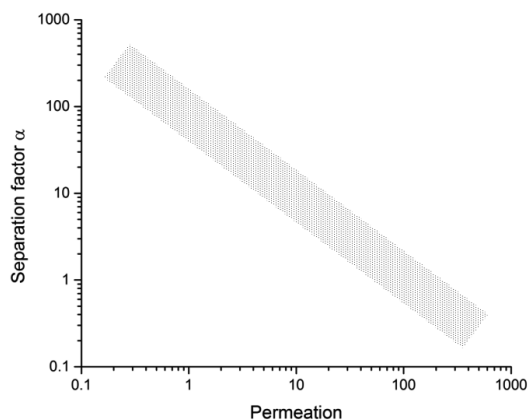


Fig. 5 Principal relationship between separation factor and permeation [42].

### 3.2.3 Characteristics

The filtration processes can be distinguished according to the size of separation medium in application. The separation principle based on the size exclusion process is achieved via pore size. For the micro-filtration the particle sizes range from 5  $\mu\text{m}$  to 100 nm. The pore size of ultra-filtration membranes is between 10 nm and 100 nm. The nano-filtration is a diversification of the separation process between ultra-filtration and reverse osmosis, since the macromolecules are in the nanometre dimension (1 to 10nm) [33]. Not only is the molecular weight significant for this separation process, but also electrical charge and valence [33].

For the gas separation high gas purity and large processing quantities are usually desired as performance indicators. For this reason, defect-free membranes are required from the production side, in order to avoid unfiltered permeates. Seals or joints placed between the membrane and set-up is another challenge to avoid accidental gas leakage [4].

### 3.2.4 Mechanism of gas separation and transport

According to the pore size, the gas permeation membranes can be divided into macro-porous membranes (diameter larger than 50 nm), meso-porous membranes (diameter between 2 nm and 50 nm) and micro-porous membranes (diameter between 0 nm and 2 nm) [33].

The gas transport through the membrane can be affected by the pore size, temperature, pressure, interaction of different gases with each other and interaction between gases and membrane surface [43]. The transport mechanism, e.g. ordinary diffusion, Knudsen diffusion, Knudsen diffusion, surface diffusion or viscous flow might overlap [41].

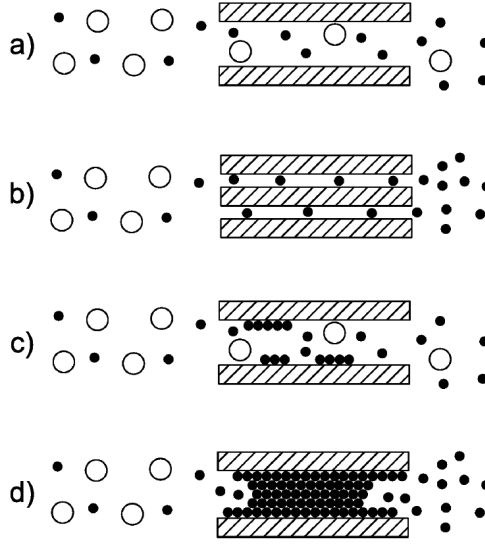


Fig. 6 Gas separation mechanism in porous membranes: a) Knudsen-diffusion, b) molecular sieving, c) surface diffusion, d) capillary condensation [9].

For the porous materials, the selectivity depends on the pore size, pore form and the kind of gas. When the pore diameter is larger than the mean free path of a gas particle, the possibility is higher that the particle collide another particle than against the pore wall [38]. If there is no wand collision, the total impulse of the molecules will remain constant. In this case ordinary diffusion or viscous flow dominates the transport through the pores. These transport mechanisms do not contribute to gas separation. This relevant transport mechanism in large pores related to a pressure difference is defined by the Hagen-Poiseuille's law. According to [38] it can be written in the form:

$$F_{viscous} = \frac{\varepsilon \cdot \mu_p \cdot \bar{r}^2}{8 \cdot R \cdot T \cdot \eta \cdot h} \cdot P_m \quad (\text{Equ. 3})$$

where  $F_{viscous}$  [ $\text{mol} \cdot \text{m}^{-2} \cdot \text{s}^{-1} \cdot \text{Pa}^{-1}$ ] is the Poiseuille permeation,  $\varepsilon$  [%] the porosity,  $\mu_p$  reciprocal sinuousness of the pores,  $\bar{r}$  [m] the modal pore radius,  $R$  [ $\text{J} \cdot \text{mol}^{-1} \cdot \text{K}$ ] the gas constant,  $T$  [K]

the absolute temperature,  $\eta$  [ $\text{N}\cdot\text{s}\cdot\text{m}^{-2}$ ] the gas viscosity,  $h$  [m] the layer thickness and  $P_m$  [Pa] the average pressure through the membrane.

When the pore size is lower than the mean free path of the molecules, the transport through the pores is dominated by the Knudsen diffusion mechanism (e.g. at 20 °C the mean free path of molecules is about 60 - 100 nm. If the pore diameter is in the range of 1 - 20 nm, Knudsen transport dominates.). Therefore, the impulse of the gas molecules increases by exchange with the pore wall [38]. This means that the different molecules are independent of each other and only affected by the thermal mobility with different tempos. This transport is defined according to [38]:

$$F_{Kn} = \frac{2 \cdot \varepsilon \cdot \mu_{Kn} \cdot \bar{v} \cdot \bar{r}}{3 \cdot R \cdot T \cdot h} \text{ with } \bar{v} = \sqrt{\frac{8 \cdot R \cdot T}{\pi \cdot M}} \quad (\text{Equ. 4})$$

where  $F_{Kn}$  [ $\text{mol}\cdot\text{m}^{-2}\cdot\text{s}^{-1}\cdot\text{Pa}^{-1}$ ] is the Knudsen permeation,  $\mu_{Kn}$  the form factor,  $\bar{v}$  [ $\text{m}\cdot\text{s}^{-1}$ ] the average molecule tempo and  $M$  [ $\text{kg}\cdot\text{mol}^{-1}$ ] the mass of gas molecules. The permeation in meso-pores depends on temperature and decreases with the root of temperature according to the equation above. Because of this relationship, gas molecules with different masses can be separated according to the following equation [44]:

$$\alpha_{Knudsen\ a/b} = \sqrt{\frac{M_b}{M_a}} \quad (M_b > M_a) \quad (\text{Equ. 5})$$

Here, the separation is not influenced by the molecule diameter but only the molecule mass. Hence it is possible that a large molecule, e.g.  $\text{N}_2$ , passes the membrane faster than the smaller molecule e.g.  $\text{CO}_2$ .

Due to the small pore dimension and the high adsorption force, capillary condensation can occur in the lower pore size regime. This assuaged condensation can improve the transport through surface diffusion of the condensable gases, and therefore results in rising of the separation of condensable gases compared to non-condensable gases [45].

Micro-porous membranes can be distinguished through the pore dimension within the magnitude of molecule dimension. The pore size is usually defined by the kinetic diameter of the largest and to be permeated molecule. Both amorphous material, e.g.  $\text{SiO}_2$ , and crystal material, e.g. Zeolite, can possess micro-porous properties [42]. Burggraaf differentiates micro-porous materials furthermore into the ones with small micro-pore with  $d_p < 0.5$  nm

(also called ultra-micro-porous) and with large micro-pore with  $d_p = 1.0 - 2.0$  nm (also called super-micro-porous) [42].

There is the existence of a total molecule sieving effect in the small micro-pores whose separation mechanism is based on size exclusion. The larger gas component cannot penetrate the pores due to their molecule dimension. However, the smaller component can penetrate into the pores and adsorb there. Such materials are primarily applied for the separation where the temperature is higher and the selectivity through adsorption effect can be neglected. In an ideal case the selectivity can be infinite with such membranes. The advantage of such membranes is that the permeation will decrease as the selectivity increases [38, 42, 46]. Moreover, the distribution of the pores in micro-porous membrane should be so close, since the difference in the kinetic diameter of typical gases are still small (Table 1).

Table 1 Kinetic diameter and molecule mass of selected gases [47].

	He	H <sub>2</sub>	CO <sub>2</sub>	Ar	O <sub>2</sub>	N <sub>2</sub>	CO	CH <sub>4</sub>
<b>Kinetic diameter</b> [Å]	2.60	2.89	3.30	3.40	3.46	3.64	3.76	3.80
<b>Molecule mass</b> [g/mol]	4.00	2.02	44.01	39.95	32.00	28.01	28.01	16.04

There is a partial molecule sieving effect in large micro-pores. In this case all gas components can penetrate and adsorb in the pores. There exists a competing mass transfer due to the different adsorption and diffusion rates of the individual gas components. These mechanisms are dependent on charging and temperature, because at low temperatures, the pores are almost completely occupied and hence the mobility of the molecules is crucial for the separation. In contrast, at high temperatures, the molecules exhibit a high mobility, and the transport is limited by the respective sorption behaviour. Generally, materials with large micro-pores can be used for separation applications with larger gas molecules, which differ greatly by their interaction with the pore walls [42, 44, 45].

In micro-pores, the gas molecules can be located both on the pore walls and in gas phase. The transport is hence described as surface diffusion and gas phase diffusion. The surface diffusion, which dominates at low temperatures, is superimposed with increasing temperature by the gas phase diffusion and finally changes to an activated gas phase transport at high temperatures. The activated transportation is mainly characterized by the increase in the

permeation as a function of temperature. This temperature dependency is expressed by the following Arrhenius equation [45]:

$$F \propto F_0 \cdot \exp\left(\frac{-E_a}{R \cdot T}\right) \quad (\text{Equ. 6})$$

where  $E_a$  [kJ·mol<sup>-1</sup>] is the activation energy.  $E_a$  is calculated empirically for each type of gas by the relationship between temperature and permeation.  $E_a$  is composed of two contributions and can be both positive and negative:

$$E_a = E_m - Q_{st} \quad (\text{Equ. 7})$$

where  $E_m$  [kJ·mol<sup>-1</sup>] is the positive mobility energy which is required for the jumping from one side to the other side of the pore wall and  $Q_{st}$  [kJ·mol<sup>-1</sup>] is the isosteric adsorption heat. The activation energy is characteristic for the quality of membranes for gas permeation. Defect-free, high quality gas separation membranes operate on the principle of the activated gas transport and thus have a higher  $E_a$  value than defect containing membranes with proportionate Knudsen diffusion [48]. A high  $E_a$  value is the origin for high  $E_m$  values due to the presence of highly selective pores. In high-quality membrane layers, the  $E_a$  value for H<sub>2</sub> is higher than 10 [kJ·mol<sup>-1</sup>]. However, the  $E_a$  is below this value for total membrane with substrate [49].

### 3.3 Porous membranes

#### 3.3.1 Structure of porous membrane

In general, gas separation membranes can be dense or porous. Dense membranes, e.g. ionic conduct ceramic membranes, are permeable only for few gaseous components, e.g. hydrogen and oxygen. However, dense membranes possess relatively low permeability and require typically a high operation temperature. The permeability through dense membranes depends also strongly on the thickness of the layer [50, 51].

If a membrane only consists of one function layer, it will be denominated as symmetrical. In order to minimize the transport resistance, the membrane thickness can be reduced. Due to the limited mechanical stability, the gas separation membranes are usually produced in a graded multi-layer structure [10]. Thus, a macro-porous and a meso-porous interlayer will be deposited on the substrate. On the top the functional membrane is coated (Fig. 7). Because the transport resistance is mainly determinate by the function layer, such graded structures enable a thickness minimization of the gas separation membrane. Various materials might be used in

such a graded structure. Such kind of membranes is denominated as composite membrane [10, 38].

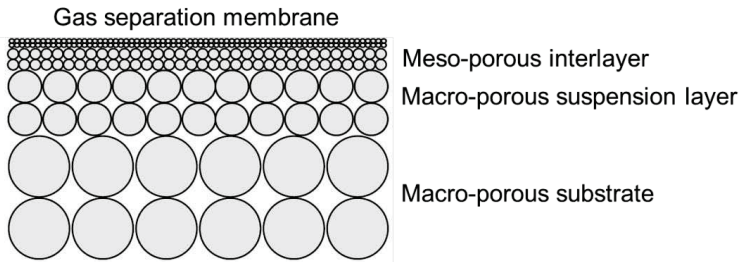


Fig. 7 Structure of a graded porous membrane [9].

The macro-porous support structure has a thickness of a few millimetres and supports the entire system mechanically. Most current micro-porous membranes have  $\alpha$ - $\text{Al}_2\text{O}_3$  substrate or  $\text{ZrO}_2$  produced by extrusion, film or vacuum slip casting [10, 52].

The mesoporous interlayer usually has a thickness of 0.5-10 microns and serves to bridge the pores with different sizes between carrier and functional layer. Without the intermediate layer, suspension with small particles would easily infiltrate in the large spaces of the carrier [53]. There will not be any supporting effect. Furthermore, the intermediate layer has the function to reduce the surface roughness and to mask defects, so that the functional layer can be deposited homogeneously and defect-free [54]. Most meso-porous oxide layers consist of  $\text{Al}_2\text{O}_3$ ,  $\text{ZrO}_2$ ,  $\text{TiO}_2$  or  $\text{CeO}_2$  [52]. Here  $\gamma$ - $\text{Al}_2\text{O}_3$  layers are often applied in the case of gas separation membranes due to the ease of preparation and the good film quality.

The micro-porous functional layer is crucial for gas separation membranes. For proper performance, it is necessary that this layer has neither defects nor inhomogeneity. Therefore, more intermediate layers are often applied in practice that ensures a defect-free production of the functional layer [52]. Often used materials for micro-porous layers are  $\text{Al}_2\text{O}_3$ ,  $\text{ZrO}_2$ ,  $\text{TiO}_2$  and  $\text{SiO}_2$  [55-57].

In the application of the ceramic layers, the suspension must completely cover the substrate surface. Since generally the surface to be coated is completely wetted in the dip-coating and rotation-coating, they are particularly suitable for deposition of meso-porous and micro-porous layers [10, 58, 59]. However, a chemical vapour deposition method might also be for micro-porous layers [60].

### 3.3.2 Porous silica membranes

In the recent years, amorphous micro-porous SiO<sub>2</sub>-membranes have been intensively studied for the gas separation, because they have a good chemical and thermal stability and have a high power potential in the form of a high permeation and selectivity [61]. Silica membranes can be produced by sol-gel route or via CVD (chemical vapour deposition) [62]. However, the key problem of silica membranes is the reproducibility, which causes a large fluctuation of the permeability and a low selectivity. The reason is unusually the defects from coating process, which is currently a challenge for all inorganic membranes [63].

The principle of CO<sub>2</sub> separation with silica membrane is the CO<sub>2</sub> adsorption on the silica pore surface [64, 65]. Therefore, in order to improve the selectivity and permeability of silica membrane, it is necessary to enhance the affinity between CO<sub>2</sub> and silica membrane surface.

### 3.3.3 Porous silica membranes modified with amino-group

A widespread and technically mature method for separation of CO<sub>2</sub> from gas mixtures is the absorption of CO<sub>2</sub> in aqueous solutions of alkyl-amines, also called amine scrubbing. The CO<sub>2</sub> absorption takes place here via the formation of carbamates under dry conditions and bicarbonates under wet conditions [66, 67]. Furthermore, due to the development of meso- and micro-structured silica material, it has been possible to functionalize the porous silica material with amino-groups [68, 69], so that the separation of CO<sub>2</sub> can be realized through porous silica membranes modified with amino-group (Fig. 8).

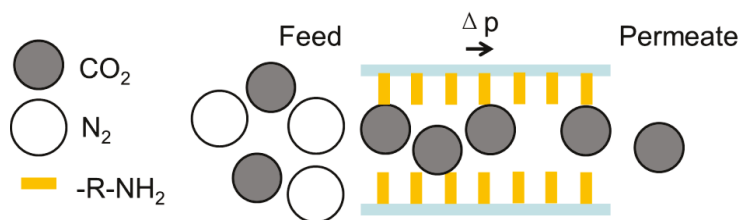


Fig. 8 Schematic function principle of a modified silica pore wall.

The term amine is used in organic chemistry for both specific functional groups as well as organic compounds (Fig. 9). These are derivatives of ammonia (NH<sub>3</sub>), in which one or more hydrogen atoms are replaced by alkyl-groups or aryl-groups. Referring to the concept of a functional group, a distinction is made, depending on how many hydrogen atoms of ammonia have been replaced by organic molecular groups between primary (-NH<sub>2</sub>), secondary (-NHR') and tertiary amines (-NR'R'') [25].

Amines are basic functional groups. A proton acid can be gripped by the free pair on the nitrogen atom, analogous to the ammonia molecule. This enables the removal of compounds with  $\text{CO}_2$  (Fig. 9) [67].

In secondary amino-groups, the adsorption is carried out analogously. Only ternary amino groups have a different adsorption [66, 67]. Functional amino groups can be active sites for  $\text{CO}_2$  chemisorption also on surfaces of solids. It is possible for the surface of silica gel to be modified with amino-groups by anchoring 3-aminopropyl [70, 71]. Then the functional amino groups are available as active sites where  $\text{CO}_2$  can be chemically absorbed at room temperature. The adsorption process results from the formation of ammonium carbamate under dry conditions. In each case, two functional amino groups are depleted by per adsorbed  $\text{CO}_2$  molecule. In the presence of water, the theoretical adsorption capacity of  $\text{CO}_2$  is doubled by the conversion of the carbamate into two adsorbed bicarbonate molecules [72]. It has been shown for porous silica membrane modified with amino-group that the adsorbed carbon dioxide completely desorbed at temperatures between about 70 and 140 ° C [70].

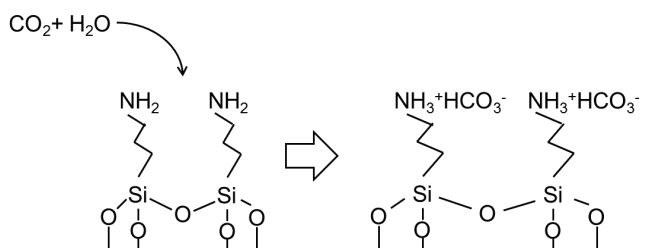


Fig. 9 Reaction of  $\text{CO}_2$  and  $\text{H}_2\text{O}$  on the silica surface with 3-aminopropyl-group [70, 71]

### 3.3.4 Synthesis of porous silica membranes

#### 3.3.4.1 Synthesis of porous silica membrane using a the sol-gel-route

The general method for manufacturing an inorganic membrane layer by using the sol-gel method is illustrated in Fig. 10 [73]. The procedure can be divided into the steps outlined in the following subsections.

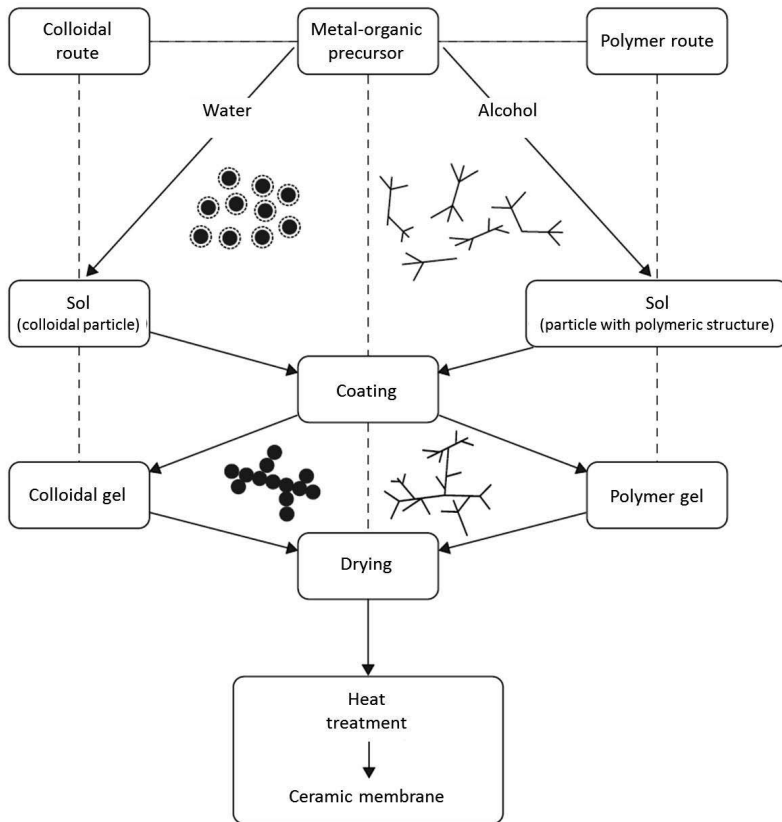


Fig. 10 Overview of sol-gel processes for the production of the inorganic membrane layers [73].

### Sol-production and coating

Dip coating is a convenient method for coating of the interlayers and functional layers in the manufacture of membranes. It has the advantage that surface to be coated can be completely wetted by immersion of the substrate. This ensures a complete layer covering on the substrate. Due to the uniform withdrawal of the substrate from the coating liquid, the layer is deposited homogeneously and with even thickness [10]. However, the characteristics and quality of a layer also depend strongly on the quality of the substrate or the intermediate layer. Therefore, a multitude of layers is often necessary before finally coating the last defect-free layer [74].

The film deposition dip-coating process is commonly divided into four steps, which are demonstrated in Fig. 11 [75].

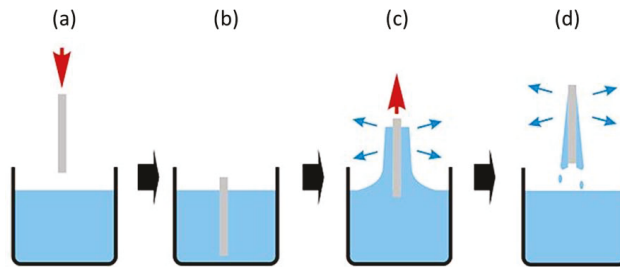


Fig. 11 Schematic drawing of dip coating process [75]: (a) immersing of the substrate, (b) keeping the substrate in the sol, (c) depositing and draining of the sol, (d) drying of the solvent.

- a) The substrate is immersed in the coating liquid; the substrate surface is wetted.
- b) The substrate moves; region of the liquid near-surface region of the liquid begin to circles.
- c) The substrate is withdrawn from the sol, as a film is deposited by the adhesion to the surface. Simultaneously the sol on the substrate surface runs downward due to the gravitational force.
- d) The solvent is evaporated from the deposited film.

The dip coating can be separated into horizontal and vertical methods. Tubular membranes are prepared on the vertical dip coating method, whereas planar membranes can be coated with both methods [75]. Fig. 12 schematically shows both methods for planar substrates.

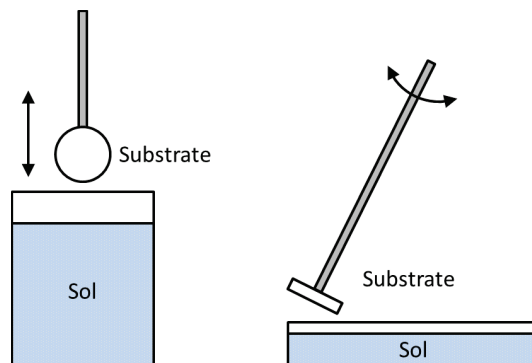


Fig. 12 Schematical drawing of vertical dip coating (left) and horizontal dip coating (right).

In the horizontal dip-coating only the surface comes to contact with the sol, whereas in the vertical dip-coating, the entire substrate is immersed. For vertical dip-coating, despite of the

full immersion, the probability is much higher that dirt from the substrate or substrate holder can remain in the sol and adversely affects subsequent coatings [75, 76]. Especially when the deposited layers have a thickness less than 5  $\mu\text{m}$  and a pore size less than 100 nm, dust and foreign matter defects can occur [10]. Furthermore, the immersion of the entire substrate body can induce many air bubbles from the highly porous substrate. These may settle on the substrate surface leading to defective locations.

### **Drying of sol-gel layer**

The step of drying is carried out in a temperature range between 80 and 350 °C and results in a layer containing residual organics. Drying is a difficult process, as it can be associated with evaporation of the solvent leading large shrinkage and concomitant cracking [76, 77]. The principle here is mainly based on the capillary forces of the liquid. If the gel capillaries have different diameters, in which the liquid is dried with different rates, high stress will occur in the smallest space [25].

### **Heat treatment of the sol-gel layer**

In this step, the remaining organic groups are burned at temperatures above 350 °C. The layer is solidified and obtained by the appropriate calcination or sintering its final pore structure [73, 78].

#### ***3.3.4.2 Functionalization of porous silica membranes with organic group***

To enhance the affinity of  $\text{CO}_2$  to the  $\text{SiO}_2$ -membrane surface, the membrane surface can be modified with function groups. By varying the organic residue  $R$ , the molecules anchored on the silica surface can carry various functions. The functionalization with amino groups is of importance for the development of  $\text{CO}_2/\text{N}_2$  gas separation membranes. The most commonly used alkoxy silane for amino-functionalization of silica is 3-aminopropyltriethoxysilane (APTES) which has a primary amino-group per molecule [79, 80].

In this work all the functionalization were conducted with APTES. One reason is that it is probably the most commonly used for amino-functionalization silane and can be formed according to many synthetic procedures described in the literature [25]. Another important reason is that the molecule is relatively small and the functional amino-group can be connected via a relatively short propyl-chain to the silica surface. This firstly facilitates the diffusion of the molecule in the pore network and also reduces the risk of blocking the pores. In principle, the surface modification is accompanied by surface anchoring of molecules with

a reduction of the pore cross-section. The thickness of a single amino-propyl-layer tethered to silica is about 7-9 Å [81-83].



Fig. 13 Atomic layer deposition (ALD) of the amino-propyl-siloxane layer [84]

The atomic layer deposition (ALD) is typically applied for this functionalization. As a chemical vapour deposition, ALD is based on the sequential use of self-terminating gas- solid reactions and can control the thickness precisely at angstrom or monolayer level. Another advantage of ALD processing is that they can fill all space independent of substrate geometry. The schematic principle of ALD for the functionalization of porous silica membranes in this work is shown in Fig. 13 [85, 86].

### 3.3.5 Degradation of silica membrane with water vapour

A disadvantage of  $\text{SiO}_2$  is that the low hydrothermal stability at higher temperatures under hydrous conditions leads to rapid membrane degradation. To characterize the permeability behaviour of silica membranes, it is necessary to analyse the thermal-chemical stability under water vapour of the silica surface.

There are three different groups on the silica surface: siloxane bridges ( $=\text{Si}-\text{O}-\text{Si}=\text{}$ ), hydroxyl groups ( $-\text{OH}$ ) and unsaturated Si atoms. The siloxane bridges are somewhat hydrophobic, while hydroxyl groups ( $-\text{OH}$ ) and unsaturated Si atoms are absolutely hydrophilic. Water vapour can be absorbed on the silica surface by physical sorption at low temperature and by reacting with the siloxanes at high temperature [87].

Since the hydrophobicity of silica surface increases with decreasing amount of hydroxyl groups, the hydrothermal stability of silica can be improved by increasing the sintering temperature [88] or by modifying with some organic [89-91] groups to substitute the hydroxyl groups. However, the organic groups on the silica surface themselves are not very stable at elevated temperatures. It is concluded in the study of de Vos [88] that the thermal stability up to 300 °C is higher for membranes calcined at higher temperature. The influence of the water

vapour pressure on the membrane deterioration is larger than that of the temperature. Although silica membranes calcined at higher temperatures have less hydroxyl groups, the decrease of hydroxyl group concentration does not increase the hydrothermal stability due to the fact that the pore size is reduced at higher calcination temperatures [92].

It was concluded in the study of Song [92] that the permeance through the silica membrane, even the organic-modified one, decreases in presence of water vapour. At high temperatures, the interaction between water vapour and the silica surface causes the densification or damage of the pore structure, while at low temperatures, the permeance decreases significantly in the presence of water vapour, even without destroying the pore structure [93, 94]. This phenomenon should become more significant at lower temperature where the mobility of H<sub>2</sub>O molecules decrease, while the amount of adsorbed H<sub>2</sub>O molecules increase due to the stronger interaction.

## 4 Literature review of investigated materials' properties

### 4.1 Substrate

Ceramic substrates have advantageous properties in terms of hardness, wear and temperature resistance and high resistance against acids and bases [95, 96]. However, they have the disadvantage that they are very brittle and thus in particular in the porous state, of limited strength associated with a rather large scatter related to the defect size distribution in the material [97-99]. Contrarily metallic substrates have both high fracture toughness as well as a corresponding high strength that are beneficial for membrane fabrication and operation. The temperature and corrosion resistance can be increased, by the selection of an appropriate alloy [100]. Another major advantage of metallic supports is the potential use of technical joining processes such as welding or soldering to install individual gas-tight porous membranes in large modules [101]. In the current work, one typical ceramic substrate material and one typical metallic substrate material were investigated, respectively, i.e. porous  $\alpha$ -Al<sub>2</sub>O<sub>3</sub> and porous ITM (Intermediate temperature metal).

#### 4.1.1 Ceramic substrate – porous $\alpha$ -Al<sub>2</sub>O<sub>3</sub>

As an interesting substrate option for ceramic layers, porous  $\alpha$ -Al<sub>2</sub>O<sub>3</sub> is usually used in oxyfuel or post-combustion [102]. The porous ceramic substrate should have both high permeability and high mechanical strength. Whereas the permeation increases with increasing porosity, the strength decrease with increasing porosity [103], requiring optimization with respect to necessary porosity and microstructure.

To analyse the strength of ceramic materials, the measured fracture strengths were evaluated statistically through a Weibull diagram and the Weibull parameters are also derived in this way.

$$F(\sigma_c) = 1 - \exp\left[-\left(\frac{\sigma_c}{\sigma_0}\right)^m\right] \quad (\text{Equ. 8})$$

$$\ln \ln \frac{1}{1-F} = m \ln \sigma_c - m \ln \sigma_0 \quad (\text{Equ. 9})$$

where  $\zeta_c$  is the fracture strength,

$\zeta_0$  the characteristic fracture stress and

$m$  the Weibull modulus.

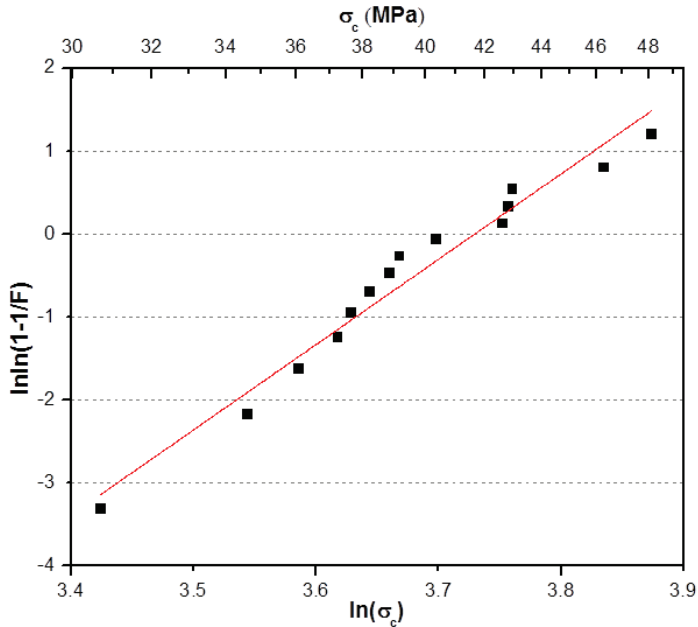


Fig. 14 Example of a Weibull diagram

Here, the characteristic fracture stress (strength  $\zeta_c = \zeta_0$ ) is the value at which 63.2% of all samples fail ( $F = 63.2\%$ ) and can be seen as the average value of fracture stresses. The Weibull modulus  $m$  is a representation of the distribution of fracture stresses: The larger  $m$  is, the lower is the dispersion of the fracture stress and enables a prediction of failure probability under a particular load condition in accordance with the characteristic strength value. In Weibull diagram  $m$  corresponds to the slope of the fitting line. Meanwhile, Young's modulus and fracture strain are also important parameters to describe the deformation behaviour of the ceramic materials. Young's modulus of certain ceramic depends on the density and the porosity, also the pore size and the pore form. It represents the stiffness of materials. Similarly, fracture strain also describes the stiffness via the deformation of materials at fracture point.

In Table 2, the mechanical properties of some typical potential membrane substrate materials are compared. The materials were all tested using a ring-on-ring bending test set-up with identical loading and support geometries. Porosities of all materials are in application relevant ranges. For example MgO substrates have been suggested in literature for CGO layers [104],  $\text{Ba}_{0.5}\text{Sr}_{0.5}\text{Co}_{0.8}\text{Fe}_{0.2}\text{O}_{3-\delta}$  (BSCF) or  $\text{La}_{0.6}\text{Sr}_{0.4}\text{Co}_{0.2}\text{Fe}_{0.8}\text{O}_{3-\delta}$  (LSCF) are known to possess rather high permeation rates [105, 106] and hence can be useful for oxyfuel or post-combustion processes.

Table 2 Comparison of the mechanical properties of the different ceramic substrate materials

Material	MgO [107]	CGO [104]	BSCF [104]	LSCF [104]
Porosity	36	43	34	46
$E$ [GPa]	$55 \pm 3$	$57 \pm 14$	$35 \pm 3$	$12 \pm 4$
$\sigma_0$ [MPa]	$41 \pm 2$	$55 \pm 3$	$31 \pm 1$	$18 \pm 2$
Fracture strain	0.075	0.096	0.089	0.15
$m$	$19^{+5}_{-7}$	$4 \pm 2$	$5 \pm 2$	$4 \pm 2$

#### 4.1.2 Metallic substrate – porous ITM (Intermediate temperature metal)

Despite of the advantages like hardness, friction and thermochemical resistance, ceramic substrate materials are fragile and not ductile enough against shocking. Contrarily, metallic substrates possess not only high fracture toughness but also advanced strength during the membrane production and application. Meanwhile, with the aid of proper alloying elements, the thermochemical and corrosion resistance of metallic substrates can also be improved.

Table 3 Parameters of porous ITM at room temperature [108]

Properties	Value	Principle or method of measurement
Porosity	0.38	Archimedes principle
Young's modulus ( $E_0$ ) of dense ITM	206 GPa	Four-point bending test
Young's modulus ( $E$ ) of porous ITM	53 GPa	Calculated by $E = E_0 \cdot (1 - 1.7 \cdot P)^{1.3}$ , where $E_0$ is Young's modulus of dense ITM, $P$ porosity of 0.38
Poisson's ratio ( $\nu$ )	0.29	Impulse excitation technique

ITM alloy is an oxide dispersive strengthened ferritic Fe-Cr alloy produced by Plansee SE and can provides good chemical and mechanical stability at elevated temperature. Compared to commonly used metallic porous substrates, e.g. stainless steel 1.4404, ITM has good high

temperature resistance and larger pore size which has lower gas flow resistance [108-111]. Hence, ITM is proved to be good choice as the metal support for metal supported SOFC (solid oxide fuel cell) [112]. As interconnector in SOFC, the ITM needs to have a high porosity for the active zone. In the study [108], some typical properties of dense and porous ITM were investigated (Table 3).

## 4.2 Membrane

### 4.2.1 Porous silica membrane

In order to permit a comparison with the permeability of silica membrane in the current study, Table 4 summarizes some literature data and permeation results of silica membranes from literatures. As mentioned in section 3.3.2, silica membranes are usually produced by sol-gel route or CVD. Thus, at the bottom of the table there are the data of several silica membranes produced via CVD as comparison.

Table 4 Data of selected silica membranes from literatures.

Membrane and data source	Produce method	Temperature (°C)	CO <sub>2</sub> permeation (mol·m <sup>-2</sup> ·s <sup>-1</sup> ·Pa <sup>-1</sup> )	N <sub>2</sub> permeation (mol·m <sup>-2</sup> ·s <sup>-1</sup> ·Pa <sup>-1</sup> )	CO <sub>2</sub> /N <sub>2</sub> Selectivity
SiO <sub>2</sub> [113]	Sol-gel (calcinated at 400 °C)	25	2.3·10 <sup>-7</sup>	1.0·10 <sup>-9</sup>	23
		200	2.3·10 <sup>-7</sup>	2.7·10 <sup>-7</sup>	9
SiO <sub>2</sub> [114]	Sol-gel (calcinated at 600 °C)	100	8.0·10 <sup>-9</sup>	1.0·10 <sup>-9</sup>	8
SiO <sub>2</sub> [115]	Sol-gel (calcinated at 450 °C)	80	6.7·10 <sup>-8</sup>	1.0·10 <sup>-9</sup>	60
SiO <sub>2</sub> [116]	Sol-gel (calcinated at 500 °C)	150	2.0·10 <sup>-10</sup>	-	-
SiO <sub>2</sub> [117]	Sol-gel (calcinated at 600 °C)	400	1.2·10 <sup>-8</sup>	-	-
SiO <sub>2</sub> [118]	Sol-gel (calcinated at 500 °C)	200	1.3·10 <sup>-8</sup>	4.2·10 <sup>-9</sup>	3
SiO <sub>2</sub> [119]	CVD	100	9.0·10 <sup>-8</sup>	3.5·10 <sup>-8</sup>	3
SiO <sub>2</sub> [120]	CVD	600	8.1·10 <sup>-11</sup>	-	-
SiO <sub>2</sub> [121]	CVD TEOS	200	3.3·10 <sup>-10</sup>	5.0·10 <sup>-10</sup>	1
	CVD PTES		1.0·10 <sup>-8</sup>	1.0·10 <sup>-9</sup>	6
	CVD DPDES		3.3·10 <sup>-8</sup>	7.9·10 <sup>-9</sup>	4

All the membranes show low permeation of CO<sub>2</sub> and N<sub>2</sub> below  $3.0 \cdot 10^{-7} \text{ mol} \cdot \text{m}^{-2} \cdot \text{s}^{-1} \cdot \text{Pa}^{-1}$ . Some silica membranes have even no measurable N<sub>2</sub> permeation. The silica membrane produced by CVD in the study of Gopalakrishnan et.al has the highest permeation of CO<sub>2</sub> and N<sub>2</sub> [119]. The highest selectivity is reported for the silica membrane in the study published by Tsai et.al [115], which is produced via sol-gel route. The selectivity of membrane in the study of De Vos [113] exhibits a pronounced temperature dependence (CO<sub>2</sub>/N<sub>2</sub> selectivity is 23 at 25 °C, 9 at 200 °C).

#### 4.2.2 Amino-modified silica membrane

Table 5 Data of selected amino-modified silica membranes from literatures.

Membrane and data source	-NH <sub>2</sub> source	Measure temperature (°C)	CO <sub>2</sub> permeation (mol·m <sup>-2</sup> ·s <sup>-1</sup> ·Pa <sup>-1</sup> )	CO <sub>2</sub> /N <sub>2</sub> Selectivity
Amino-modified silica [122]	GlyNa	22	$2.1 \cdot 10^{-8}$ to $1.0 \cdot 10^{-7}$	52.3 to 100.0
Amino-modified silica [122]	APTES	22	$1.7 \cdot 10^{-8}$ to $3.9 \cdot 10^{-8}$	41.0 to 76.8
Amino-modified silica [122]	APTES	22	$8.1 \cdot 10^{-8}$ to $1.3 \cdot 10^{-7}$	24.0 to 27.2
Amino-modified silica [122]	APTES	22	$6.6 \cdot 10^{-9}$ to $3.4 \cdot 10^{-8}$	43.6 to 88.8
Amino-modified silica [123]	APTES	22	$1.0 \cdot 10^{-7}$	26
Amino-modified silica [123]	APTES	22	$1.8 \cdot 10^{-8}$	34
Amino-modified silica [123]	APTES	22	$1.4 \cdot 10^{-7}$ to $1.9 \cdot 10^{-7}$	44.5 to 78.4
Amino-modified Vycor glass tube [124]	APTES	120	$2.7 \cdot 10^{-10}$	10
Amino-modified Vycor glass tube [124]	APTES	57	$2.3 \cdot 10^{-11}$	-
Vycor glass tube [124]	APTES	100	$1.4 \cdot 10^{-10}$	5.85

In order to compare with the permeability of silica membrane in the current study, Table 5 quotes some data and permeation results of amino-modified silica membranes from literatures.

The amino-modified silica membranes developed by Xomeritakis et al. [122, 123] have a high CO<sub>2</sub> permeation and a high CO<sub>2</sub>/N<sub>2</sub> selectivity. However, it is concluded in their study that the membranes were difficult to be manufactured due to the hardly realized pore sizes and porosity in the silica structure. Thus, a commercial method using Vycor glass tube, which is modified by APTES, was developed by Ostwal et al. [124]. However, compared to the results of Xomeritakis's membranes, the membranes of Ostwal show lower CO<sub>2</sub> permeation and lower CO<sub>2</sub>/N<sub>2</sub> selectivity.

A comparison of the permeation of silica membrane before and after amino-modification is presented in Table 6. Sakamoto et al. [125] prepared meso-porous silica membrane using hydrothermal and sol-gel spin-coating methods and functionalize the pore surface through amino-silane (APTMS). This modification resulted in a reduction of CO<sub>2</sub> permeation; however, the CO<sub>2</sub>/N<sub>2</sub> selectivity was obviously enhanced.

Table 6 The results of the CO<sub>2</sub>/N<sub>2</sub> mixed gas (CO<sub>2</sub> = 20%) permeation tests for Al<sub>2</sub>O<sub>3</sub> substrate and mesoporous silica membranes before and after modification [125]

Membrane and data source	Membrane prepare method	Measure temperature (°C)	CO <sub>2</sub> permeation (mol·m <sup>-2</sup> ·s <sup>-1</sup> ·Pa <sup>-1</sup> )	CO <sub>2</sub> /N <sub>2</sub> Selectivity
before modification	Spin-coating	21	3.4·10 <sup>-7</sup>	0.8
before modification	Hydro-thermal	21	1.0·10 <sup>-8</sup>	0.8
after modification	Spin-coating	100	1.0·10 <sup>-9</sup>	800
after modification	Hydro-thermal	100	4.7·10 <sup>-10</sup>	50

In this work, the SiO<sub>2</sub>-membrane and amino-modified SiO<sub>2</sub>-membrane were investigated in the permeation test to reveal the gas separation mechanism. Furthermore, the water vapour was also added into the feed gas to simulate the flue gas in power plants.

## 5 Materials and experimental methods

### 5.1 Characterization of membranes with different substrates

In this work micro-porous membranes with different types of substrates were characterized.

#### 5.1.1 Membranes with Atech substrate

These  $\alpha$ - $\text{Al}_2\text{O}_3$  substrates were delivered by our project partner Atech innovations GmbH (Gladbeck, Germany) and produced already with gradient layer structure. Two  $\alpha$ - $\text{Al}_2\text{O}_3$  suspension layers were deposited on the  $\alpha$ - $\text{Al}_2\text{O}_3$  support (Fig. 15). The support was prepared though an extrusion process. The details of the manufacture of the substrates can be found in Table 7 [126]. The structure of membrane with Atech substrate is shown in Fig. 15. The substrates had a diameter of 39 mm and a thickness of 2.25 mm, the pore size of the upper layer was given as 50 nm [127].

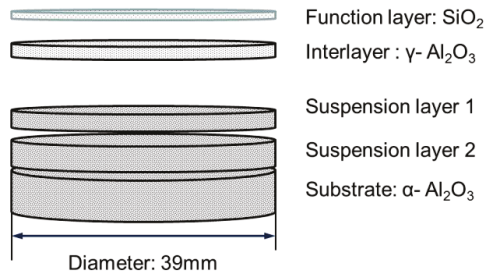


Fig. 15 Structure of membrane with Atech substrate.

Table 7 Main manufacturing parameters of coating layers on Atech ceramic substrates.

	Material	Production	Sintering temp. (°C)	Holding time (h)
Interlayer	$\gamma$ - $\text{Al}_2\text{O}_3$	Dip-coating with boehmite	600	3
Silica membrane	$\text{SiO}_2$	Dip-coating with silica polymersol	500	3

The applied  $\gamma$ - $\text{Al}_2\text{O}_3$  interlayer is formed via heat treatment of  $\text{AlO}(\text{OH})$ , which was produced by sol-gel-synthesis. Since this material is not stable under hydrothermal conditions, doping with 6 mol.-% lanthanum was necessary to enhance the stability of  $\gamma$ - $\text{Al}_2\text{O}_3$ . The coated  $\text{AlO}(\text{OH})$  films were prepared starting from 20 °C heated with a heating rate of 1 K/min to the

calcination temperature of 600 °C in air and held for 3 h. Then the mixture was cooled with a cooling rate of 1 K/min to 20 °C. Thereby, the deposited AlO(OH) film was transformed into a porous oxide layer.

For the synthesis of SiO<sub>2</sub>, alkoxides precursor (TEOS) was firstly mixed with water-free ethanol. Then a mixture of H<sub>2</sub>O and HNO<sub>3</sub> was added into the stirring TEOS solution with a rate of 1.5 ml/min. After the following complete reaction at 60 °C for 3h, the sol was cooled down and cleaned with a 0.8 μm syringe filter (Whatman, FP 30/0.8 CA). Then the clear sol was used to coat the previous γ-Al<sub>2</sub>O<sub>3</sub> layer. The SiO<sub>2</sub>-functional layers were handled with a heat treatment at 500 °C for 3 h with a heating and cooling rate of 1 K/min, respectively.

More details of the manufacture of the coating layers can be found in [4].

### 5.1.2 Membranes with IEK-1 substrate

These nano-porous substrates with a diameter of 39 mm and a thickness of 2 mm were delivered by project partner in IEK-1, Forschungszentrum Jülich and manufactured via a modified slip casting process. Firstly, the slurry was prepared adding α-Al<sub>2</sub>O<sub>3</sub> powder (AKP30, Sumitomo, Japan) with a mean particle size of 0.32 μm to a 0.02 M HNO<sub>3</sub> solution. The slurry was treated for 15 min by an ultrasonic device (Sonifier 450, Branson, USA) for homogenization and crushing of agglomerates. Then the liquid was removed by sucking it through a polymeric membrane (support-800-0.8 μm, diameter 47 mm, Pall, USA) of a suction filter device. The filtration process was supported by a vacuum pump on the permeate side. The filtering cake was dried for 10 h in the suction filter without further evacuation on the permeate side. Afterwards, the α-Al<sub>2</sub>O<sub>3</sub> discs were sintered for 1 h at 1100°C in air using a heating and cooling ramp of 2 K/min. The final geometry of the nano-porous substrates (diameter 39 mm, thickness 2.4 mm) was achieved by grinding and lapping. For further improvement of the surface quality, the surface was polished using diamond pastes with 6 μm and 3 μm particles. Finally, the samples were cleaned by ultrasonic treatment in ethanol and subsequently dried.

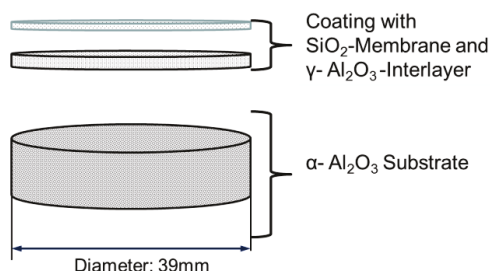


Fig. 16 Structure of membrane with IEK-1 substrate.

Table 8 Main manufacturing parameters of coating layers and IEK-1 ceramic substrates.

	Material	Production	Sintering temperature (°C)	Holding time (h)
Substrate	$\alpha$ -Al <sub>2</sub> O <sub>3</sub>	Slip-casting	1100	1
Interlayer	$\gamma$ -Al <sub>2</sub> O <sub>3</sub>	Dip-coating with boehmite	600	3
Silica membrane	SiO <sub>2</sub>	Dip-coating with silica polymersol	200	3

The manufacturing steps for the  $\gamma$ -Al<sub>2</sub>O<sub>3</sub> and SiO<sub>2</sub> layer on IEK-1 substrates were same with as for Atech substrates. The details of the manufacturing of the coating layers can be found in [25, 128-130]

### 5.1.3 Membranes with metallic ITM substrate

The metallic substrates were manufactured by the Plansee Composite Materials GmbH (Germany) and coated in IEK-1. Fig. 17 shows the layered structure of such samples. The substrate is made of the alloy ITM (Intermediate- Temperature- Metal). The most important manufacturing parameters are listed in (Table 9). Because of confidentiality agreement, more details of ITM product information cannot be published.

Table 9 Main manufacturing parameters of coating layers on ITM metallic substrates.

	Material	Production	Sintering temp. (°C)
Suspension layer 1	8YSZ (from UCM Advanced Ceramics)	Dip-coating	1250
Suspension layer 2	8YSZ (from Tosoh)	Dip-coating	1100
Interlayer	$\gamma$ -Al <sub>2</sub> O <sub>3</sub>	Dip-coating with boehmite	600
Silica membrane	SiO <sub>2</sub>	Dip-coating with silica polymersol	200

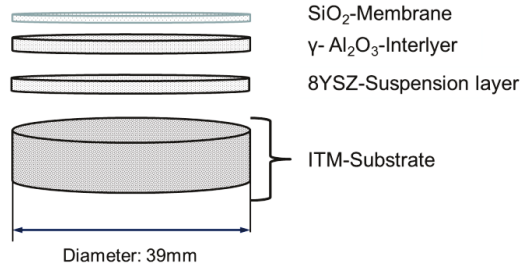


Fig. 17 Structure of membrane with ITM substrate.

#### 5.1.4 Mercury porosimetry

The mercury porosimetry is an analysis method to determine various quantifiable aspects of a porous material, such as pore size distribution, total pore volume, inner surface, the bulk density and the absolute density. The technique involves the penetration of a non-wetting liquid such as mercury at high pressure in a material using a porosimeter. The pore size is determined as a function of the external pressure, which is necessary to force the liquid into a pore against the surface tension of the liquid.

For cylindrical pores, the Washburn-Equation is to be applied [131]:

$$P_L - P_G = \frac{4\sigma \cdot \cos \theta}{D_p} \quad (\text{Equ. 10})$$

where  $P_L$  is the pressure of liquid Hg,

$P_G$  the pressure of gas (null for the vacuum applied in this study),

$\sigma$  the surface tensile stress of liquid Hg,

$\theta$  the contact angle of liquid Hg and

$D_p$  the diameter of pore.

With increasing pressure the cumulative pore volume also increases. From the cumulative pore volume, the average pore size can be determined by the equation above. The distribution of the cumulative pore volume can result in a distribution of differential pore radius distribution.

In this work, the measurements of the porosities were preceded by mercury porosimeter Pascal 440 (from company Thermo Scientific™) in IEK-1, Forschungszentrum Jülich.

## 5.2 Determination of membrane permeability

In this work, the permeation testing were carried out by single gas tests and mixed gas tests, respectively. The purpose of single gas permeation tests was determined the gas separation mechanism for the supplied membranes and the mixed gas tests aimed at the simulation of the real conditions in fossil fired power plants.

### 5.2.1 Setup of single gas permeation tests

The single-gas permeation tests were carried out with He, CO<sub>2</sub> and N<sub>2</sub>. The set-up of the single gas test is shown in Fig. 18. With this method, flow rates of various single gases at different temperatures and for various pressure differences can be measured. The flow rates are required to calculate the permeation and selectivity. In this work the gases He, CO<sub>2</sub> and N<sub>2</sub> were used. The feed pressure is adjusted by a pressure sensor (Company WIKA, type 232.30.100) and a pressure gauge (Company Samson, type 5824-30) between 0 bar and 5 bar. The pressure difference results from the difference of between feed side pressure and permeate side pressure. The permeate side is contacted to the environment and therefore fixed to 1 bar. The membrane module is located in a heating box with a maximum temperature of 200 °C which is limited by the thermal stability of sealing rings (HUG GmbH, type FPM75). The flow through membrane area can be calculated by the size of the covering sealing ring (Freudenberg Sealing Technologies, type FKM 33034,  $A = 3.14 \text{ mm}^2$ ). The bypass is during the measurement always switched off and is only switched on to help to purge the permeate side when changing the feed gas. The flow meter for the single gas tests is from company Agilent, type ADM2000.

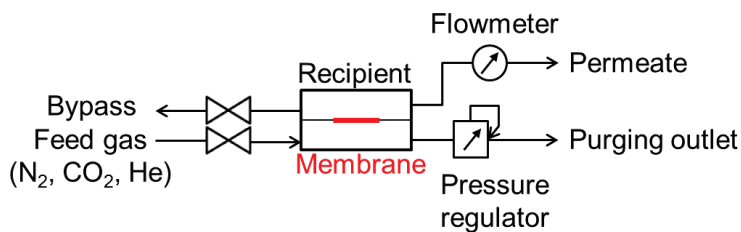


Fig. 18 Schematic structure of the single gas testing system

### 5.2.2 Set-up of mixed gas permeation tests

Fig. 19 shows a schematic representation of the permeation set-up. The available gases are mixed together in a mixing chamber. To investigate the influence of moisture on the permeability, a water reservoir is incorporated into the permeation test set-up. A coil heating

element (Company Hillesheim GmbH, type HSS) for water gasification and gas preheating is integrated in the test facility behind the mixing chamber. The coil and the tubing past it can be heated to a maximum temperature of 270°C in order to vaporize the liquid water and prevent condensation of water vapour in the tubing. After heating to a defined temperature, feed gas is flowed to the membrane side.

The permeate with sweep gas is analysed by a mass spectrometer (Company Pfeiffer Vacuum, type OmiStar™ OMS 200), so that the concentrations of the components can be calculated. For calibration of the mass spectrometer, the reference gases consist respectively of 5% O<sub>2</sub>, 10% CO<sub>2</sub>, 85% N<sub>2</sub> for feed gas and 1 % O<sub>2</sub>, 4 % N<sub>2</sub>, 5 % CO<sub>2</sub>, 90 % Ar for permeate.

The experimental conditions for the investigation of porous membranes in the permeation test facility are listed below:

- Feed gas: 15% CO<sub>2</sub>, 85% N<sub>2</sub>.
- Sweep gas: Ar.
- Operating temperature: 20 to 230 °C.
- Pressure range: 0 to 6 bar.

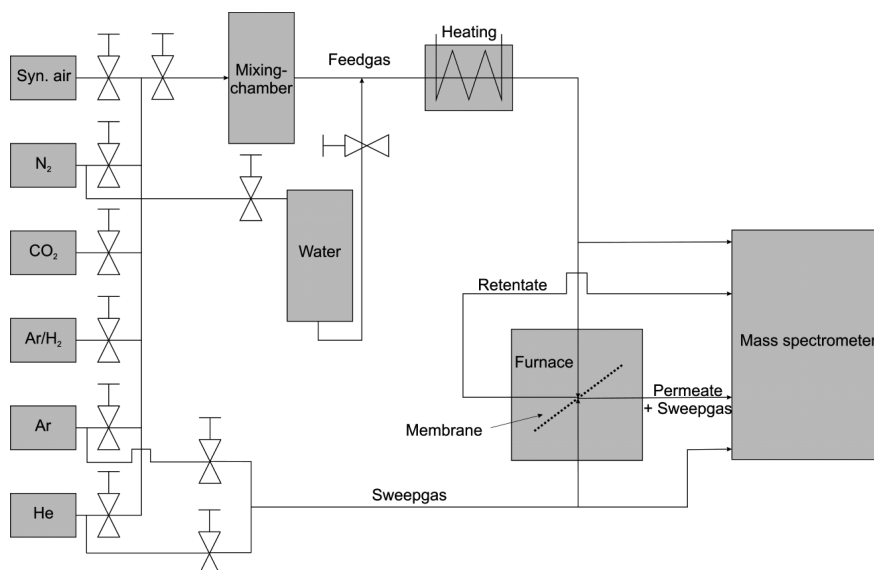


Fig. 19 Schematic representation of the permeation test facility.

A process monitoring software (Fig. 20) for the operation of the permeation test set-up was developed by ZEA-1, Forschungszentrum Jülich. It allows the operator to select the operating conditions for each experiment. The test facility features a computer supported gas mixing system (software SEMATIC, Siemens) in which the gas stream composition and flux can be varied for both the feed- and for the sweep side of the membrane. The pressure on each side of the membrane can be set to different values.

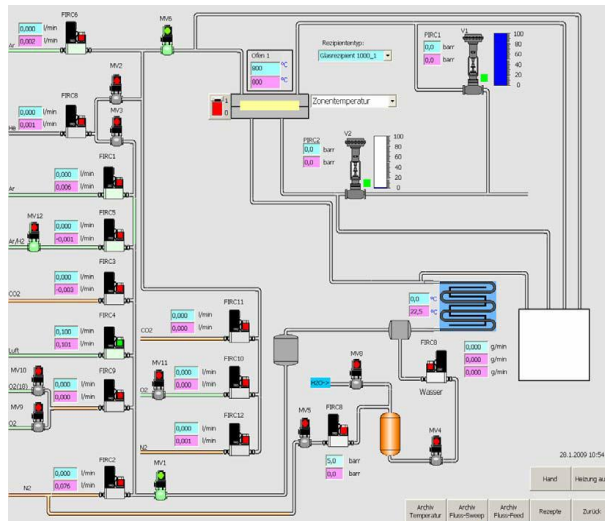


Fig. 20 Screen shot of the process monitoring software

### 5.2.2.1 Recipient

The temperature range for the permeation measurement of porous membranes was from room temperature to 200 °C. A stainless steel sample holder was used. The application of stainless steel recipient allows the measurements with high pressure. In this work, the highest pressure on the feed side was 6 bar. The inner sample holder and the outer block are both assembled tightly with six bolts. The sample holder was designed for disk-shaped membranes with a diameter of 40mm and a thickness ranging between 0.3 mm and 5 mm.

In the current work, all the tested specimens had a thickness of 2 mm and a diameter of 39 mm. According to the dimension of the specimens, the silicon sealing rings between the sample holder and the outer recipient was selected with a size of  $\varnothing 76 \times 4$  mm (FPM75, HUG GmbH). The silicon sealing ring between membrane and sample holder was with  $\varnothing 20.29$  mm  $\times$  2.62 mm (80FKM, HERTEL).

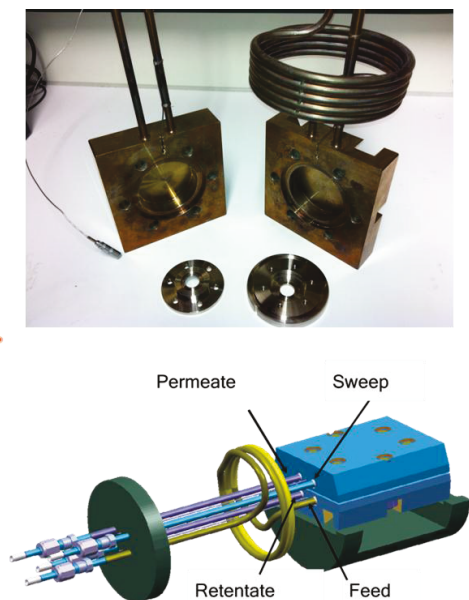


Fig. 21 Recipient of permeation measurement set-up for micro-porous membranes

#### 5.2.2.2 Development of heating system

Due to the necessary temperature variation and the control of the 2-zone furnace (ETO 20/40, Prüfer GmbH) in the operating temperature range (from RT up to 200 °C), the furnace was replaced with additional heating system (HBSIE, Horst) with a temperature controller (HT MC1, company Horst). The set-up of the test is shown in Fig. 22.

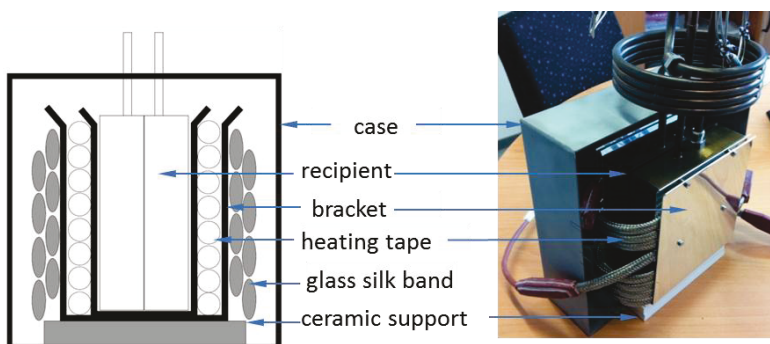


Fig. 22 Schematic drawing of cross-section and photo of the heating box.

The recipient is plugged in sandwich-like brackets. The heating tape is loaded between the two brackets. The brackets have a high thermal conductivity so that the temperature of the recipient can be well regulated by the heating tape. The clips are firmly wrapped externally with glass fibre band and supported by a ceramic substrate, so that the brackets and the recipient are well contacted. The remaining space of the housing is filled with insulating materials.

The leakage overflow between membrane holders and recipient is  $10^{-7}$  mbar·l·s<sup>-1</sup> according to the helium leak test (Pfeiffer Vacuum, ASM310). Therefore, the metallic seal rings have been replaced with Viton O-rings reducing the leakage to  $10^{-9}$  mbar·l·s<sup>-1</sup>.

It is important to ensure that the metal recipient is introduced centrally in the heater bracket and the heating conductors on the sides are not damaged. The recipient is to abut with its side surfaces to the inner wall of the bracket as well as possible (Fig. 23).

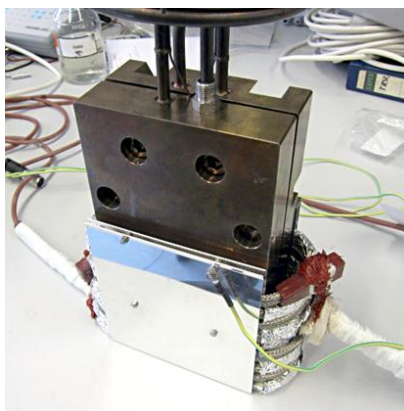


Fig. 23 Installation of recipient into the brackets.

The heating staple is placed with the recipient together on a pad in the insulated box. The insulated inner surface of the lower half of the heating box is stabilized specifically by the support of the recipient (Fig. 24).

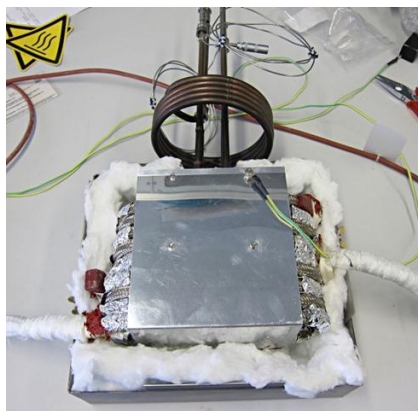


Fig. 24 Installation of the recipient and brackets into the insulated box.

The upper part of the box is gently pushed onto the lower part. The heating conductor has to be gently inserted into the cut-outs so that squeezing can be prevented. The insulated box with the built-recipient is operated for heating on a fireproof surface.

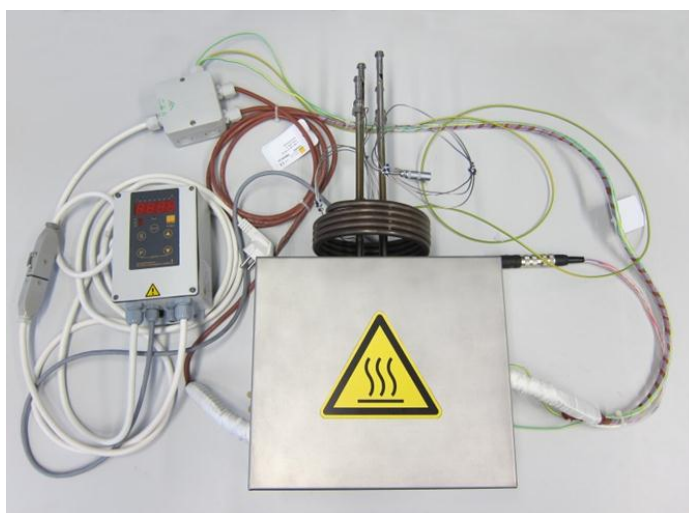


Fig. 25 Complete installation of the recipient in the heating box

After complete assembly and checking of the environment for flammable materials, the heating control is connected to the grid and continuously monitored during the full heating phase. The set point for heating can be set to 230 °C at the beginning. At target temperatures below 150 °C a reasonably lower temperature for heating should be chosen. According to the calculated heating curve, the set point of temperature in the recipient is to be set by about 5 -

10 °C above the desired temperature until about 20 minutes before reaching the desired temperature. After that the desired value should be approximately achieved and the heating temperature will be maintained.



Fig. 26 Heating progress for a 230 °C set point of the heating box for the metallic recipient.

### 5.2.3 Performance of permeation measurements

The concentration of the gas components is measured with the aid of a mass spectrometer. The mass spectrometer consists of ion source, magnetic sector and detector.

In the ion source electrons are generated by thermo-emission from a filament. Through bombardment of the generated electrons on neutral gas molecules the later are ionized or dissociated into fragments. Then the ions go into the magnetic sector where they are separated according to their characteristic mass-to-charge ratio. The used quadrupole mass spectrometer separates the ions in a high-frequency electric quadrupole field between four rod electrodes with a specific field radius (Fig. 27).

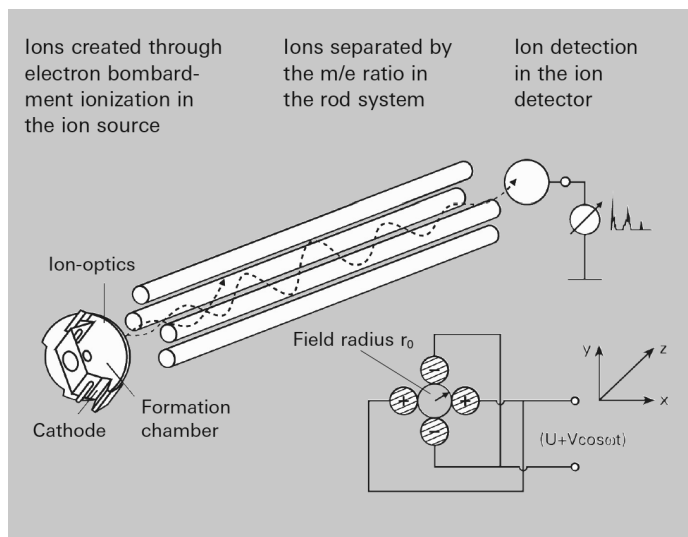


Fig. 27 Schematic of a quadrupole mass spectrometer (source: Pfeiffer Vacuum)

For gas analysis a quadrupole mass spectrometer was used by the company Pfeiffer Vacuum in this work (Type OmiStar™ OMS 200, Pfeiffer Vacuum), which a heated gas inlet system (Gas Stream Selector 300) is preceded by twelve separately addressable gas inlet channels. For detection of the ions, a Faraday-Cup is optional with an SEM are available. The experiments were all carried out without SEM [132].

### 5.3 Thermal stability evaluation

In the post-combustion process, the flue gas will weep the SiO<sub>2</sub> membrane in order to separate carbon-dioxide by diffusion through the porous layers. Consequently, the membrane material has to be stable in the gaseous atmosphere of the flue gas. Moreover, the SiO<sub>2</sub>-membranes will need to operate in the atmosphere with humidity and water vapour below 300 °C for long term. As mentioned in 3.3.5, the silica surface will interact with water vapour due to its limited hydrothermal stability. Therefore, it is important to ascertain to which degree the selected membrane material will be altered from exposure to the fuel gas with humidity at operating temperatures and for long periods of time. Since it was not possible to carry out long term permeation experiments with synthetic flue gas and water vapour in the permeation set-up, long term annealing experiments were conducted in a furnace (Type ERO 2x7/60, Prüfer GmbH, Fig. 28) on the specimens. To analyse the influence of water vapour on the stability of silica membranes, CO<sub>2</sub> partial pressure gradient is not necessary.



Fig. 28 The set-up of long term annealing experiments.

In this work, the determination of the thermal stability of silica membranes for CO<sub>2</sub> capture in post-combustion process was carried out in the atmosphere of 85% N<sub>2</sub> and 15% CO<sub>2</sub> with gas flow of 50 ml/min and 1g/h water. This composition was used to simulate the operation conditions of flue gas in fossil fire power plant [133]. Meanwhile, the annealing tests with dry gas were also carried out in the permeation set-up at 150 °C, in order to determine the influence of moist on the CO<sub>2</sub> adsorption on the silica membrane.

Table 10 Various specimens under different annealing condition

Number of specimen	85% N <sub>2</sub> and 15% CO <sub>2</sub> (50 ml/min), 150 °C	85% N <sub>2</sub> and 15% CO <sub>2</sub> (50 ml/min), 1g/h water, 300 °C
Silica membrane on Atech substrate	1	1
Silica membrane on IEK-1 substrate	1	1
Amino-modified silica membrane on IEK-1 substrate	1	1

The gas flow rates were controlled by mass-flow meters (WMR 4000, Westphal Mess- und Regeltechnik) in the range of 0 to 50 ml/min. Humidification of the gas stream is conducted by direct introduction of liquid water, through a quartz glass capillary, in the hot zone of the furnace, where it is vapourised. This technique was chosen to minimise the cost of the set-up. The water flow rate was controlled by a water-flow meter ( $\mu$ -FLOW, Bronkhorst) in the range of 0 g/h to 15 g/h. In order to prevent back diffusion of air from the gas outlets into the system, the exhaust gas was transferred a through silicon oil glass bubbler. The glass bubbler was also

used to collect the water leaving the system. As the default heating program of the furnace was installed for high temperature range at 800 °C, the temperature controller (IMAGO 500, JUMO GmbH & Co. KG) had been adjusted for an operating temperature range at 300 °C.

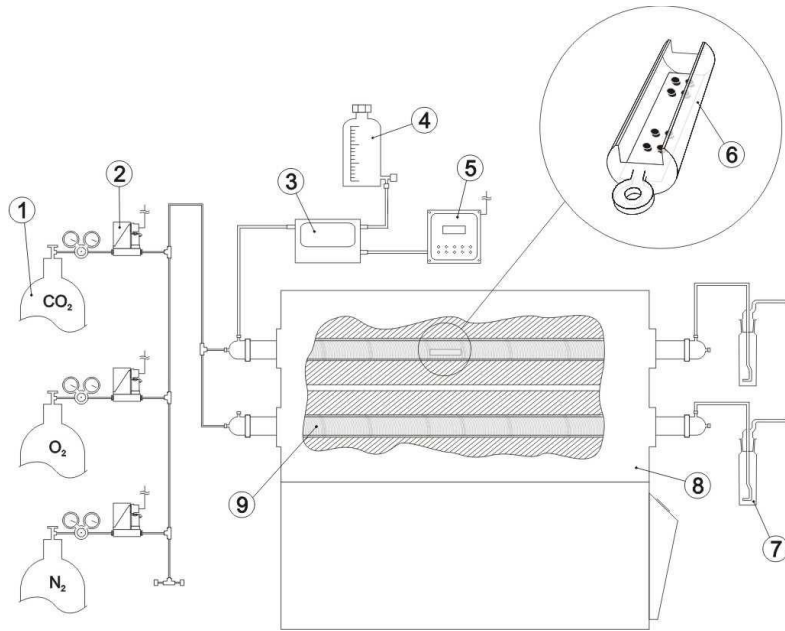


Fig. 29 Schematic representation of the stability test set-up, with 1) the gas bottles, 2) the mass flow meters, 3) the water-flow meter, 4) the water container, 5) the flow controller unit, 6) the ceramic sample holder, 7) the gas bubblers, 8) the tube furnace and 9) the quartz glass tubes.

## 5.4 Determination of mechanical properties

### 5.4.1 Ring-on-ring bending test

Young's modulus and fracture stresses were determined using bi-axial ring-on-ring bending test. The linear bending theory is used to determine the fracture stress since brittle ceramic materials usually fail after mainly elastic deformation.

The central displacement of the specimen was recorded with a sensor that contacted the lower surface of the sample. All the ring-on-ring bending tests were carried out at room temperature, under ambient air, with a loading rate of 100 N/min. the displacement was measured with a ceramic extension rod attached to a linear variable differential transformer (Sangamo, LVDT). The load was determined with a 1.5 kN load cell (Interface 1210BLR). All investigated samples fractured at a displacement value much smaller than half of the specimen thickness, which is a prerequisite for the linear elastic stress–strain analysis (ASTM C1499-05). The

mechanical properties were determined from the fracture stresses and load - displacement data obtained in ring-on-ring bending. Diameters of load ring and support ring were 11 mm and 25 mm respectively. Details of the ring-on-ring fracture tests along with the equations used for evaluation can be found in [134]. Characteristic strength  $\zeta_0$  and Weibull modulus  $m$  were derived using linear regression.

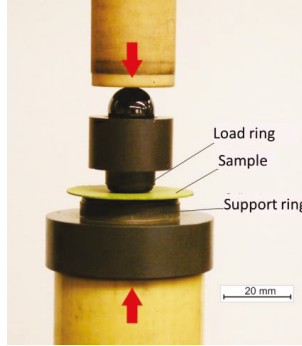


Fig. 30 Set-up of the ring-on-ring bending test (source: IEK-2, FZJ)

In addition, the Young's modulus is determined using the following equations:

$$E = \frac{3(1 - \nu^2) \cdot r_1^2 \cdot \Delta F}{2\pi \cdot \Delta f \cdot h^3} \times \left[ \left( \frac{r_2}{r_1} \right)^2 - 1 - 2 \ln \left( \frac{r_2}{r_1} \right) + \frac{1}{2} \left( \frac{1 - \nu}{1 + \nu} \right) \times \left( \frac{r_2^2 - r_1^2}{r_3^2} \right) \times \left( \frac{r_2^2}{r_1^2} \right) \right] \quad (\text{Equ. 11})$$

where  $\Delta F$  is the force,

$\Delta f$  the deflection,

$E$  the Young's modulus,

$\nu$  the Poisson's ratio (0.24 for ceramic) [135],

$h$  the specimen's thickness,

$r_1$  the radius of load ring,

$r_2$  the radius of support ring and

$r_3$  the radius of the specimen.

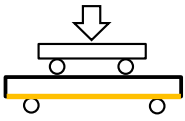
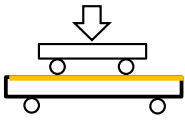
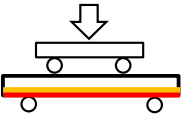
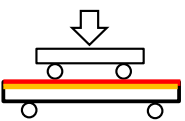
Accordingly, the strain can be calculated with the following equation:

$$\varepsilon = \frac{\sigma_B}{E} \quad (\text{Equ. 12})$$

In order to determine the influence of the coating system on the mechanical properties of the whole specimen, the fracture strengths of uncoated and coated specimens were tested in the

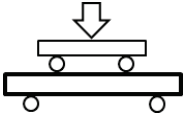
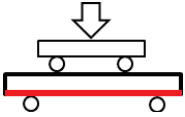
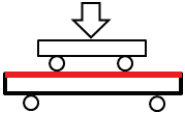
ring-on-ring bending tests according to the following load configuration (Table 11 and Table 12).

Table 11 Loading configuration and number of tested specimens with Atech substrate investigated in ring-on-ring bending test

	Loading configuration	Amount of specimens
	$\alpha$ -Al <sub>2</sub> O <sub>3</sub> substrate suspension layer on tensile side	11
	$\alpha$ -Al <sub>2</sub> O <sub>3</sub> substrate suspension layer on compressive side	11
	SiO <sub>2</sub> membrane, functional layer on tensile side	10
	SiO <sub>2</sub> membrane, functional layer on compressive side	10

Unlike to the tests of specimens with Atech substrate, the IEK-1 substrate does not have an additional suspension layer. Thus, there are only three loading configurations applied, i.e. “ $\alpha$ -Al<sub>2</sub>O<sub>3</sub> substrate”, “SiO<sub>2</sub> membrane on tensile side” and “SiO<sub>2</sub> membrane on compressive side”.

Table 12 Loading configuration and number of tested specimens with IEK-1 substrate investigated in ring-on-ring bending test

	Loading configuration	Amount of tested specimens
	$\alpha$ -Al <sub>2</sub> O <sub>3</sub> substrate	11
	SiO <sub>2</sub> membrane, functional layer on tensile side	7
	SiO <sub>2</sub> membrane, functional layer on compressive side	7

#### 5.4.2 Acoustic emission test

Unlike the specimens with ceramic substrates, the metal substrate can resist large plastic formation. For this reason, the bonding between the coating system and the substrate is crucial. In order to analyse the failure behaviour, it is to be determinate that when the cracks form and how they grow in the ceramic coating layers.

In this work, the investigation for the mechanical stability of the coating system during the deformation with the metal carrier was achieved through ring-on-ring bending test combining with for acoustic emission testing unit (AMSY-5, Vallen Systeme GmbH) (Fig. 32).



Fig. 31 Acoustic emission testing unit (AMS5, Vallen Systeme GmbH)

The load was increased here with a constant load rate of 100 N / min to 1000 N before unloading. During the deformation, if cracks form and grow in the specimen, acoustic signals will be produced. Such signals can be recorded by the acoustic emission testing unit.

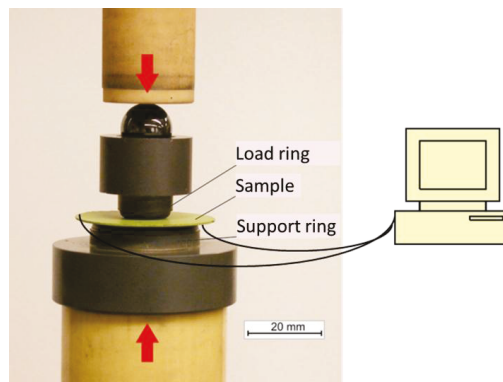


Fig. 32 Schematic principle of set-up of ring-on-ring bending test combined with acoustic emission testing unit (source: IEK-2, FZJ)

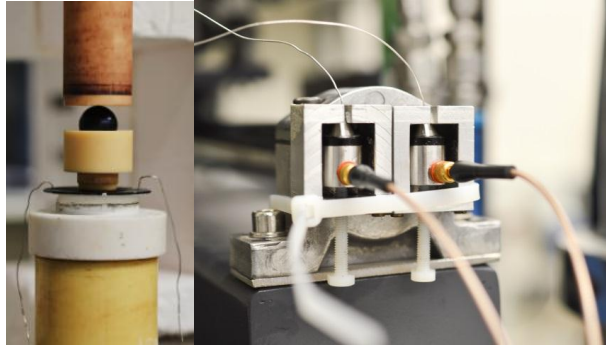


Fig. 33 Combination of ring-on-ring bending testing unit and acoustic emission testing unit (source: IEK-2, FZJ)

Table 13 Number of specimens for pre-bending tests

Loading configuration	Max. Force (N)	Number of specimens
Suspension layer on tensile side	1000 N	1
Suspension layer on compressive side	1000 N	1
Suspension layer on tensile side	2000 N	1

Table 14 Number of specimens for bending tests with acoustic emission tests

Loading configuration	Max. Force (N)	Number of specimens
Uncoated substrate	1000 N	1
Suspension layer on tensile side	1000 N	1
Membrane on tensile side	1000 N	2

### 5.4.3 Indentation test

To assess the materials Young's modulus and Vickers hardness impressions were induced in polished cross-sections by micro-indentation and nano-indentation. Indentation is a commonly applied means of testing the mechanical properties of materials.

The Young's modulus is determined with the help of the unloading curve during indentation testing, where only elastic recovery takes place, see Fig. 34.

The indentation technique is based on the principle of shifting an indenter perpendicular into the material surface so that only small volumes are tested. The depth ( $h$ ) is measured

during indentation. A Vickers indenter in the shape of a sharp diamond tip is used in this work. The angle of two diagonal sides is  $136^\circ$ . During the loading-unloading, the indenter leaves behind a permanent impression in the material. Details on the used relationships can be found in [136].

In this work Vickers hardness impressions were induced using a micro-indentation device (Helmut Fischer KG, Germany) with a maximum applied load of 1 N, and a nano-indentation device (CSM, Switzerland) with a maximum load of 500 mN.

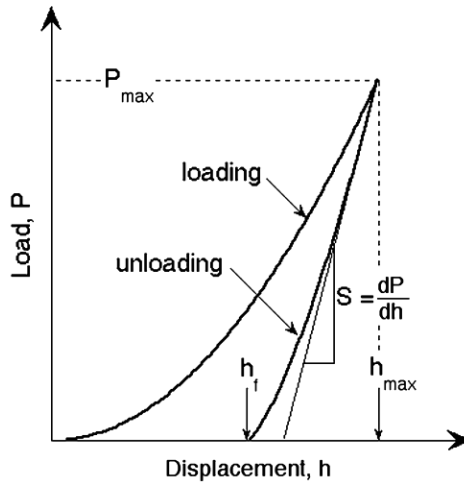


Fig. 34 Schematic representation of a typical indentation load-displacement [137]

## 5.5 Microstructure identification

### 5.5.1 Scanning electron microscopy (SEM)

Scanning electron microscopy (SEM) is a method for high-resolution images of sample surfaces that uses electrons for imaging. An incident beam of monochromatic electrons is raster-scanned over the sample's surface, and the resulting electrons emitted from the sample are collected by detectors for common signal, e.g. high energy electrons (backscattered), low energy electrons (secondary) and excited X-rays (characteristic). By analysing electron backscatter diffraction (EBSD) the crystallographic surface orientation of individual crystalline grains within the microstructure can be determined. Secondary electron (SE) image can characterize the surface morphology and the cross-section of samples. Using SEM in combination with energy-dispersive X-ray spectroscopy (EDS) detector, which collects

excited X-rays, makes it possible to identify the composition of the different formed phases [138].

Two SEM devices were used to carry out the investigations, namely the Stereoscan LEO440 (Cambridge, U.K.) with an acceleration voltage (EHT) of 20 kV and the Zeiss Supra50VP with an acceleration voltage of 15 kV. The EDS analyses were performed with type ISIS 300 (Enysham, U.K.). The micrographs of the cross section were taken in the backscattered electron mode (EBSD). The interpretation of the X-ray pattern was performed using the Software INCA Energy/Wave. Furthermore, the sample should be conductive in order to avoid charging effects. This is achieved by coating the sample in vacuum with platinum using a sputter coater.

### **5.5.2 Infrared spectroscopy**

To determinate the degradation of pure silica surface and modified silica surface after annealing tests, the specimens were analysed through infrared spectrometry. The analyses were carried out by the central department for chemical analysis (ZEA-3) in Forschungszentrum Jülich.

The measuring principle is based on the excitation of energy states in molecule, which thereby permits to extract information on the chemical bonding in substances. Substances generally exhibit with the property that they adsorb certain frequency ranges during the irradiation of electromagnetic waves. Since the energy of infrared light has a wavelength of 800 nm to 0.5 mm in the frequency range of the vibrational levels of molecular bonds, bond vibrations are excited by the adsorption, which can be seen as peaks in the measured spectrum. Since bonds are allocated according to characteristic energies or frequencies, it is possible to identify materials with this method [139, 140].

In this work, the annealed specimens (see Table 10) were analysed with infrared reflexion and absorption (IRAS) in ZEA-3. During this method, the IR radiation is sent nearly parallel onto the sample. Since with this measuring method the intensity is much lower than with the transmission, this technique is particularly suitably for layer systems/coatings [139]. In this work, the infrared spectrometer (SENSOR 27) with a room temperature DLATGS detector is manufactured by Bruker Corporation.



## 6 Results and discussion

### 6.1 Characterization of membranes with different substrates

#### 6.1.1 SiO<sub>2</sub>-membrane with ceramic Atech substrate

The layered structure of SiO<sub>2</sub>-membrane with ceramic Atech substrate is exemplified in Fig. 35. The  $\alpha$ -Al<sub>2</sub>O<sub>3</sub> substrate was already coated with two suspension layers on one side. Both suspension layers are composed of  $\alpha$ -Al<sub>2</sub>O<sub>3</sub> and the pore size decreases from substrate to the suspension layer 1 (Table 15). The completely coated specimen coated completely has additionally a  $\gamma$ -Al<sub>2</sub>O<sub>3</sub> interlayer and a SiO<sub>2</sub> function layer.

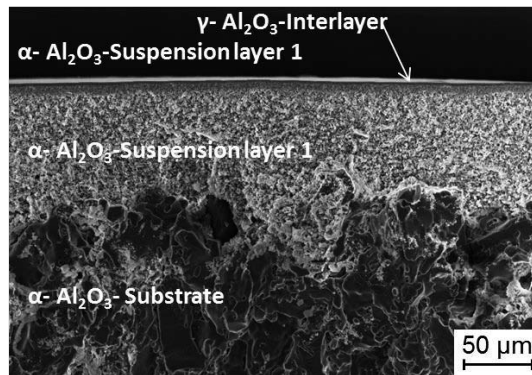


Fig. 35 Fracture surface of specimen with Atech substrate (source: IEK-1)

Table 15 Pore size from substrate to suspension 2 of Atech substrate (Source: IEK-1)

Layer	Pore size ( $\mu\text{m}$ )
Suspension layer 2	0.05
Suspension layer 1	0.2
Substrate	5 - 8

#### 6.1.2 SiO<sub>2</sub>-membrane with ceramic IEK-1 substrate

##### 6.1.2.1 Pure SiO<sub>2</sub>-membrane with ceramic IEK-1 substrate

Fig. 36 is a SEM image of cross-section of the uncoated and coated specimen's side. It shows schematically the layer structure of the specimen. The substrate material is also  $\alpha$ -Al<sub>2</sub>O<sub>3</sub> like Atech substrate. The completely coated samples have an additional interlayer from  $\gamma$ -Al<sub>2</sub>O<sub>3</sub> with a thickness of 4  $\mu\text{m}$  and a functional layer of SiO<sub>2</sub> with a thickness of 100 nm.

The side of the substrate to be coated was polished (Fig. 36 left), which is reflected in a difference contrast. Fig. 36 right shows the side of the substrate after coating. On the substrate,

there is the intermediate layer of  $\gamma$ -Al<sub>2</sub>O<sub>3</sub>, which was deposited by a 2-step coating process and has a pore size of about 4 nm. In this image the thin SiO<sub>2</sub> layer with a pore size smaller than 1 nm cannot be seen clearly.

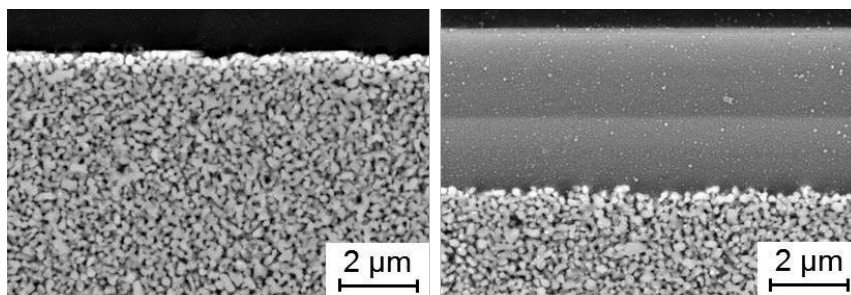


Fig. 36 SEM images of cross section of the specimen side to be coated (left) and coated (right)

#### 6.1.2.2 Amino-modified SiO<sub>2</sub>-membrane with ceramic IEK-1 substrate

The SEM image of cross-section of amino-modified SiO<sub>2</sub>-membrane with ceramic IEK-1 substrate is shown in Fig. 37. The Kelvin radius has a distribution from 0.5 nm to 1.5 nm, measured by He- permporosimetry (Type EKR, Fraunhofer IKTS) [25]. The completely coated samples have an additional interlayer from  $\gamma$ -Al<sub>2</sub>O<sub>3</sub> with a thickness of 5  $\mu$ m and a functional layer of SiO<sub>2</sub> with a thickness of 100 nm.

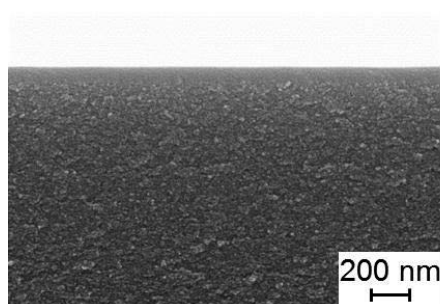


Fig. 37 left:  $\gamma$ -Al<sub>2</sub>O<sub>3</sub>-interlayer with modified silica layer on top [25]

#### 6.1.3 SiO<sub>2</sub>-membrane with metallic ITM substrate

The substrate is made of the alloy ITM (Intermediate- Temperature- Metal). On the substrate, two 8YSZ suspension layers are deposited (Fig. 38). The thicknesses of the two suspension layers are approximately 100  $\mu$ m for the lower layer and 30  $\mu$ m for the upper layer. The completely coated samples have an additional interlayer from  $\gamma$ -Al<sub>2</sub>O<sub>3</sub> with a thickness of 3  $\mu$ m and a functional layer of SiO<sub>2</sub> with a thickness of 100 nm.

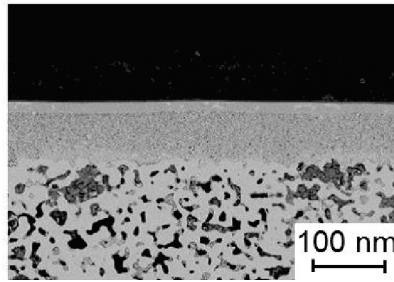


Fig. 38 SEM image of cross section of the ITM substrate with two 8YSZ suspension layers (source: IEK-1)

#### 6.1.4 Porosity of Atech substrate and IEK-1 substrate

The porosity of the IEK-1 and Atech substrates was measured by mercury porosimetry. The measurements for both substrates result in almost the same porosity value of 42.0 % and 43.5 %. The pore size of the Atech substrates is about 2 to 5  $\mu\text{m}$  and the IEK-1 substrates about 30 to 40 nm. This means that Atech substrate is microporous and IEK-1 substrate nanoporous.

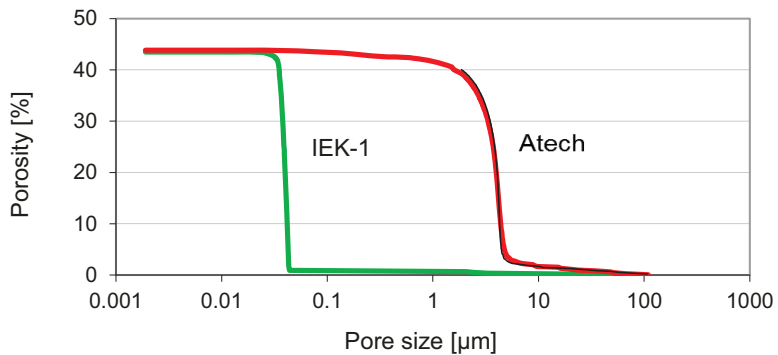


Fig. 39 Porosity and pore size distribution of Atech and IEK-1 substrates measured by mercury porosimetry

## 6.2 Mechanical properties

### 6.2.1 Mechanical properties of porous ceramic substrates

In order to determine the influence of the coating system on the mechanical properties of the whole specimen, the fracture strengths of uncoated and coated specimens were tested in the ring-on-ring bending tests according to the load configuration “SiO<sub>2</sub> membrane on tensile side” and “SiO<sub>2</sub> membrane on compressive side”.

#### 6.2.1.1 SiO<sub>2</sub>-membrane with ceramic Atech substrate

Since the uncoated substrates had already two suspension layers, it was necessary to carried out also ring-on-ring bending tests in the load configuration “suspension layer on tensile side” and “suspension layer on compressive side” to assess the influence of the suspension layers.

A Weibull-plot of the fracture strengths of all specimens with Atech substrate is shown in Fig. 40. Derived, characteristic fracture stress  $\zeta$  and Weibull modulus  $m$  are given in Table 16.

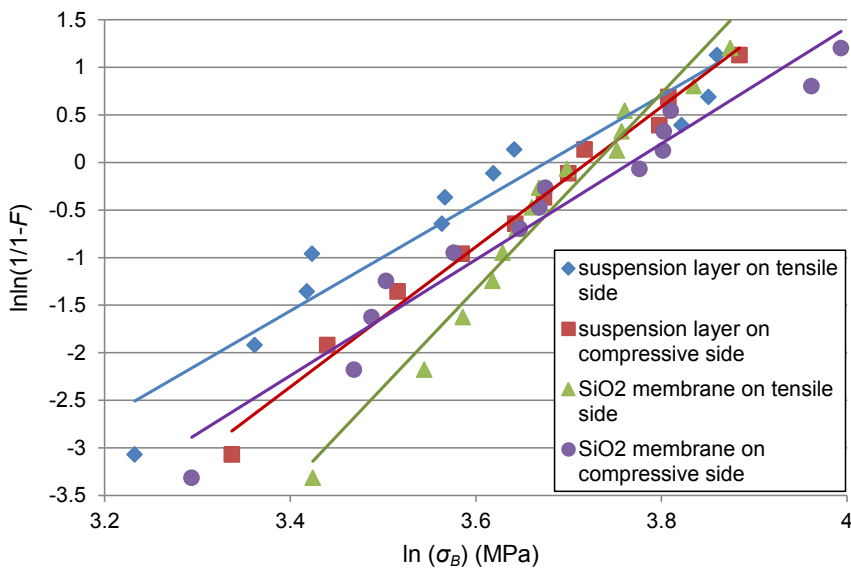


Fig. 40 Weibull-plot of fracture strengths of all specimens with Atech substrate

The characteristic fracture stresses are between 39 and 43 MPa. The coating system does not affect the characteristic fracture stress within the experimental uncertainty; also a slight indication for an increased strength in the case of specimens with membrane top layer might be seen. Also Weibull moduli agree within the limits of uncertainty. Therefore, the strength of the specimens is determined by the fracture strength of the substrates.

Table 16 Results of ring-on-ring bending test of specimens with Atech substrate in various loading configurations and calculated Weibull parameters (characteristic fracture stress and Weibull modulus)

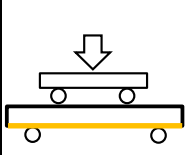
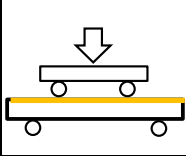
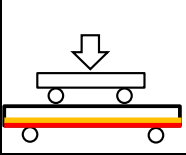
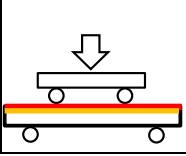
	Loading configuration	Characteristic fracture stress (MPa)	Weibull modulus ( $m$ )
	$\alpha$ -Al <sub>2</sub> O <sub>3</sub> substrate suspension layer on tensile side	39 ± 2	6 ± 2
	$\alpha$ -Al <sub>2</sub> O <sub>3</sub> substrate suspension layer on compressive side	41 ± 2	7 ± 2
	SiO <sub>2</sub> membrane, functional layer on tensile side	42 ± 1	10 ± 3
	SiO <sub>2</sub> membrane, functional layer on compressive side	43 ± 2	6 ± 2

Fig. 41 shows a SEM-image of fracture surfaces of an Atech substrate. It is obvious that the crack grows mainly along the grain boundaries. The red circle marks an inter-crystalline break area with clearly step shear cleavage structure, indicating that the strength of the specimens is determined, in addition to the size and distribution of defects, by the mechanical properties of the of  $\alpha$ -Al<sub>2</sub>O<sub>3</sub> substrate grain boundaries.

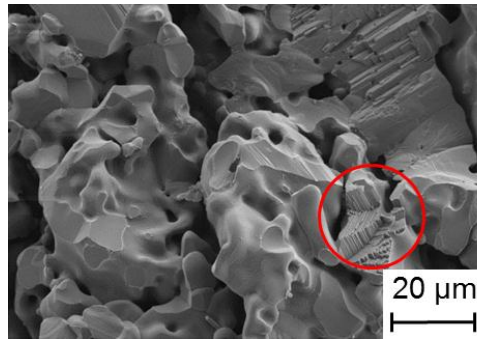


Fig. 41 SEM-image of fracture surfaces of Atech substrate after ring-on-ring bending test (fracture stress = 37 MPa)

### 6.2.1.2 $\text{SiO}_2$ -membrane with ceramic IEK-1 substrate

Fig. 42 shows the Weibull plot of fracture strengths of all the specimens with IEK-1 substrate as determined via ring-on-ring bending testing. The plot compares the characteristic fracture stresses and Weibull moduli with respect to the various loading configurations. Unlike to the tests of specimens with Atech substrate, the IEK-1 substrate does not have an additional suspension layer. Thus, there are only three loading configurations applied, i.e. “ $\alpha\text{-Al}_2\text{O}_3$  substrate”, “ $\text{SiO}_2$  membrane on tensile side” and “ $\text{SiO}_2$  membrane on compressive side”.

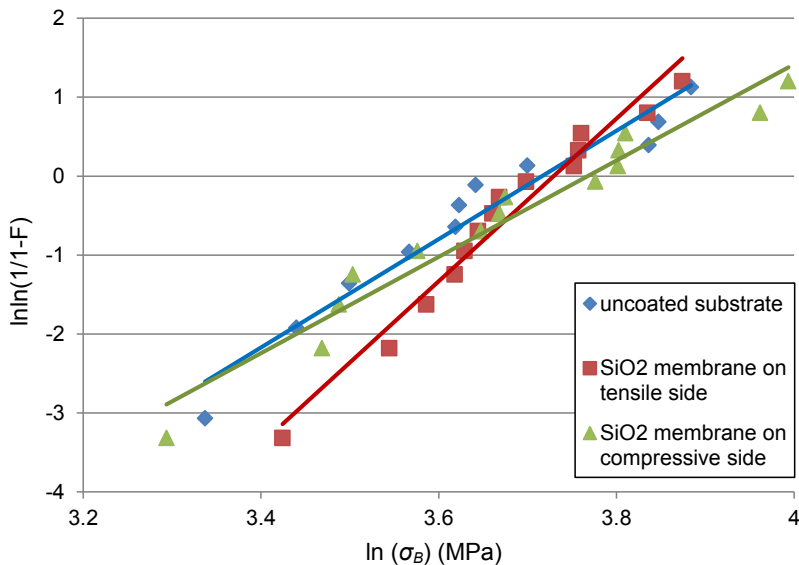
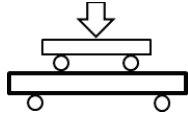
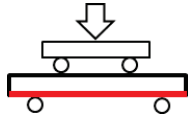
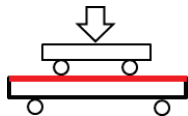


Fig. 42 Weibull-plot of fracture strengths of all the specimens with IEK-1 substrate

For uncoated substrates and the case of “ $\text{SiO}_2$  membrane on tensile side”, the characteristic fracture stresses  $\zeta_B$  are almost identical. In contrast, for the loading configuration “ $\text{SiO}_2$

membrane on compressive side”, the derived  $\zeta_B$  is lower and the Weibull modulus  $m$  appears to be higher.

Table 17 Results of ring-on-ring bending test of specimen with IEK-1 substrate tested in various loading configurations and calculated Weibull parameters (characteristic fracture stress and Weibull modulus)

	Loading configuration	Characteristic fracture stress (MPa)	Weibull modulus ( $m$ )
	$\alpha$ -Al <sub>2</sub> O <sub>3</sub> substrate	161 ± 23	2 ± 1
	SiO <sub>2</sub> membrane, functional layer on tensile side	167 ± 23	3 ± 1
	SiO <sub>2</sub> membrane, functional layer on compressive side	142 ± 9	6 ± 2

In the interpretation of the Weibull diagram it should be considered that the number of tested specimens for statistical Weibull analysis is rather low and can only be used as a guideline for the assessment for the materials' failure behaviour. The coating itself does not appear to affect the fracture stress as seen from the data with the coating under tension, hence the coating does not appear to reduce the defect size which might suggest that failure occurs from volume and not surface defects. The data with the coating under compression rather surprisingly indicate an increase in strength, which in this case surely cannot be related to crack healing, it can rather be suggested that the increase is related to residual stresses that are induced by the coating process, which agrees also with the slight kink observed in the Weibull plot, i.e. a two parameter Weibull distribution can change to a three parameter distribution due to residual stresses. Residual stress induced by the coating process should be approximately equal to the difference in strength of coated and uncoated material, i.e. around 20 MPa. Currently it is unclear why the tests with Atech substrate did not reveal such an effect.

Fig. 43 and Fig. 44 show the fracture surfaces of the IEK-1 specimens that failed at the lowest and highest fracture stress under different loading configurations, respectively. For the

specimens with the highest fracture stress, the fracture surface shows a clear edge between interlayer and substrate, i.e. at higher elastic energies the crack path is affected by the layer. The interlayer of the sample with the highest fracture stress has a significantly smoother fracture surface as the interlayer of the sample with low fracture stress. This phenomenon was not observed for fracture surfaces of the specimens with Atech substrates (Fig. 45). It could be explained through the fact that the substrates from Atech possess two suspension layers with a thickness of 60  $\mu\text{m}$  and 5  $\mu\text{m}$ , respectively, hence the crack path grows more like in a graded structure, i.e. this transition eases the abrupt change of stress between interlayer and substrate (Fig. 46), but the effect might also simply absent since the Atech material failed at lower loads and hence was always in the regime observed for the IEK-1 materials specimens that failed under the lower stresses. However, since this is the case for both loading configurations and tests with loading configuration layer under tension did not reveal a change in strength compared to the uncoated case, this difference in crack path did not affect the experimental results.

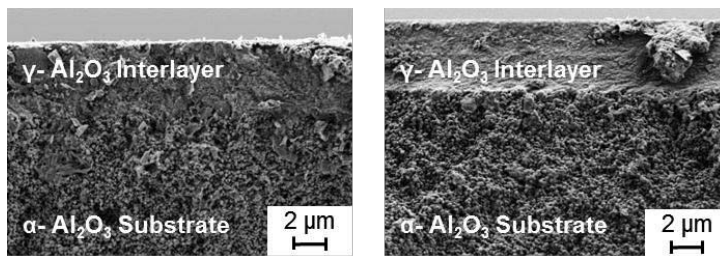


Fig. 43 SEM image close to the interlayer for fractured specimen with IEK-1 substrate after ring-on-ring bending test under the loading configuration “SiO<sub>2</sub> membrane on tensile side” (stress: left 92 MPa, right 213 MPa)

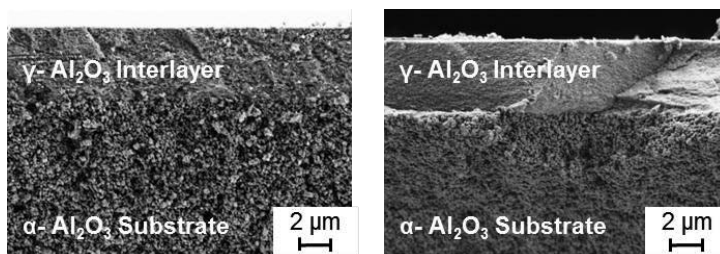


Fig. 44 SEM image close to interlayer for fractured specimen with IEK-1 substrate after ring-on-ring bending test under the load configuration “SiO<sub>2</sub> membrane on compressive side” (stress: left 103 MPa, right 171 MPa)

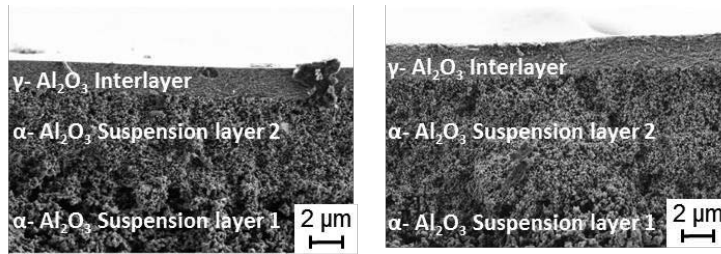


Fig. 45 SEM image close to the interlayer for fractured specimen with Atech substrate after ring-on-ring bending test under the loading configuration “SiO<sub>2</sub> membrane on tensile side” (stress: left 31 MPa, right 48 MPa)

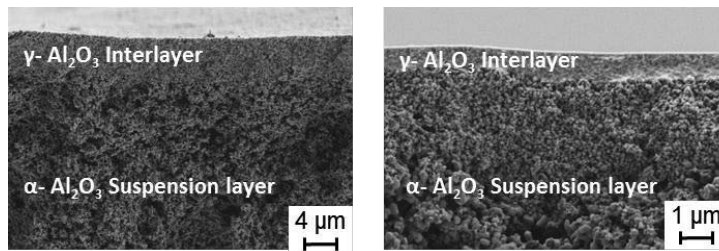
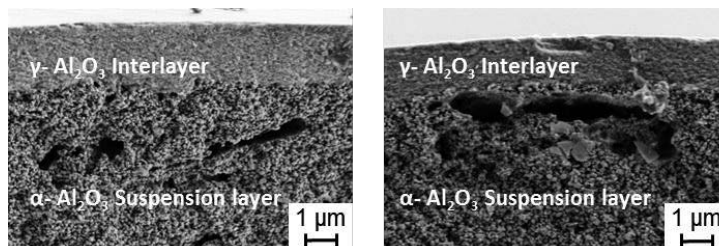


Fig. 46 SEM image close to interlayer for fractured specimen with Atech substrate after ring-on-ring bending test under the load configuration “SiO<sub>2</sub> membrane on compressive side” (stress: left 28 MPa, right 54 MPa)

Furthermore, another reason for neglecting the influence of the coating on the fracture behaviour of Atech substrate is the large in the suspension layer (Fig. 47). These defects often appearing in the layer connection and with the comparable pore size with that of the layer below are the start points of the crack growth, when the coated side is under tensile stress. In this case, the crack will directly grow through the substrate, like under the load configuration “SiO<sub>2</sub>-membrane on compressive side”.



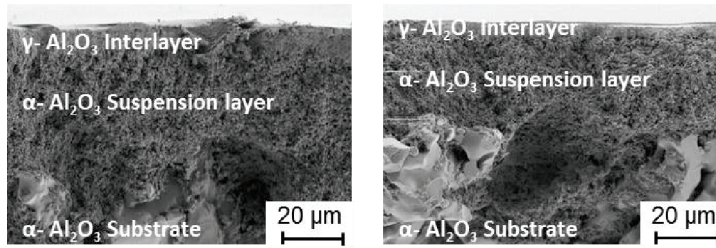


Fig. 47 Defects in the suspension layer of the specimens with Atech substrates.

### 6.2.1.3 Indentation tests

Nano- and micro-indentation tests were carried out for materials characterization with loads of 5 mN, 10 mN respectively. Typical loading and unloading curves of indentation tests carried out for Atech and IEK-1 substrates are shown in Fig. 48. Because of the fine microstructure, the loading curve for the IEK-1 substrate is relatively smooth. In contrast the loading curve on Atech substrate processes steps due to the rough microstructure and the large pores which affect the continuous movement of the indenter. This was also reflected in the indentation mark on the cross-section. Fig. 49 shows the clear indentation mark for the IEK-1 material. Contrary, it was not possible to distinguish the indentation mark on Atech substrates.

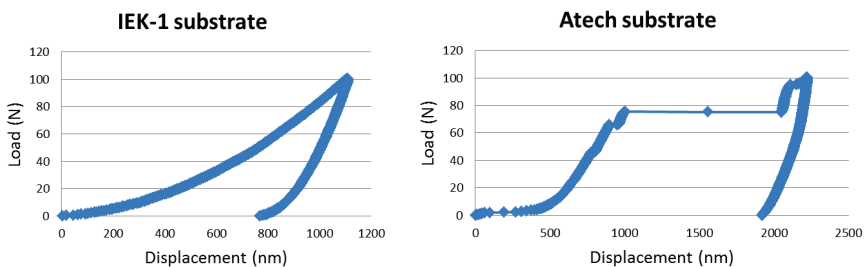


Fig. 48 Loading and unloading curves of nano-indentation test on Atech substrate and IEK-1 substrate

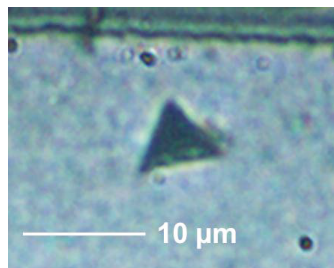


Fig. 49 Indentation mark on the cross section of the IEK-1 substrate

Fig. 50 compiles the Young's modulus of IEK-1 substrate measured by nano-indentation tests as a function of the indentation depth. At the very beginning, where the depth is much smaller than the particle size  $300\ \mu\text{m}$ , values of Young's modulus are much larger than the average value (red dash line in Fig. 50) reaching up to 250 GPa. Especially when the indentation depth is larger than 300 nm, the scattering of Young's moduli is so narrow that individual data are close to the average value.

For the Atech substrate, the coarse microstructure is also reflected by the measured values of Young's modulus (Fig. 51). When the indentation depth is smaller than 100 nm, the measured values of Young's moduli for the Atech substrate are significantly high than the values, which were measured for indentation depths between 400 nm to 700 nm.

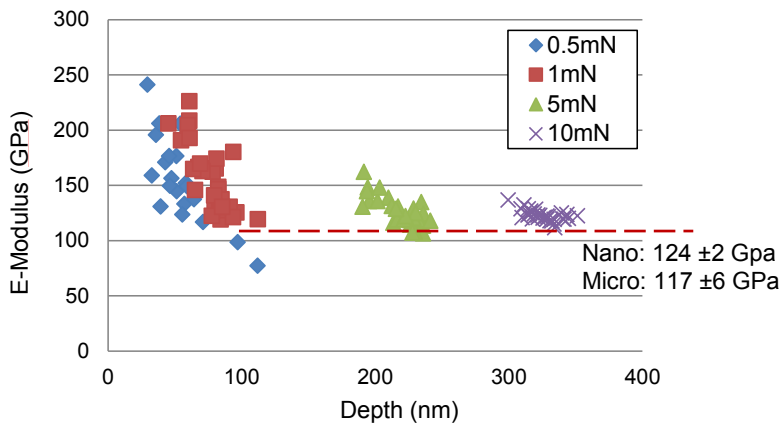


Fig. 50 Young's moduli of IEK-1 substrates measured by nano-indentation test as the function of indentation depth

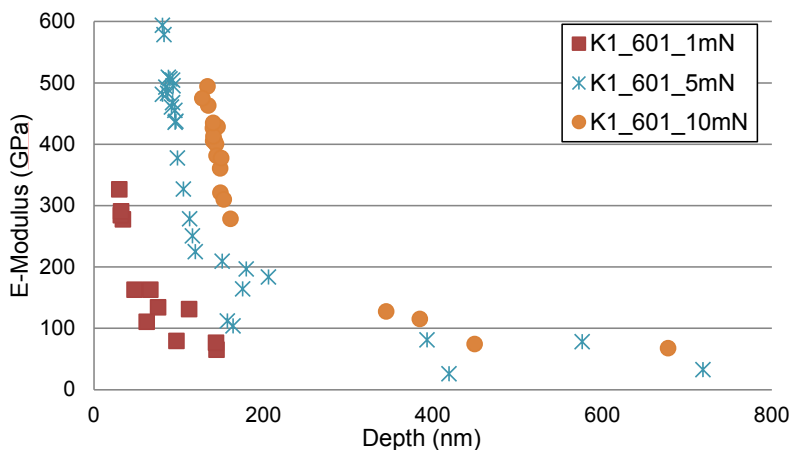


Fig. 51 Young's moduli of Atech substrates measured by nano-indentation test as the function of indentation depth

Since nano-indentation testing yields for very low loads only the local property of the material [141], the results should correspond to the literature value of alumina (Table 18 [142]). As the load and the depth increases, pores affect the deformation behaviour.

The average Young's moduli of the Atech and IEK-1 based substrates were  $379 \pm 6$  GPa and  $124 \pm 2$  GPa, respectively, where the maximal load was 10 mN. The Atech Young's modulus is similar to literature values (see Table 17), indicating that at these loads the behaviour of single grains is tested; the Young's modulus of the IEK-1 based material is affected by the pores even at these low loads due to the significantly smaller grain size.

The micro-indentation system permitted tests at larger indentation depths, although for the Atech powder based substrates the depth was still smaller than the average grain size of  $50 \mu\text{m}$ . Micro-indentation tests with the maximum available load of 1 N (average indentation depth  $20 \mu\text{m}$ ) yielded values of  $40 \pm 38$  GPa for the Atech and  $117 \pm 6$  GPa for the IEK-1 based material. Hence, data determined using the micro-indentation technique at this load appear to be already representative for the global behaviour of the porous material; note, the elastic zone is approximately ten times larger than the plastic zone.

Table 18 Young's modulus of  $\alpha\text{-Al}_2\text{O}_3$  [142]

E-modulus value	Condition
530 GPa	Single crystal
345 - 409 GPa	Polycrystalline, room temperature

#### 6.2.1.4 Summary and discussion of the results: specimens with ceramic substrates

Since the strength of all specimens with ceramic substrates appears to be determined by the substrate material, the results of various loading configurations were joined for each material and analysed as one data set each, except “SiO<sub>2</sub>-membrane, functional layer on compressive side” for specimens with IEK-1 substrate, because of the deviation of the characteristic fracture strength and Weibull-Modulus compared to the other loading configurations (Fig. 52).

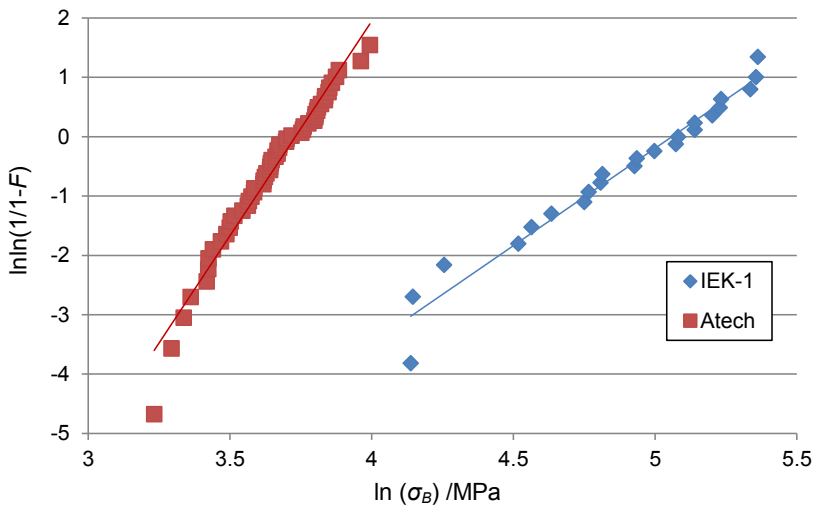


Fig. 52 Weibull plot of fracture strengths of all specimens with Atech and IEK-1 substrates, respectively

The calculated characteristic fracture stress is  $42 \pm 1$  MPa for Atech substrates and  $157 \pm 11$  MPa for IEK-1 substrates, furthermore, the Weibull modulus accounts to  $7 \pm 1$  for Atech substrates and  $3 \pm 1$  for IEK-1 substrates (Table 19).

Furthermore, the ring-on-ring bending test load-displacement curves yielded Young's moduli of  $48 \pm 10$  GPa for the Atech and  $102 \pm 13$  GPa for the IEK-1 substrates (see Table 19), i.e. again significantly higher values for the nano-porous material, which agreed, however, with the data obtained using micro-indentation ( $40 \pm 38$  GPa for the Atech and  $117 \pm 6$  GPa for the IEK-1 based material, see section 6.2.1.3).

Table 19 Characteristic fracture stresses, Weibull moduli and Young's moduli for Atech and IEK-1 substrates

	Atech Substrate	IEK-1 Substrate
Characteristic fracture stress [MPa]	$42 \pm 1$	$157 \pm 11$
Weibull-Modul ( $m$ )	$7 \pm 1$	$3 \pm 1$
E-Modul [GPa]	$48 \pm 10$	$102 \pm 13$

The IEK-1 substrates have higher fracture stresses than the substrate from Atech. Since both consist of  $\alpha$ -Al<sub>2</sub>O<sub>3</sub>, the reason can only be different microstructures, since both substrates possess almost the same, i.e. 42.0 % for IEK-1 substrate and 43.5 % for Atech substrate (Fig. 39).

This means, in spite of the similar porosity, the substrates exhibit still different characteristic fracture stresses. So the phenomenon can only be related to different grain sizes and contact areas between the grains. SEM images of fracture surfaces show that for both materials the cracks progress along grain boundaries (Fig. 53 (a), (b)). This means that the contact area is the weakest position and thus dominates strength and Young's modulus behaviour. This deduction will be discussed with the help of following literatures.

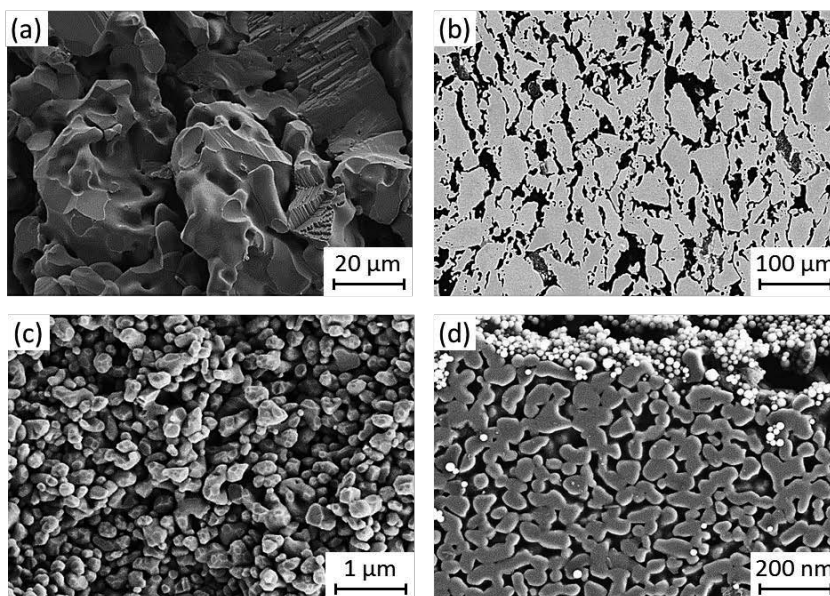


Fig. 53 Polished cross-sections and fracture surfaces, (a) (b) IEK-1 substrate, (c) (d) Atech substrate

It appears to be interesting in this context to compare the observed behaviour also to that reported in [143], where ceramic materials with different pore sizes between 50 and 500  $\mu\text{m}$  and porosities between 20 % and 48 % were characterized. A reanalysis of this data in Fig. 54 clearly shows that the discrete flexural strength data decrease with increasing pore size, similar as in the current study.

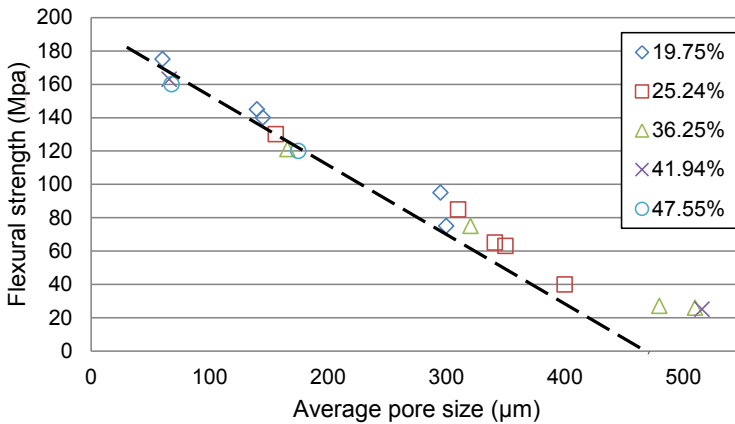


Fig. 54 Effect of pore size and porosity on the flexural strength on porous alumina compacts [143]

In other study Li et al. [144] characterized two types of  $\text{Al}_2\text{O}_3$  porous ceramics with different pore sizes. Type-A had a pore size distribution from 1 to 4  $\mu\text{m}$  and type-B from 0.4 to 2  $\mu\text{m}$ , yielding similar flexural strengths for porosities of 35 %, whereas for a porosity of around 45 % the flexural strength of type-A was much lower than that of type-B, i.e. the particles of smaller size appear still to have enough contacting points even at higher porosities. A similar effect has also been reported for ductile metallic materials. Wen et al. [145] found for magnesium foams with a porosity of 45% that both Young's modulus and compressibility peak stress decreased with increasing pore size.

Mathematical descriptions of strength - pore size effects are limited. Isobe et al. [146] observed that the 3-point bending strength of extruded alumina ceramics (porosity 39 %) decreased with increasing pore size and proposed a relationship suggested before by Ashizukat et al. [147] for alumina ceramics (porosity 10 and 20 %). It links bending strength ( $\zeta_c$ ) and pore size ( $d$ ):

$$\sigma_c \propto \frac{1}{\sqrt{d}} \quad (\text{Equ. 13})$$

But it was not possible to describe the current strength data by this equation (pores in their cases were isolated).

Liu found [148] that for the same porosity, ceramics with smaller macro-pore sizes could sustain a higher compressive strength and the strength revealed a stronger porosity dependence for larger macro-pore sizes.

Knudsen [149] developed a model upon the assumptions that: (a) the pores are formed by packing equal-sized spheres in a special array; (b) various porosity can be achieved by densifying to different densities; (c) the spheres attract to each other during densification, causing the contact area to increase, yet without disturbing the relative orientation of spheres, which means the pattern of array is no changed; (d) each deforming sphere maintains its original volume, and (e) the displaced materials redistributes itself evenly over the residual spherical surface; (f) the strength of an individual sphere is stronger than the cohesion of contacting area; and finally (g) the strength of a porous material is proportional to the load-bearing contact area.

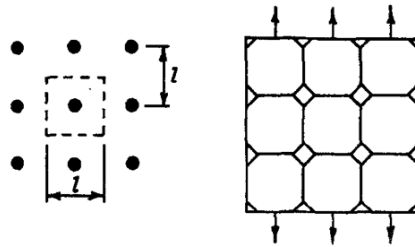


Fig. 55 Simple cubic array and unit cell [150]

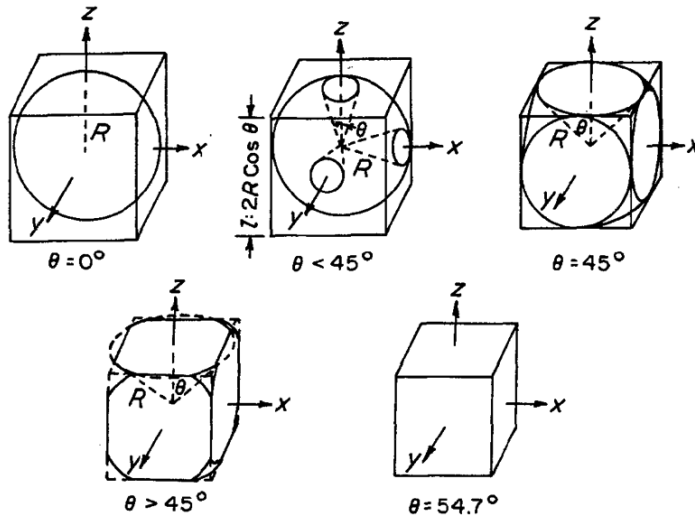


Fig. 56 Sequence of events upon densification [150]

Later, Wang [150] included the mathematical description of the Young's modulus porosity behaviour after Sprigg [146] into the ideas of Knudsen [149] yielding that the Young's modulus should depend on the total contact area between the grains.

The Atech powder based substrates were manufactured by an extrusion method. Therefore, the grain sizes are not uniform and the grain boundaries are also not smooth but with sharp angle. Hence, the ratio of contact area between unit grains with the neighbour grains in case of the Atech powder based substrate is smaller than that of IEK-1 substrate (Fig. 53), which is in good agreement with the behaviour expected from the Knudsen's model.

Both substrates have different pore sizes but the same porosity, hence, in case of a similar geometric arrangement of the grains, the number of contact points per unit volume is significantly larger for the IEK-1 based material (see also Fig. 53). Furthermore, pores lead to crack deflection and hence energy absorption and smaller pores can then lead to more crack deflection sites [151].

Table 20 Comparison of the mechanical properties of the different substrate materials

Consignment	Al <sub>2</sub> O <sub>3</sub> Atech	Al <sub>2</sub> O <sub>3</sub> IEK-1	MgO [107]	CGO [104]	BSCF [104]	LSCF [104]
Porosity	42	43.5	36	43	34	46
$E$ [GPa ]	$48 \pm 10$	$102 \pm 13$	$55 \pm 3$	$57 \pm 14$	$35 \pm 3$	$12 \pm 4$
$\zeta_0$ [MPa ]	$42 \pm 1$	$157 \pm 11$	$41 \pm 2$	$55 \pm 3$	$31 \pm 1$	$18 \pm 2$
Fracture strain	0.088	0.15	0.075	0.096	0.089	0.15
$m$	$7 \pm 1$	$3 \pm 1$	$19^{+5}_{-7}$	$4 \pm 2$	$5 \pm 2$	$4 \pm 2$

The Atech based material has a similar Young's modulus and strength as the other materials quoted in Table 20, whereas the IEK-1 powder based alumina has a significantly higher Young's modulus and strength than the other materials, even though porosities are similar.

A comparison can also be based on the fracture strain determined as the ratio of strength to Young's modulus. It can be seen that fracture strain of the IEK-1 powder based alumina is the highest of all quoted materials, hence proving again that this material is mechanically superior. However, the low Weibull modulus indicates that there is still space for materials improvement.

## 6.2.2 Mechanical properties of porous metallic substrate

The metallic substrates have a good ductility during deformation in contrast to ceramic substrates. However, this significant difference in the formability might also result in a peeling of the fragile layers and hence, it is important to investigate the crack creation and growth in the layers on metallic substrates.

### 6.2.2.1 Ring-on-ring bending tests of metallic substrates coated with 8YSZ suspension layer

As primary tests, three metallic substrates coated with 8YSZ suspension layer were characterized using the ring-on-ring bending tests to investigate initially the loading strength, which could produce cracks of the coating layers. The test set-up is same as used for the ceramic composite membranes.

There were two available types of bending test machine with maximal load of 1000 N and 2000 N respectively. With a maximum load of 1000 N, the loading and unloading curves of the bending tests were almost identical for the arrangements “suspension layer on tensile side” and “suspension layer on compressive side” (Fig. 57). Fig. 58 shows the specimens after deformation in the ring-on-ring bending tests. In this case, the specimens were deformed only to a minor extend (Fig. 58 (a) and (b)) and there was no obvious peeling of the suspension layer.

After increasing the maximum load to 2000 N, the peeling was observed for the loading configuration “suspension layer on tensile side” (Fig. 58 (c)), at a deformation of 982  $\mu\text{m}$  (1853 N) (Fig. 57).

For the thin layer on the metallic substrate did not affect the linear deformation behaviour (Fig. 57) and there is only small deflection, the strain of the specimen can still be calculated with the equation of Young’s modulus (Equ. 11) [134, 152], with a ITM Poisson’s ratio of 0.29 [108].

It was verified that the delamination of the 8YSZ suspension layer will occur at the load of 1853 N when the layer was tested in tension. Accordingly, the corresponding stress is 905.5 MPa and corresponding strain is 1.12 % (Equ. 14). Because Young’s modulus of dense ITM is 206 GPa and Young’s modulus of porous ITM with a porosity of 38 % is 53 % (see Table 3), the calculated Young’s modulus of 80.6 GPa for porous ITM with a porosity of about 36 % appears to be realistic for a porous metallic material..

In order to determine whether there were micro-cracks forming during deformation, the machine with maximal load of 1000 N was used to the following ring-on-ring bending tests for the specimens with metallic substrate.

The similarity of the hysteresis for the test with layer in compression and tension indicate that even at 1000 N substrate plasticity affects the results. The limited number of specimens did not permit an accurate determination of the critical strain for plastic deformation based on these results and was aided by the tests with acoustic emission detection described in the following subsection.

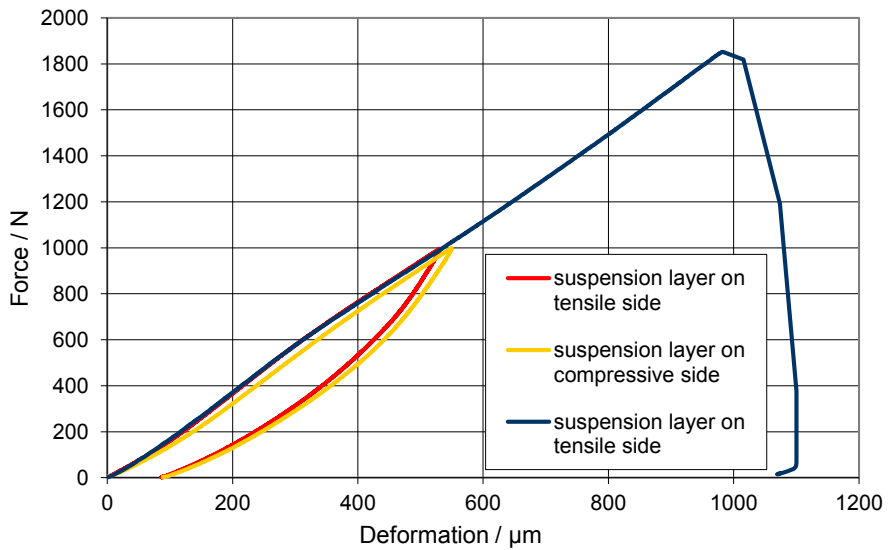


Fig. 57 Loading and unloading curves of ring-on-ring bending test with metal substrates coated with 8YSZ suspension layer

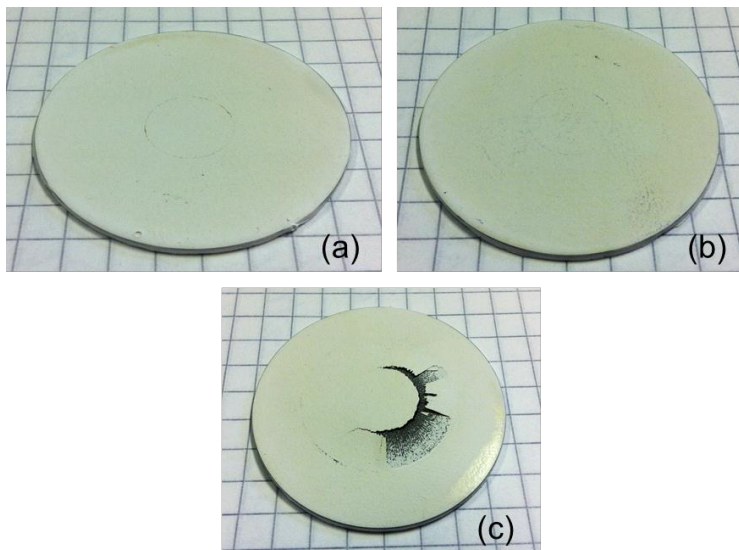


Fig. 58 Specimens (diameter 39 mm) consisting of metal substrate and suspension layer after ring-on-ring bending tests: (a) suspension layer on tensile side (1000 N), (b) suspension layer on compressive (1000 N), (c) suspension layer on tensile side with maximal load of 2000 N.

### 6.2.2.2 Ring-on-ring bending test with acoustic emission detection for specimens with metallic substrates

In order to analyse the failure behaviour in more detail and to characterize the origin of the cracks growing in the coating system complementary tests with acoustic emission detection were carried out. For this purpose, the following specimens were investigated: uncoated metallic substrate, substrate coated with 8YSZ suspension layers and a completely coated specimen which consisted of substrate, 8YSZ suspension layers and  $\gamma$ -Al<sub>2</sub>O<sub>3</sub> interlayer from and SiO<sub>2</sub> functional layer. For all specimens, tests were carried out with the coating layers were on the tensile side.

Fig. 59 shows the deformation curves of the specimens during the bending tests as function of the test time. Again the loading rate was 100 N/min and the maximal load 1000 N, where the deformation of the specimens also reached the largest value. However, there is an obvious difference between the behaviours of the investigated specimens. The uncoated substrate has a deformation of about 725  $\mu\text{m}$ , the one coated with a suspension layer for the same load, only 620  $\mu\text{m}$ . Furthermore, for a completely coated specimen with suspension layer, interlayer and functional membrane, the maximal deformation was even less accounting to  $\sim$  460  $\mu\text{m}$ .

This indicates that the stiffness of the porous metallic substrate was enhanced by the ceramic coating layers due to their lower porosity. Obviously, the apparent stiffness of the entire specimen increases with the number, hence total thickness, of the stiff ceramic coating layers (Table 21).

Table 21 Young's modulus and deformation of various specimens

Specimen	Deformation ( $\mu\text{m}$ )	Apparent Young's modulus (GPa)
Substrate	977	37.6
Substrate, suspension layer	620	59.7
Substrate, suspension layer, interlayer, functional membrane	467	76.2

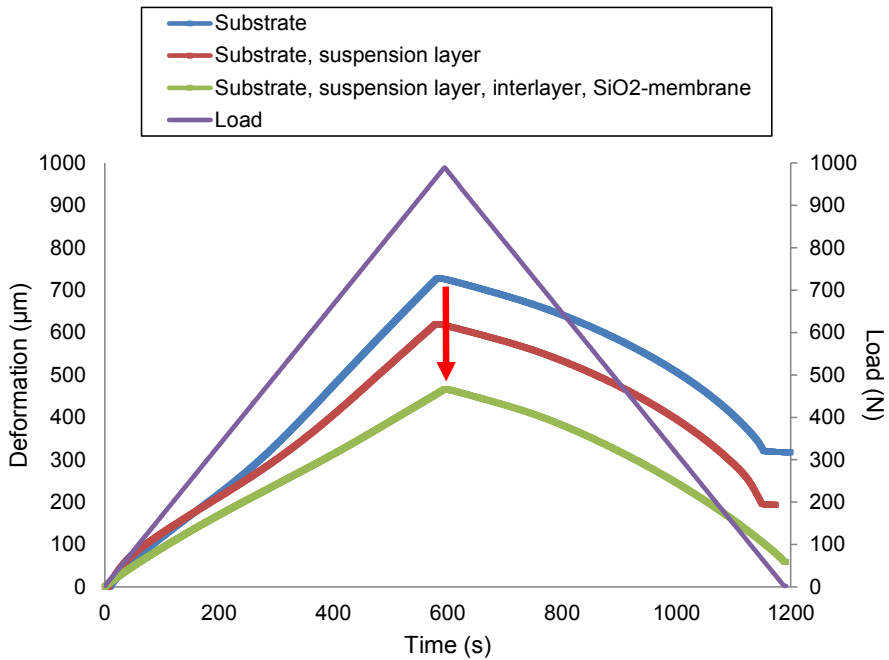


Fig. 59 Deformation of uncoated, partially coated and completely coated specimen as a function of time

Fig. 60 shows the acoustic emission signal as function of test time, in terms of the number of counts obtained in a coincidence mode. It can be seen that only the completely coated specimen shows a significant amount of emissions.

The deformation reached the peak value at the maximal load of 1000 N after 600 s. However, the acoustic emission signal increased strongly at 372 s (load = 620 N, strain  $\varepsilon = 0.36\%$ ), which agrees quite well with the deviation from linearity in the load-displacement curves indicated in the initial tests without acoustic emission discussed above, and reaches a peak value at 460 s (load = 767 N, strain  $\varepsilon = 0.44\%$  calculated by apparent Young's modulus 76.2 GPa). This implies that cracks already form, grow and even stop growing before the specimen reached the maximal deformation.

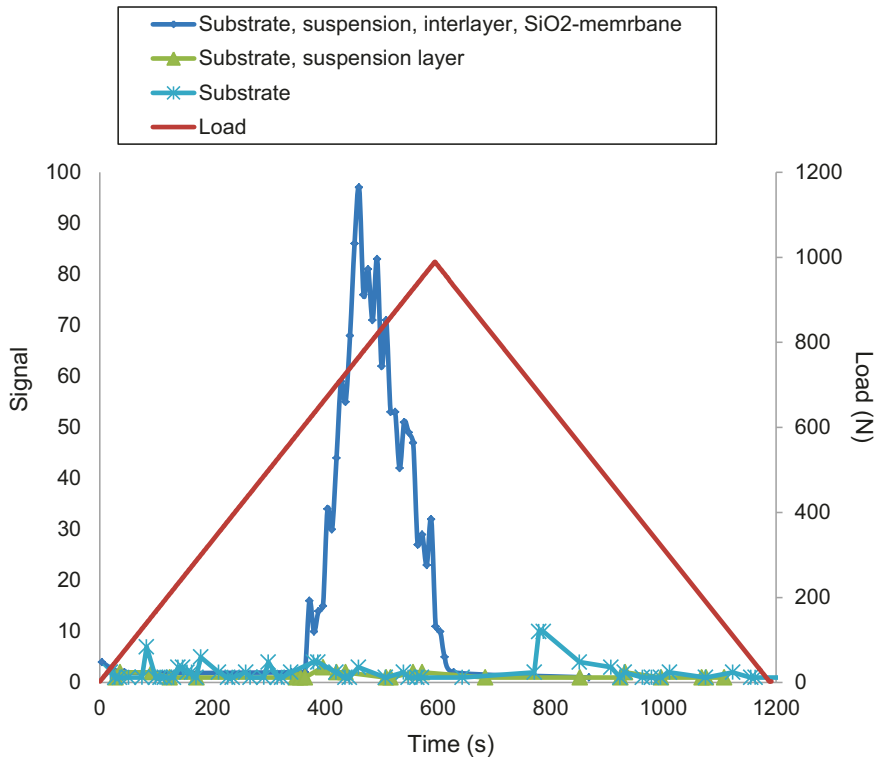


Fig. 60 Deformation and acoustic emission signals of uncoated, partially coated and completely coated specimen as a function of time

In order to characterize the origin of these cracks cross-section of the coated specimen were investigated via SEM after the bending tests. The specimens were cut into four pieces (Fig. 61). The red circle indicates the position of the loading ring within the area the maximum of stress will occur. Therefore, the cross-sections indicated by four red short lines were the focus of the investigation.

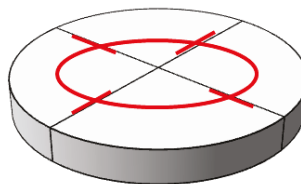


Fig. 61 Schematic cutting way of specimen after deformation testing.

The cross-sections consisting of substrate and suspension layers are shown in Fig. 62, confirming that there are no obvious cracks in the suspension layer, i.e. the porous suspension layer appears to be rather strain tolerant.

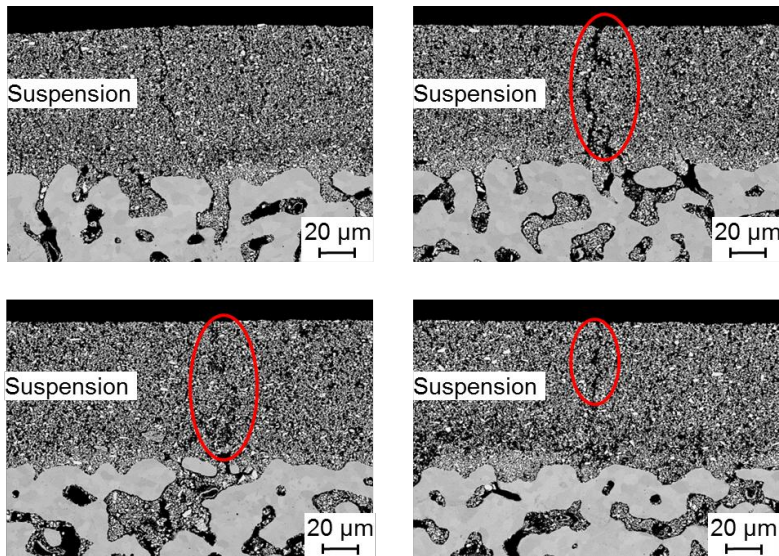


Fig. 62 Cross-section SEM images of specimen consisting of metal substrate and suspension layer

The cross-sections of completely coated substrate with suspension layers and interlayer and function membrane are shown in Fig. 63. It can be confirmed that there are no obvious cracks in the first suspension layer, whereas clear cracks can be seen in the second suspension layer from 8YSZ, interlayer from  $\gamma$ - $\text{Al}_2\text{O}_3$ . The experimentally observed failure strains for the initiation and maximum emission are 0.36 % and 0.44 %, respectively, where former value can be interpreted as the application limit of the structure. In fact, the images show cracks for the 8YSZ layer even in cases where the other layers did not fail, furthermore, delamination cracks in the alumina layer were observed that might be related to crack deflection.

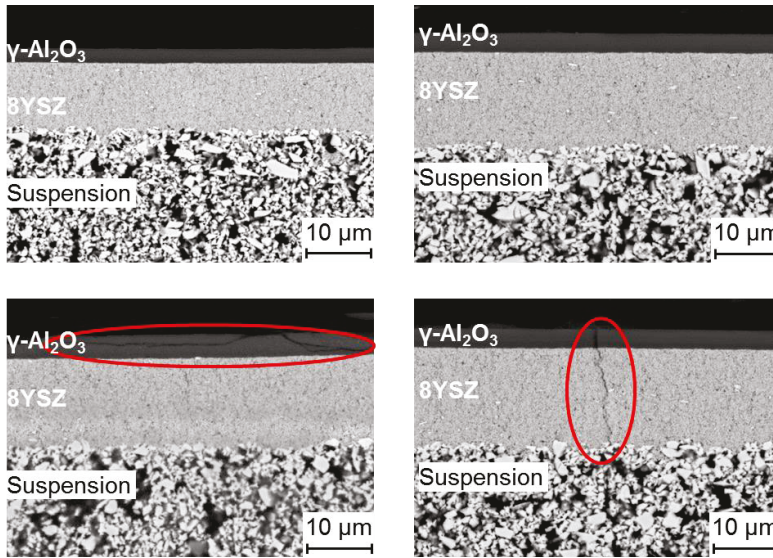


Fig. 63 Cross-section SEM images of completely coated specimen with metal substrate, suspension layer, interlayer and silica membrane.

### 6.2.2.3 Discussion

For the uncoated substrate and substrate coated with suspension layer, there are no obvious cracks in the specimen and additionally no significant signals in the acoustic emission tests. Therefore, the peaks can only correspond to the crack formation and growth in the (YSZ, the  $\gamma\text{-Al}_2\text{O}_3$  interlayer and functional membrane of  $\text{SiO}_2$ ). Consequently, with help of the acoustic emission tests, it can be determined that the cracks form and grow begin at a load of 620 N for a deformation of approximately  $293\ \mu\text{m}$ , which corresponds to a critical strain of 0.36 %.

Via comparison with Table 20 it is obvious that the critical strain for layered composites with metallic substrate is significantly higher than even in the case of the rather robust IEK-1 ceramic substrate, hence, showing the clear advantage of metallic substrate based concepts in terms of materials reliability. However, the disadvantage for long term use might still be the corrosion resistance.

Since the ceramic membrane hinders the deformation of metallic substrate due to higher Young's modulus, the coated specimen has accordingly higher stiffness and is hard to be deformed.

For the ceramic coating system has higher crack forming and growing possibility under tensile stress than under compressive stress, the bending test in the loading configuration "coating system on the tensile side" can be seen as the extreme case. Thus, another completely specimen pre-deformed by such a bending test and with similar deformation

behaviour (Table 22 right) was analysed in the following permeation test, in order to determine the influence of a pre-deformation and the micro-cracks in the coating system on the permeability.

Table 22 Load and deformation of completely coated specimens during bending test (coating system on tensile side)

	Analysed by acoustic emission test and SEM	For following permeation test
Maximal load (N)	989	997
Maximal deformation ( $\mu\text{m}$ )	467	476
Residual deformation after unloaded ( $\mu\text{m}$ )	59	60
Young's modulus (GPa)	76.2	75.4
Maximal strain (%)	0.58	0.59

### 6.3 Permeability

In the following sections, the permeability of different membranes measured in single gas tests and mixed gas tests will be presented, in order to explain the gas transport and separation mechanism of various gases through the membranes.

#### 6.3.1 SiO<sub>2</sub>-membrane on ceramic Atech substrate

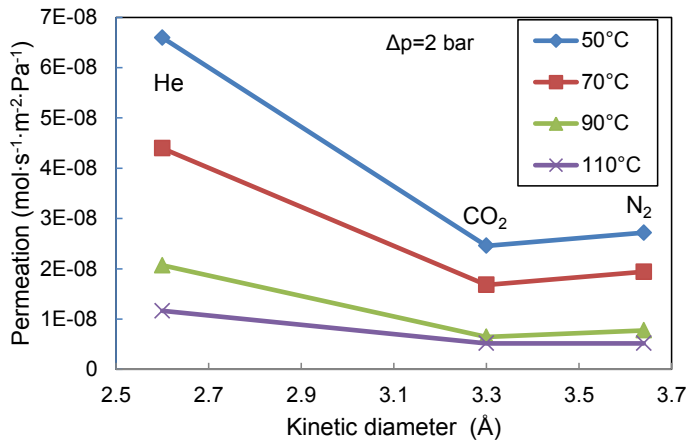


Fig. 64 Permeation of He, CO<sub>2</sub> und N<sub>2</sub> as single gas through the membrane on an Atech substrate at various temperatures as function of kinetic diameter of gas molecules.

The results of permeation tests of the specimen with SiO<sub>2</sub>-membrane on ceramic Atech substrate at different temperatures are plotted in Fig. 64, sorted according to the various kinetic diameters. From Fig. 64 it can clearly be recognized that the permeation rate decreases with the increasing temperature, which agrees with a Knudsen transport mechanism [38]. Furthermore, the selectivity is inversely proportional of the square root of the mass of the gas molecules. The selectivity of CO<sub>2</sub> and N<sub>2</sub> at various temperatures of are also given in Table 23.

Table 23 Selectivities of CO<sub>2</sub>/N<sub>2</sub> at different temperatures (selectivity of ideal Knudsen gas transport is 0.8).

Temperature (°C)	25	50	70	90	Average
Selectivity ( $\alpha$ )	0.83	0.86	0.87	0.83	0.85 ± 0.18

The selectivities measured by single gas permeation tests at 50 °C, 70 °C, 90 °C are 0.86, 0.87 and 0.83 respectively with an average value of 0.85, in a good agreement with the selectivity of an ideal Knudsen diffusion of 0.80, which is calculated by following equation [44]:

$$\alpha_{CO_2/N_2(ideal)} = \sqrt{\frac{M_{N_2}}{M_{CO_2}}} = 0.80 \quad (\text{Equ. 14})$$

However, the change of the permeation rate with temperature cannot be explained by the definition of Knudsen diffusion. According to the definition of Knudsen diffusion, the gas flow is inversely proportional to the square root of the temperature [153-155]. But in our case, where the temperature is only varied slightly (i.e. the ratio of these temperatures is approximately 1.0), the permeation rate changes strongly (Table 24).

Table 24 Permeation of He, CO<sub>2</sub> und N<sub>2</sub> as single gas through silica membrane on Atech substrate ( $\Delta p=2$  bar).

Permeation (mol*s <sup>-1</sup> *m <sup>-2</sup> *Pa <sup>-1</sup> )	50 °C	70 °C	90 °C
He	1.35E-06	9.02E-07	4.25E-07
CO <sub>2</sub>	5.04E-07	3.45E-07	1.33E-07
N <sub>2</sub>	5.57E-07	3.98E-07	1.59E-07

This indicates an additional surface diffusion contributing. In the overview of Uhlhorn about gas-membrane combinations, it is concluded that in all treatments in the literature the surface diffusion is taken as an additional contribution to the gas flow, especially for gas transport through micro-porous or dense materials, where adsorption of molecules is required before the subsequent diffusion process [153]. For example, the flux of hydrogen by surface diffusion through  $\gamma$ -alumina modified with 17 wt% Ag is 2.5 times the Knudsen flux at 25 °C and  $P = 60$  kPa [156]. Meanwhile, the surface diffusion dominates only at low temperatures and also decreases with increasing temperature [38]. Thus, the overlapping of surface diffusion and Knudsen diffusion enhanced the decline of the permeation with increasing temperature.

### 6.3.2 SiO<sub>2</sub>-membrane with ceramic IEK-1 substrate

#### 6.3.2.1 Single-gas permeation tests

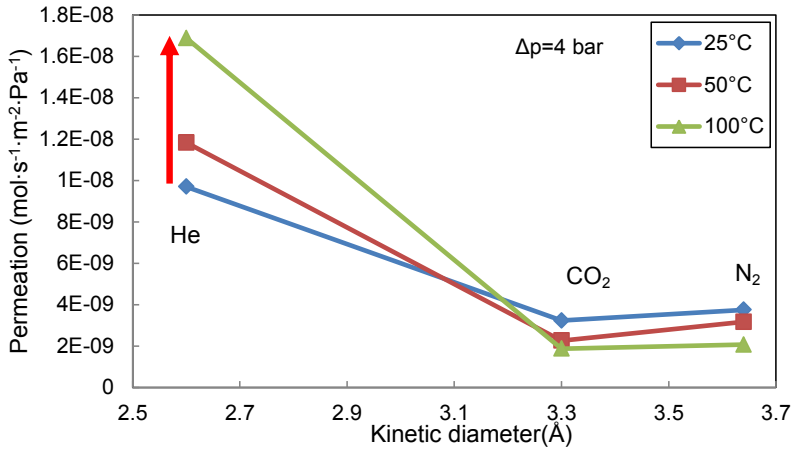


Fig. 65 Permeation of He, CO<sub>2</sub> and N<sub>2</sub> as single gas through a silica membrane on IEK-1 substrate at various temperatures as function of kinetic diameter of gas molecules.

Fig. 65 shows the permeation rates of He, CO<sub>2</sub> and N<sub>2</sub> through the specimen with IEK-1 substrate at various temperatures as function of kinetic diameter of gas molecular. The permeation rates are almost one decade lower than the results measured for the specimens with Atech substrates. Similar as in the case of the specimen with Atech substrate, the permeation rates of CO<sub>2</sub> and N<sub>2</sub> decrease with increasing temperature (Table 25).

Furthermore, the selectivity of CO<sub>2</sub>/N<sub>2</sub> at various temperatures is still about 0.80, as to be expected for Knudsen diffusion (Table 26).

Table 25 Permeation of He, CO<sub>2</sub> and N<sub>2</sub> as single gas through the silica membrane on IEK-1 substrate.

Temperature (°C)	Permeation (mol·s <sup>-1</sup> ·m <sup>-2</sup> ·Pa <sup>-1</sup> )		
	He	CO <sub>2</sub>	N <sub>2</sub>
25	1.99E-07	6.63E-08	7.70E-08
50	2.43E-07	4.64E-08	6.50E-08
100	3.46E-07	3.85E-08	4.25E-08

Table 26 Selectivity of silica membrane on IEK-1 substrate for gas separation He/CO<sub>2</sub>, He/N<sub>2</sub> and CO<sub>2</sub>/N<sub>2</sub>.

Temperature (°C)	Selectivity		
	He/CO <sub>2</sub>	He/N <sub>2</sub>	CO <sub>2</sub> /N <sub>2</sub>
25	3	2.59	0.86
50	5.23	3.73	0.71
100	9	8.16	0.91
	$\alpha_{He/CO_2(ideal)}$ $= \sqrt{\frac{M_{N_2}}{M_{CO_2}}} = 3.32$	$\alpha_{He/N_2(ideal)}$ $= \sqrt{\frac{M_{N_2}}{M_{CO_2}}} = 2.65$	$\alpha_{CO_2/N_2(ideal)}$ $= \sqrt{\frac{M_{N_2}}{M_{CO_2}}} = 0.80$

As shown in Table 26, at room temperature the selectivities of He/CO<sub>2</sub> and He/N<sub>2</sub> are in good agreement with the theoretical selectivity of Knudsen diffusion. However, in contrast to the case of specimens with Atech substrates, the permeation of Helium rises remarkably at increased temperatures. Although it can be expected that the gas permeation by Knudsen diffusion decreases with increasing temperature, this result implies that the permeation of Helium through the specimen with IEK-1 substrate does not follow a Knudsen diffusion mechanism, suggesting a gas molecular sieving effect [157].

Li et al. [158] reported similar results with respect to the sieving effect comparing gas molecules with small e.g. H<sub>2</sub>, and large diameters e.g. CO<sub>2</sub>, N<sub>2</sub>, CH<sub>4</sub> in the case of micro-porous membranes. In Li's study, H<sub>2</sub> revealed much higher permeation rates than the other gaseous component in single gas tests (Table 27). This can be related to the pore size of the micro-porous membrane of 0.30 nm (in the pore size range of silica membrane in this work), which is between the kinetic diameter of H<sub>2</sub> (0.29 nm) and the kinetic diameter of the other gas molecules (CO<sub>2</sub> 0.33 nm, N<sub>2</sub> 0.36 nm).

Table 27 Permeances of H<sub>2</sub>, CO<sub>2</sub>, N<sub>2</sub>, in the single gas tests at 220 °C [158].

Single gas	Permeance ( $\times 10^{-8}$ mol m <sup>-2</sup> s <sup>-1</sup> Pa <sup>-1</sup> )	H <sub>2</sub> selectivity	Kinetic diameter (nm)
H <sub>2</sub>	4.55	-	0.29
CO <sub>2</sub>	0.35	13.0	0.33
N <sub>2</sub>	0.22	20.7	0.36

Furthermore, the a permeance-temperature effect for small gas molecular following a sieving effect has also be found in the literature [159], where Nair et al. found that the helium

permeation values rises with increasing temperature and are less affected by pressure changes, which was also observed in the current work (Fig. 66).

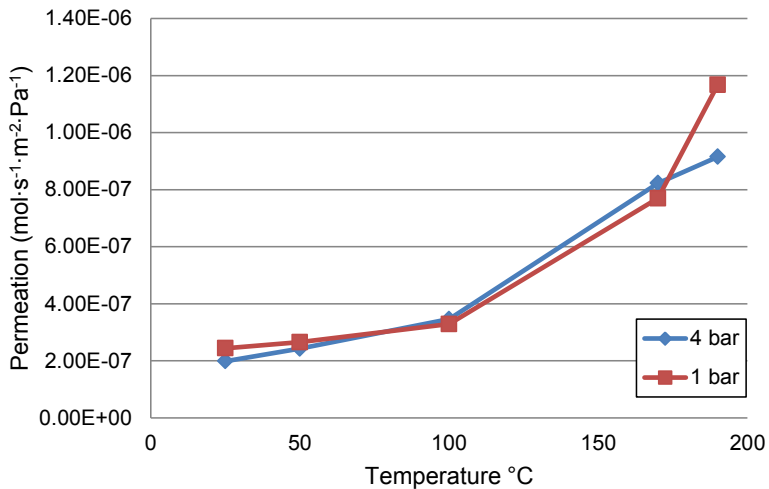


Fig. 66 Helium permeation as single gas through silica membrane on a -1 substrate for feed partial pressures of 4 bar and 1 bar at various temperatures.

In summary, the gas transport of helium through the specimen with IEK-1 substrate can be attributed to molecular sieving effect. Meanwhile, the permeation mechanism of CO<sub>2</sub> and N<sub>2</sub> follows Knudsen diffusion. The difference compared to the Atech material can be explained through the different microstructure of the both substrates. Fig. 67 illustrates the influence of the substrate microstructure on the morphology of coating system. Because of the coarse microstructure, the coating system can only be deposited unevenly on the surface of the Atech substrate, which results in micro-defects in the coated layers and in turn decreases the selectivity for various gas components in spite of the higher permeation compared to the specimen with IEK-1 substrate.

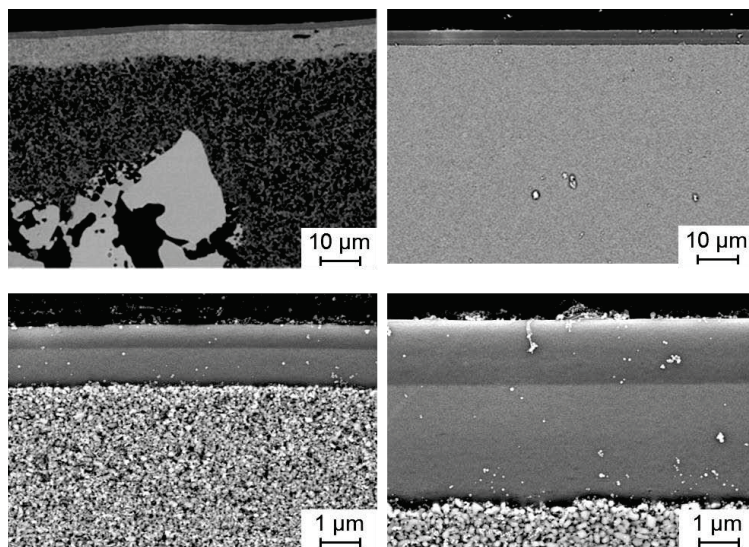


Fig. 67 Cross-sectional SEM images of the coated side (left: coated Atech substrate, right: coated IEK-1 substrate).

The significantly different microstructure of substrate is also reflected in the results of single gas permeation tests with uncoated Atech and IEK-1 substrate. In such tests, the Atech substrate shows no resistance against the feed gas flow, in other word, the feed gas can entirely go through the porous substrate. However, for the IEK-1 material the permeances of helium, CO<sub>2</sub> and N<sub>2</sub> show a good agreement with Knudsen diffusion (Table 28), since the pore size is comparable to the mean free path of the gas molecules.

Table 28 Permeation rates of helium, CO<sub>2</sub> and N<sub>2</sub> and selectivities of He/CO<sub>2</sub>, He/N<sub>2</sub> and CO<sub>2</sub>/N<sub>2</sub> through uncoated IEK-1 substrate at T = 25 °C and Δp = 1 bar.

T=25 °C Δp=1 bar	Permeation (mol*s <sup>-1</sup> *m <sup>-2</sup> *Pa <sup>-1</sup> )			Selectivity		
	He	CO <sub>2</sub>	N <sub>2</sub>	He/CO <sub>2</sub>	He/N <sub>2</sub>	CO <sub>2</sub> /N <sub>2</sub>
	1.83E-05	5.57E-06	7.80E-06	3.2762	2.3401	0.7143
			$\alpha_{He/CO_2(ideal)}$	$\alpha_{He/N_2(ideal)}$	$\alpha_{CO_2/N_2(ideal)}$	
			$= \frac{\sqrt{M_{N_2}}}{\sqrt{M_{CO_2}}}$	$= \frac{\sqrt{M_{N_2}}}{\sqrt{M_{CO_2}}}$	$= \frac{\sqrt{M_{N_2}}}{\sqrt{M_{CO_2}}}$	
			= 3.32	= 2.65	= 0.80	

### 6.3.2.2 Mixed gas tests

The mixed gas tests were performed in order to investigate the influence of the interaction of various gas components on the selectivity in comparison to the single gas tests. Furthermore, the other aim of mixed gas tests is to simulate a real flue gas mixture in fossil power plants. The concentration of CO<sub>2</sub> and N<sub>2</sub> in the feed gas for mixed gas tests was 15 % and 85 %, respectively.

For the specimen with IEK-1 substrate had an expected performance of molecular sieving effect to separate small and large gas molecules, which is also possible for the gas separation of CO<sub>2</sub> and N<sub>2</sub>, such specimen with IEK-1 substrate were selected to be investigated in the following binary gas mixture permeation tests. The permeation results of CO<sub>2</sub> and N<sub>2</sub> through the SiO<sub>2</sub>-membrane with IEK-1 substrate at different temperatures and under different pressures are shown in Fig. 68.

Both permeances of CO<sub>2</sub> and N<sub>2</sub> rise with the increasing temperature, and additionally, are little affected by the change of feed gas pressure. The results show a good agreement with the characteristics of molecular sieving effect since the selectivity of CO<sub>2</sub>/N<sub>2</sub> ratio is higher than 1, i.e. the kinetic diameter of CO<sub>2</sub> molecule is larger than that of N<sub>2</sub> molecule. Furthermore, the increase of CO<sub>2</sub> permeation with the temperature is remarkably larger than that in the case of N<sub>2</sub>.

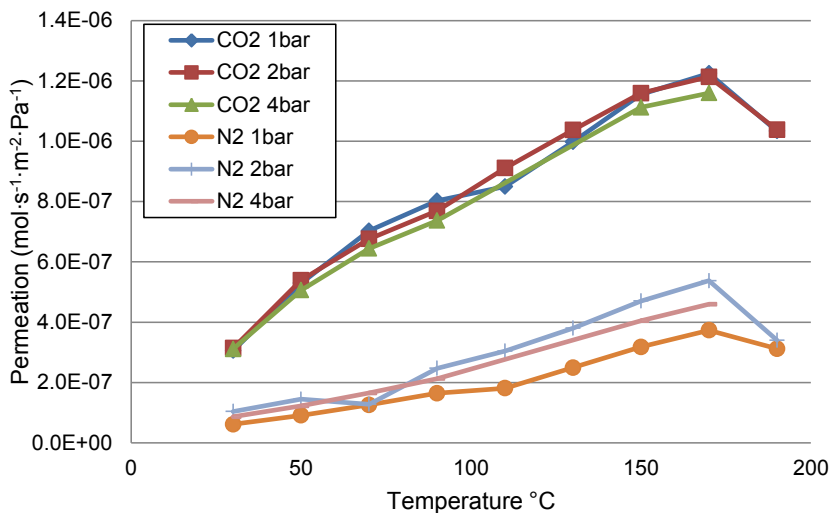


Fig. 68 Permeation of CO<sub>2</sub> and N<sub>2</sub> through the silica membrane on a IEK-1 substrate at various temperatures and under various feed pressures.

The trend of  $\text{CO}_2/\text{N}_2$  selectivity with temperature under various feed pressures is shown in Fig. 69, indicating a decrease with increasing temperature and in particular at room temperature it decreases strongly with increasing pressure. However, the pressure effect becomes less significant when the temperature is increased to 170 °C.

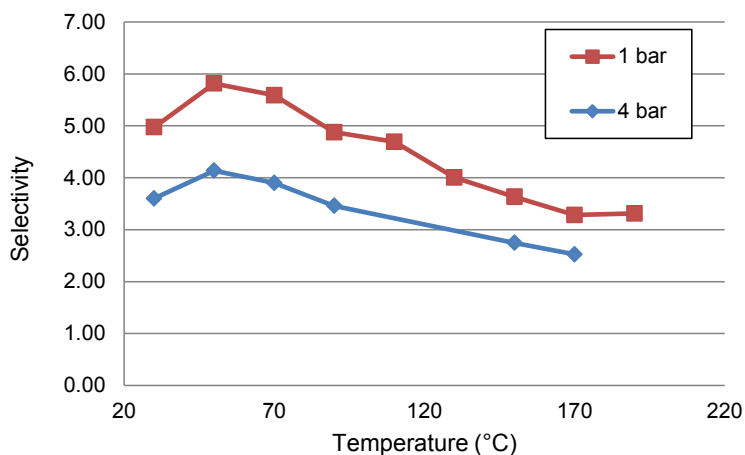


Fig. 69 Selectivity of  $\text{CO}_2/\text{N}_2$  under various differential pressures as the function of temperature.

### ***Discussion***

As shown in the dissertation of Jan Hoffmann [160], the pore size of the silica membranes that were also used in the current work is less than 1 nm, on both Atech and IEK-1 substrate. So in the range of micro-pores, hence, the difference in affinity of gas molecules towards the pore wall play an important role [60] since molecular masses and sizes of are not largely different.

In a literature study on the transport properties of butane through silicalite [161, 162], molecular dynamics simulations were carried out. Furukawa et al. found that the permeability of *n*-butane at 400 K is larger than that at 300 K, since the surface diffusion of the gas components becomes weaker at higher temperature, similar to observations in the current study. This results from the increase in the mobility as the temperature rises, which is larger than the decrease in the adsorption potential [161].

The affinities of  $\text{CO}_2$  and  $\text{N}_2$  in micro-pores have been compared in the literature [163]. In a study by Mizukami et al., the principle of permeation of gas mixture ( $\text{CO}_2/\text{N}_2 = 1:1$ ) in the zeolite membrane is explained via a molecular dynamics simulation. The study revealed that the number of adsorbed  $\text{CO}_2$  molecules is almost twice that of  $\text{N}_2$  molecules in agreement

with experimental data in the literature [164]. Since the pore size characteristic of zeolite is similar to that of silica membrane investigated in the current work ( $d_p > d_{N_2} + d_{CO_2}$ ) [60], it can be concluded that the affinity of  $CO_2$  on the silica surface is also higher than that of  $N_2$ .

In summary, the gas mixture of  $CO_2$  and  $N_2$  shows a higher selectivity of  $CO_2/N_2$  through the  $SiO_2$ -membrane, first, because of the higher affinity of  $CO_2$  on the silica micro pore surface. Hence, the affinity difference results in a high concentration  $CO_2$  concentration and lower  $N_2$  concentration on the pore wall. Furthermore, due to the micro pore size ( $d_p > d_{N_2} + d_{CO_2}$ ), the  $CO_2$  molecules, which migrate along the pore wall, outrun  $N_2$  molecules, which are located in the core region of the pore, since surface diffusion dominates (Fig. 70).

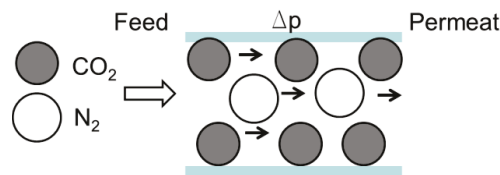


Fig. 70 Schematic principle of the  $CO_2$  and  $N_2$  migration in the porous silica membrane.

Thus, the  $CO_2/N_2$  selectivity measured with feed gas in form of mixture is higher than that of pure gas. Furthermore,  $CO_2$  is adsorptive and smaller than  $N_2$ , and the  $N_2$  molecules are inhibited to pass by  $CO_2$  in the micro-pore. Hence, carbon dioxide permeates better than nitrogen. Furthermore, the surface diffusion dominates the  $CO_2/N_2$  selection, thus, the selectivity at high temperature, where gas phase transport becomes stronger, is lower than that at room temperature. Due to the limitation of the pore room, the impact of transition from surface diffusion on gas phase transport is not very pronounced, and the selectivity declines only slightly. Moreover, because most  $CO_2$  molecules are on the pore wall due to the good affinity with  $SiO_2$ , the pressure change cannot affect the permeation of  $CO_2$  significantly. But since  $N_2$  diffuses mainly in the gas phase, the permeation increases as the pressure rises, which reduces the selectivity of  $CO_2/N_2$ .

### 6.3.2.3 Mixed gas tests with water vapour

With the aid of water spraying and a heating set-up, the water vapour (0.1 g/min) was added to the gas mixture. The permeances of  $CO_2$  and  $N_2$  through  $SiO_2$ -Membran with IEK-1 substrate under the atmosphere with water vapour are shown in the following figure. In addition, the results with water vapour, the results without water vapour are also plotted in the figure for comparison.

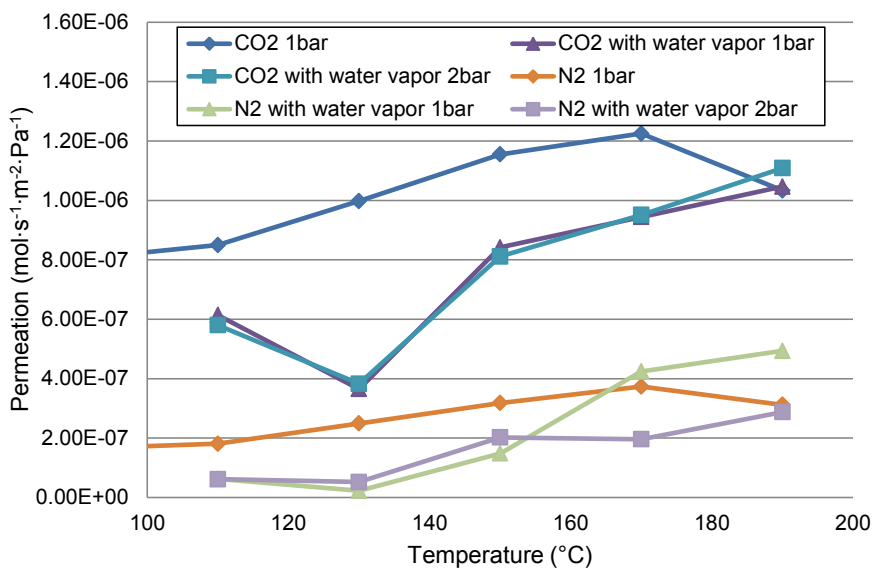


Fig. 71 Permeation of CO<sub>2</sub> and N<sub>2</sub> with and without water vapour through specimen with a IEK-1 substrate at different temperatures and under various pressures.

After adding water vapour to the feed gas comparing of 85 % N<sub>2</sub> and 15 % CO<sub>2</sub>, the permeances of CO<sub>2</sub> and N<sub>2</sub> decrease a little compared to that without water vapour. Furthermore, the dependence of permeation on the temperature is a bit stronger than in the case without water vapour (Table 29). The permeance of CO<sub>2</sub> with water vapour reaches the same value obtained without water vapour at 190 °C. The permeance of N<sub>2</sub> with water vapour has already exceeded the value without water vapour at 170 °C.

Table 29 Permeation trend with increasing temperature (mol·s<sup>-1</sup>·m<sup>-2</sup>·Pa<sup>-1</sup>/K·10<sup>-9</sup>).

CO <sub>2</sub> 1bar	5
CO <sub>2</sub> with water vapour 1 bar	7
CO <sub>2</sub> with water vapour 2 bar	8
N <sub>2</sub> 1 bar	2
N <sub>2</sub> with water vapour 1 bar	6
N <sub>2</sub> with water vapour 2 bar	3

The selectivity of CO<sub>2</sub>/N<sub>2</sub> with water vapour as the function of temperature is shown in Fig. 72. At 110 °C the selectivity under differential pressure  $\Delta p = 1$  bar and  $\Delta p = 2$  bar cannot be distinguished. As the temperature increases, the selectivity of CO<sub>2</sub>/N<sub>2</sub> with water vapour for a differential pressure ( $\Delta p$ ) of 1 bar reaches a maximum and then decreases dramatically. This

should result from the decline of CO<sub>2</sub> at this point due to feed gas fluctuation. At 170 °C and 190 °C the selectivity with  $\Delta p = 1$  bar is even lower than that of  $\Delta p = 2$  bar.

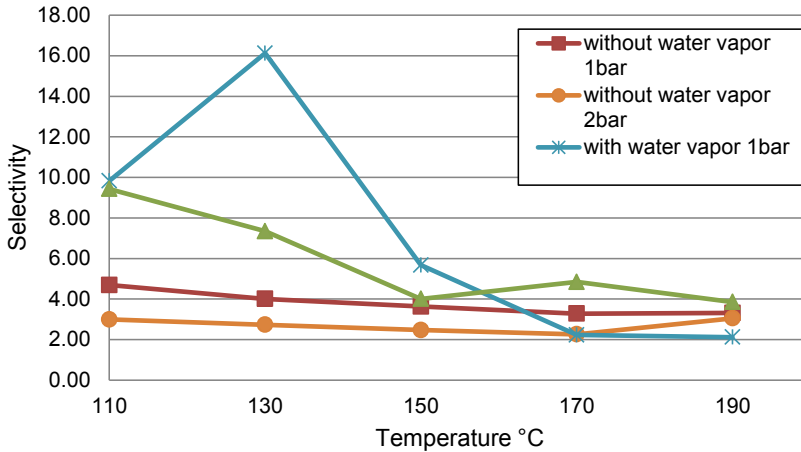
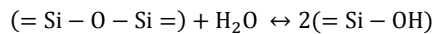


Fig. 72 Selectivity of CO<sub>2</sub>/N<sub>2</sub> under various differential pressures as the function of temperature.

### Discussion

The sensitivity of micro-porous SiO<sub>2</sub> membrane to water vapour has been discussed in a study of Wei et al. [165]. Through infrared spectrometry and thermo-gravimetric analysis, it was interpreted that the micro-porous SiO<sub>2</sub> membrane is hydrophilic and can absorb humidity in the environment through chemisorption called rehydration [92]:



This reaction and the interaction between (-O-H) group on the SiO<sub>2</sub>-membrane surface and water vapour causes further condensation of the SiO<sub>2</sub>-membrane. Hence, the original micro pores (< 1 nm) shrink and are even blocked up [165]. The shrinkage of the pores results obviously in a decrease of the CO<sub>2</sub> and N<sub>2</sub> permeation.

Furthermore, the large numbers of (-O-H) groups are the sites for absorption of CO<sub>2</sub>. Hence, the affinity of CO<sub>2</sub> on the micro-porous SiO<sub>2</sub> surface is enhanced significantly with the aid H<sub>2</sub>O. Therefore, more CO<sub>2</sub> can migrate through the membrane via surface diffusion, which means that the transition of gas transport for CO<sub>2</sub> molecules from surface diffusion to gas phase that is expected with increasing temperature is balanced to some extent by the higher adsorption of CO<sub>2</sub> on the pore wall and as the mobility of CO<sub>2</sub> molecules on the silica micro-

pore wall increases, the permeation in the case with water vapour recovers to the value without water vapour at 190 °C.

It is necessary to take the condensation behaviour into consideration for feed gas pressures that are higher than atmosphere pressure. At 100 °C the condensation pressure of water vapour is about 1.01 bar. In this testing campaign the applied differential pressures were 1 bar and 2 bar, which accordingly means that the feed gas pressures were 2 bar and 3 bar respectively. From the calculated partial pressure of water vapour in the gas mixture, it can be concluded that the water vapour was not condensed on the micro pore walls at all testing temperatures for all the partial pressures of water vapour were lower than the condensation pressures (Table 30).

Table 30 Partial pressure of water vapour in gas mixture (condensation pressure of water vapour 1.01 bar at 100 °C)

Temperature (°C)	Partial pressure of water vapour (bar)	
	$\Delta p = 1\text{bar}$	$\Delta p = 2\text{bar}$
110	0.48	0.73
130	0.50	0.76
150	0.52	0.78
170	0.54	0.81
190	0.56	0.84

Condensation during the measurements will not strongly affect the conclusions drawn for the case without the water vapour condensation, because it has already been determined that the gas transport through micro-porous silica membrane is dominated by surface diffusion. Additionally, the (Si-O-H) and (Si-O) group on silica membrane surface that typically reacts with CO<sub>2</sub> has already reacted chemically with H<sub>2</sub>O or moistened physically by H<sub>2</sub>O condensation. Therefore, the affinity of CO<sub>2</sub> with the silica pore wall is totally affected by (-O-H) groups and is the same as the affinity in the case of water condensation on the silica pore wall.

Also due to high affinity of CO<sub>2</sub> towards surface diffusion, the permeances of CO<sub>2</sub> with water vapour under differential pressure of 1 bar and 2 bar, which has mainly an impact on the gas phase transport, cannot be distinguished from each other.

As shown in Fig. 70 and discussed in section 6.3.2.2, the adsorption of CO<sub>2</sub> on the micro porous silica membrane can restrain the diffusion of N<sub>2</sub>, because the available diffusion path

of  $N_2$  in the micro-pores is limited by the  $CO_2$  on the pore wall. Since the water vapour can also shrink the pore size and meanwhile the affinity of  $CO_2$  on the pore wall can remain active, the path for  $N_2$  through the membrane will be much smaller than in the case without water vapour. Furthermore, in the study of Choi [166], it was verified that the adsorption of  $CO_2$  on the pore wall can increase with increasing the gas pressure. Thus, the capillary condensation of  $CO_2$  molecules could occur aided by  $H_2O$  or (-Si-O-H) group to some degree. This could be the reason that in the case of tests with water vapour the permeation of  $N_2$  under differential pressure of 1 bar is even higher than that under 2 bar.

### **6.3.3 Amino-modified $SiO_2$ -membrane on ceramic IEK-1 substrate**

#### **6.3.3.1 Single-gas permeation tests**

The single gas permeation tests were preceded by my project partner Dr. J. Eiberger (IEK-1). The results of single gas tests for  $CO_2$  and  $N_2$  are plotted in Fig. 73. The permeation of  $CO_2$  decreases with increasing temperature, but the permeation of  $N_2$  rises with increasing temperature.

The data imply that the gas transport for  $N_2$  is dominated by Knudsen diffusion, as the case of previous  $N_2$  single gas tests for non-amino-modified membranes. However, the  $CO_2$  permeation change with temperature has a good agreement with the one expected for a molecular sieving effect. Furthermore, as discussed in the previous section, since surface diffusion is limited by increasing temperature to some extent, the enhancement of the affinity of  $CO_2$  on micro pore wall and higher movement with increasing temperature can compensate the decline of the permeation. Hence, the gas transport of  $CO_2$  should be dominated by surface diffusion and molecular sieving. Since the gas transport mechanisms for  $CO_2$  and  $N_2$  are independent, the gas transport by Knudsen diffusion could be higher than the gas transport by surface diffusion. Therefore, at room temperature the permeation of  $N_2$  could be higher than that of  $CO_2$  in the case of single gas permeation tests. But due to reverse permeation trend with temperature, the permeation of  $CO_2$  becomes larger than that of  $N_2$  when the temperature is above 100 °C.

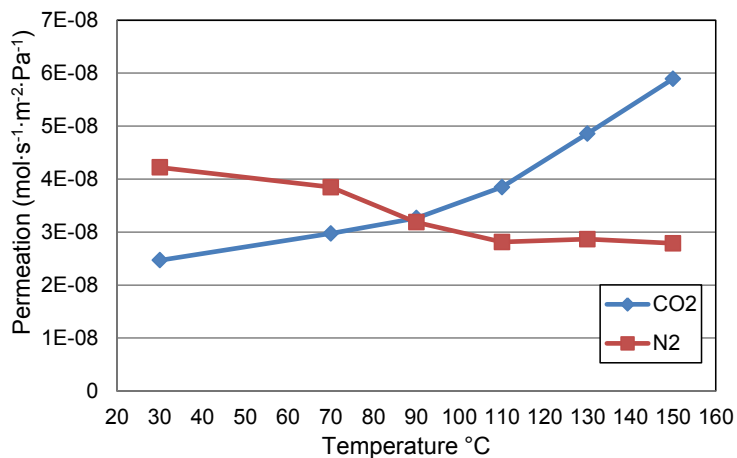


Fig. 73 Permeances of CO<sub>2</sub> und N<sub>2</sub> single gases through amino-modified SiO<sub>2</sub>-membrane as a function of temperature ( $\Delta p = 4$  bar)

### 6.3.3.2 Mixed gas tests

Fig. 74 shows the results of permeation tests with a gas mixture of 85 % N<sub>2</sub> and 15% CO<sub>2</sub> as a function of temperature under pressure differences of 4 bar and 5 bar.

Compared with the results of single gas tests, the permeances of CO<sub>2</sub> and N<sub>2</sub> are lower at every temperature. This decrease is especially evident for the permeation of N<sub>2</sub>. In particular at room temperature the permeation for CO<sub>2</sub> shows no difference between single gas test and binary gas mixture. There is high possibility for occurrence of a molecular sieving effect in the range of micro-pores, where, the separation of the small CO<sub>2</sub> and N<sub>2</sub> gas molecules is mainly based on the interaction between the gas molecules and the pore wall, i.e. difference of adsorption and diffusion rates, and also on the intrinsic interaction between the gas molecules [167].

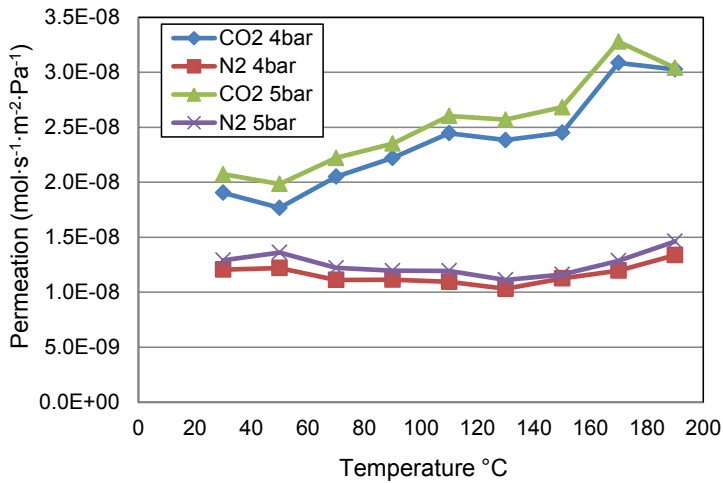


Fig. 74 Permeances of CO<sub>2</sub> und N<sub>2</sub> as gas mixture through amino-modified SiO<sub>2</sub>-membrane as a function of temperature

As discussed with respect to the results of single gas tests, the gas transport of CO<sub>2</sub> should be dominated by surface diffusion and molecular sieving, and the gas transport for N<sub>2</sub> dominated by Knudsen diffusion. Therefore, the permeation of CO<sub>2</sub> in binary gas mixture is similar to single gas due to the same affinity of CO<sub>2</sub> on the amino-modified (-R-NH<sub>2</sub>) micro porous silica surface at room temperature. However, the N<sub>2</sub> diffusion path which is mainly via the gas phase through micro-porous silica membrane is affected by following effects. First, the pore size of micro-silica membrane is reduced by the functional amino groups. Second, the CO<sub>2</sub> molecules, which absorb on the pore walls with the help of functional amino groups, reduce the path for N<sub>2</sub> through the membrane even further (Fig. 75). Thus, the permeation of N<sub>2</sub> decreases significantly.

Moreover, as discussed in a study of Morooka et al. [60], because of this reduced pore size ( $d_p < d_{N_2} + d_{CO_2}$ ), gas molecules cannot pass each other (Fig. 75). Once gas molecules enter the pores in the form of a gas mixture, the total permeation rate through the pores is impacted by coefficient interaction of the gas molecules with different permeation rates. It can be interpreted that the permeation rate of CO<sub>2</sub> by surface diffusion on the amino-modified silica pore walls is higher than that of N<sub>2</sub> by gas phase diffusion. Thus, the CO<sub>2</sub> molecules with higher mobility can accelerate the relatively slower N<sub>2</sub> molecules so that the permeation of N<sub>2</sub> can be almost constant even though the temperature increases to temperatures at which the permeation of N<sub>2</sub> should normally decrease according to the inverse relationship of Knudsen diffusion flux and the temperature. Furthermore, the permeation of CO<sub>2</sub> in the binary gas mixture is lower than in the case of a single gas since the transport is hindered nitrogen gas molecules with slower diffusion rate.

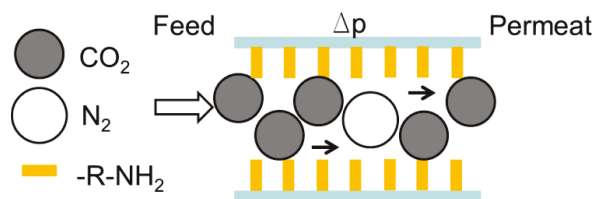


Fig. 75 Schematic principle of the CO<sub>2</sub> and N<sub>2</sub> migration in the amino-modified porous silica membrane

The selectivity of CO<sub>2</sub>/N<sub>2</sub> under various pressure differences as the function of temperature is shown in Fig. 76. It is evident that the selectivity is independent of this differential pressure. As discussed above, in the micro pore range ( $d_p < d_{N_2} + d_{CO_2}$ ), the gas molecules can not pass each other when they are transported along the pores. Hence, CO<sub>2</sub> and N<sub>2</sub> molecules are affected similarly by the pressure difference and thus, there is no influence of pressures on the separation of CO<sub>2</sub> and N<sub>2</sub>.

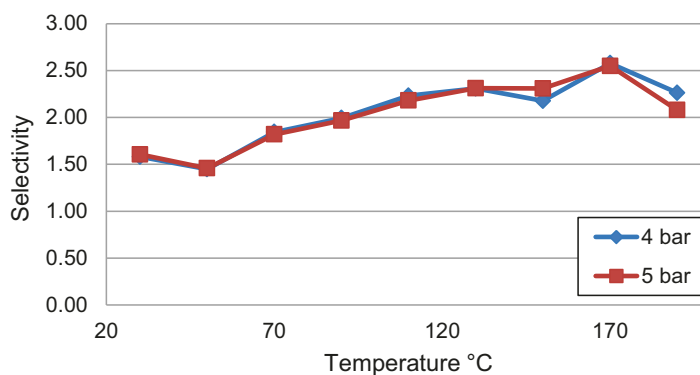


Fig. 76 Selectivity of CO<sub>2</sub>/N<sub>2</sub> under various differential pressures as the function of temperature

### 6.3.3.3 Mixed gas tests with water vapour

The permeances of CO<sub>2</sub> and N<sub>2</sub> as gas mixture with water vapour through amino-modified SiO<sub>2</sub>-membrane are shown in Fig. 77. After the addition of water vapour to the gas mixture (85 % N<sub>2</sub>, 15 % CO<sub>2</sub>), the permeances of CO<sub>2</sub> and N<sub>2</sub> shows an evident decrease in comparison with the results of permeation tests with binary gas mixture without water. The decline of the CO<sub>2</sub> permeation at the temperatures below 160 °C is obviously larger than that observed for N<sub>2</sub>. The decrease of N<sub>2</sub> permeation remains until the temperature reaches 190 °C, whereas the CO<sub>2</sub> permeation recovers to the level of permeation measured without water vapour.

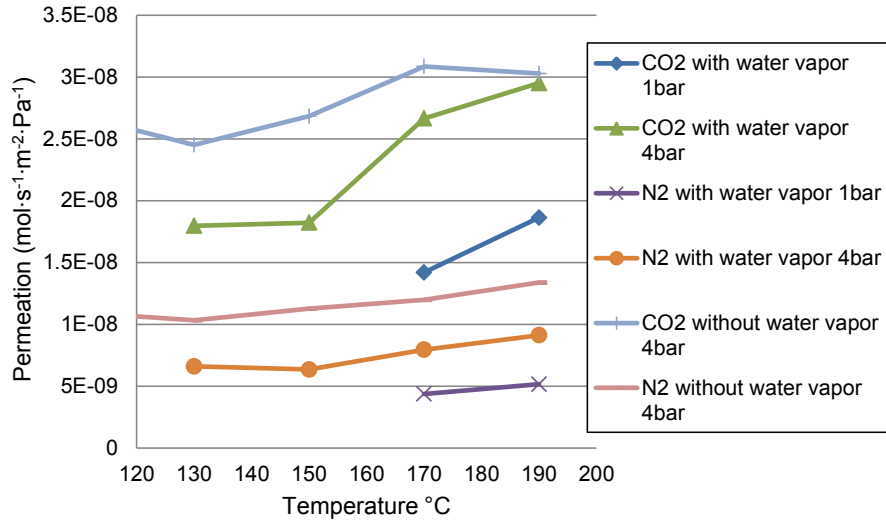


Fig. 77 Permeances of CO<sub>2</sub> and N<sub>2</sub> as gas mixture with water vapour through amino-modified SiO<sub>2</sub>-membrane as a function of temperature

Fig. 78 shows the selectivity of CO<sub>2</sub>/N<sub>2</sub> in permeation tests with binary gas mixture under various differential pressures as the function of temperature. The addition of water to the gas mixture has obviously raised the CO<sub>2</sub> and N<sub>2</sub> separation efficiency. However, because the permeances of the both gas components increase proportionally with the change of differential pressure from 1 bar to 4 bar, as shown in Fig. 77, the selectivity of CO<sub>2</sub>/N<sub>2</sub> is rather stable.

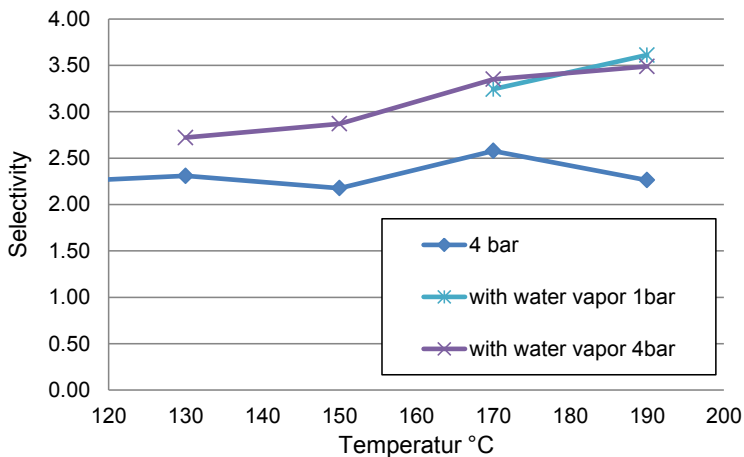


Fig. 78 Selectivity of CO<sub>2</sub>/N<sub>2</sub> in permeation tests with binary gas mixture under various differential pressures as the function of temperature

As discussed in section 6.3.2.3, it is necessary to consider the condensation behaviour of the water vapour. The partial pressures of water vapour at different temperatures are calculated and shown in Table 31. Since the condensation pressure is 2.7 bar at 130 °C [168], the water vapour in the gas mixture did not condensate on the silica micro pore surface.

Table 31 Partial pressure of water vapour in gas mixture (condensation pressure of water vapour is 2.7 bar at 130 °C)

Temperature (°C)	Partial pressure of water vapour (bar)
130	1.26
150	1.30
170	1.35
190	1.39

Due to the higher selectivity of amino-modified SiO<sub>2</sub>-membrane in the permeation tests with water vapour, the concentration of CO<sub>2</sub> in the permeate also increases comparing to the case without water vapour (Fig. 79).

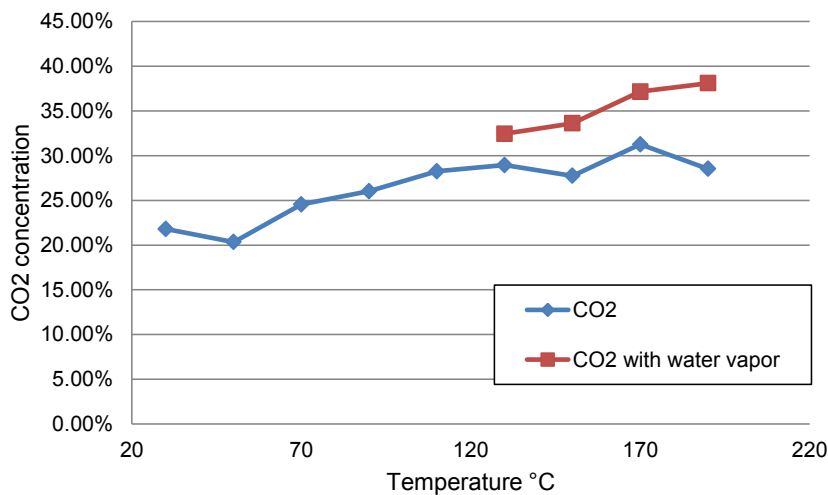


Fig. 79 The concentration of CO<sub>2</sub> in the permeate gas measured by binary gas mixture permeation tests as function of temperature (Feed gas: 85% N<sub>2</sub>, 15 % CO<sub>2</sub>)

Considering that the amount of water vapour could affect the permeation of gases through amino-modified silica membrane, the water injected into the gas mixture was reduced from 0.1 g/min to 0.05 g/min at 170 °C. The permeances of CO<sub>2</sub> and N<sub>2</sub> as a function of differential

pressure for this case are plotted in Fig. 80. It is evident that the permeances of CO<sub>2</sub> and N<sub>2</sub> were not changed in spite of reduction of the amount of water vapour amount.

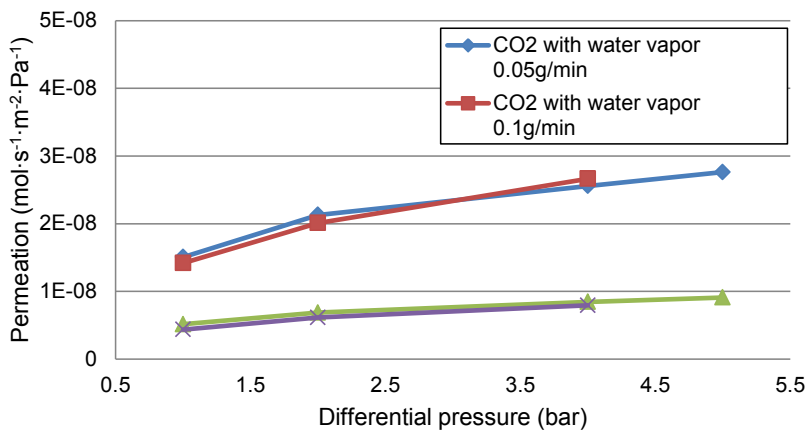


Fig. 80 The influence of water vapour amount on the permeances of CO<sub>2</sub> and N<sub>2</sub> at 170 °C

### Discussion

As shown theoretically in Fig. 9 in section 3.3.4.2, the presence of water can enhance the absorption of carbon dioxide molecules at amino-groups. This is realized via a doubled availability of amino-group. In the absence of water, each carbon dioxide molecule needs two amino groups on the silica surface to be chemisorbed in the form of ammonium carbamate. But if there is water present in the carbon dioxide gas, the carbamate will become an ammonium bicarbonate species. This has been confirmed in the study of Leal et al. [71].

In the studies of Hiyoshi et al. [169], carbon dioxide reveals a higher adsorption capacity on amino modified silica membrane surface with the presence of water than under dry condition. So far there is no literature indicating that the presence of water will reduce the adsorption of carbon dioxide on an amino functionalized silica membrane. Therefore, the decline of CO<sub>2</sub> permeation in presence of water vapour in the gas mixture below 190 °C can only be attributed to the reduction of desorption of carbon dioxide molecules from the pore surface of the amino modified silica membrane.

This conclusion is supported by the study of Knowles et al. [170]. In their work, the results of DTA indicate a rapid uptake of the carbon dioxide adsorption in the presence of water as well as in the absence of water. However, only approximately one-third of the adsorbed CO<sub>2</sub> could be rapidly desorbed. In the following 10 min of the desorption experiment, no further mass loss was observed. In our case, the holding time to obtain a stable measure point was 30 min

and no change of CO<sub>2</sub> permeation observed during the test. The reason why desorption of carbon dioxide is diminished by the presence of water could be the higher active energy for the transition from bicarbonate to carbamate than the inverse transition. Hence, as the temperature increases, the permeation of CO<sub>2</sub> rises rapidly and reaches the permeation value without water vapour.

#### 6.3.4 Permeability of SiO<sub>2</sub>-membrane on porous metal substrates

Fig. 81 shows the permeation results of single gas measurements (He, CO<sub>2</sub>, N<sub>2</sub>) through SiO<sub>2</sub>-membrane on an ITM metallic substrate. Just as in the case of the silica membrane on the IEK-1 ceramic substrate, the permeances of CO<sub>2</sub> and N<sub>2</sub> decrease with increasing temperature and the permeation of helium increases with increasing temperature (Table 32). This means that the gas transport of helium through the silica membrane on the ITM metal substrate is determined by molecular sieving effect, whereas the transport mechanism of CO<sub>2</sub> and N<sub>2</sub> through this type of membrane is still dominated by Knudsen diffusion. Furthermore, the good reproducibility of the results indicates that the silica coating can be deposited on the ceramic as well as on metallic substrate.

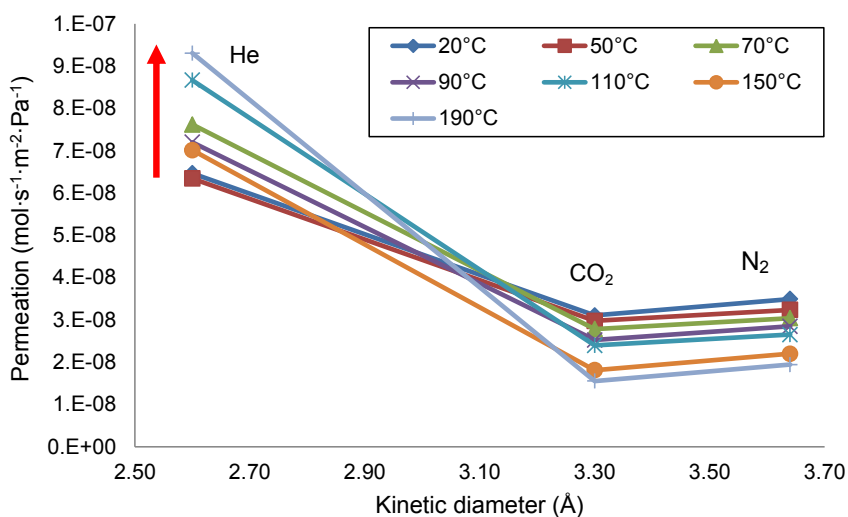


Fig. 81 Permeation of He, CO<sub>2</sub> and N<sub>2</sub> as single gas through the membrane on ITM porous metal substrate at various temperatures as function of kinetic diameter of gas molecules ( $\Delta p = 4$  bar), without pre-deformation

Table 32 Permeation of He, CO<sub>2</sub> and N<sub>2</sub> as single gas through silica membrane on ITM porous metal substrate and the selectivity of silica membrane for gas separation CO<sub>2</sub>/N<sub>2</sub>, without pre-deformation

Temperature (°C)	Permeation (mol·s <sup>-1</sup> ·m <sup>-2</sup> ·Pa <sup>-1</sup> )		Selectivity CO <sub>2</sub> /N <sub>2</sub>
	CO <sub>2</sub>	N <sub>2</sub>	$\alpha_{CO_2/N_2(ideal)}$ $= \sqrt{\frac{M_{N_2}}{M_{CO_2}}} = 0.80$
25	6.37E-07	7.17E-07	0.89
50	6.10E-07	6.63E-07	0.92
70	5.71E-07	6.24E-07	0.91
90	5.18E-07	5.84E-07	0.89
110	4.91E-07	5.44E-07	0.90
150	3.72E-07	4.51E-07	0.82
190	3.18E-07	3.98E-07	0.80

Subsequently, this specimen was deformed by ring-on-ring bending tests, to have a pre-deformation of approximately 476 μm (Load = 997 N, strain = 0.59 %, residual deformation = 60 μm, see Table 22). With this pre-deformation, the permeation of single gases through this specimen was measured again. The results are shown in Fig. 82. The permeances of all the gases are enhanced by more than one decade. Moreover, there is no apparent molecular sieving effect apparently. It indicates that such a pre-deformation has already produced the micro-cracks, which has already proved in section 6.2.2.2. These micro-cracks result in the absence of molecular sieving and the gas transport mechanism turns to Knudsen diffusion.

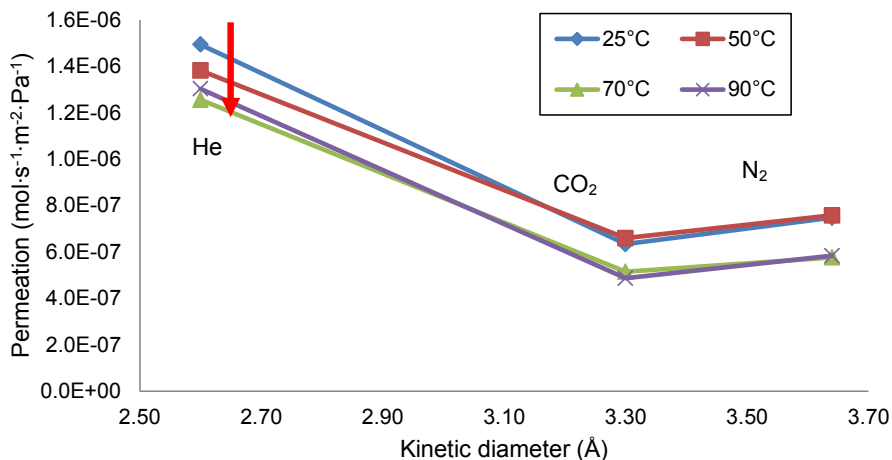


Fig. 82 Permeation of He, CO<sub>2</sub> and N<sub>2</sub> as single gas through the membrane on ITM porous metal substrate at various temperatures as function of kinetic diameter of gas molecules ( $\Delta p = 4$  bar), with pre-deformation of 100  $\mu\text{m}$

Table 33 Permeation of He, CO<sub>2</sub> and N<sub>2</sub> as single gas through silica membrane on ITM porous metal substrate and the selectivity of silica membrane for gas separation CO<sub>2</sub>/N<sub>2</sub>, with pre-deformation

Temperature (°C)	Permeation (mol·s <sup>-1</sup> ·m <sup>-2</sup> ·Pa <sup>-1</sup> )		Selectivity CO <sub>2</sub> /N <sub>2</sub> $\alpha_{CO_2/N_2(ideal)}$ $= \sqrt{\frac{M_{N_2}}{M_{CO_2}}} = 0.80$
	CO <sub>2</sub>	N <sub>2</sub>	
25	1.30E-05	1.53E-05	0.85
50	1.35E-05	1.56E-05	0.87
70	1.33E-05	1.49E-05	0.89
90	1.33E-05	1.59E-05	0.83

### Discussion

By the comparison of the results of permeation tests with a respective specimen before and after deformation, the influence of the micro-cracks formed during deformation process has been assessed. Because of these micro-cracks through SiO<sub>2</sub>-membrane and interlayer until suspension layer, the molecular sieving effect for small gas molecules has been replaced by total Knudsen's diffusion. With the aid of acoustic emission test, the formation of micro-cracks was ascertained at the strain of 0.36 % under the load of 620 N and the deformation of 293  $\mu\text{m}$ , these parameters should be set as the threshold for the reliable application of SiO<sub>2</sub>-membrane on porous ITM substrate.

## 6.4 Thermochemical stability

In order to explain the adsorption state of CO<sub>2</sub> on pure silica membrane and amino-modified silica membrane, ex situ infrared spectrometry study was carried out. The results of infrared spectra for the specimens annealed in ambient dry gas flow (50 ml/min, 85 % N<sub>2</sub>, 15 % CO<sub>2</sub>, 150 °C) and moistened gas flow (50 ml/min dry gas flow with 1g/h water, 300 °C) respectively, are compared in the following sections.

### 6.4.1 SiO<sub>2</sub>-membrane with ceramic Atech substrate and ceramic IEK-1 substrate

The IR-spectra in the region 800-1700 cm<sup>-1</sup> of SiO<sub>2</sub>-membrane with Atech substrate and with IEK-1 substrate annealed with and without water vapour are shown in Fig. 83 and Fig. 84, respectively. The band at 1080 cm<sup>-1</sup> assigns asymmetric Si-O-Si stretching. Furthermore, at 1240 cm<sup>-1</sup> there is another absorption band indicating Si-O-Si which appears only with decreasing thickness of SiO<sub>2</sub>-layer [171, 172]. Thus, the thickness of SiO<sub>2</sub>-layer can also be reflected by representing the IR-spectra of SiO<sub>2</sub>-membrane on Atech substrate and IEK-1 substrate annealed without water vapour. Because the band at 1240 cm<sup>-1</sup> of SiO<sub>2</sub>-membrane on Atech substrate is higher than that of SiO<sub>2</sub>-membrane on IEK-1 substrate, it can be concluded that the thickness of SiO<sub>2</sub>-layer on Atech substrate is smaller than on IEK-1 substrate, what is hardly assessed by SEM. This conclusion can also explain the lower defect possibility of SiO<sub>2</sub>-layer on IEK-1 substrate, which resulted in a molecular sieving effect. Moreover, the larger thickness of SiO<sub>2</sub>-layer on IEK-1 substrate can also hinder the gas flux through the membrane (see sections 6.3.1 and 6.3.2).

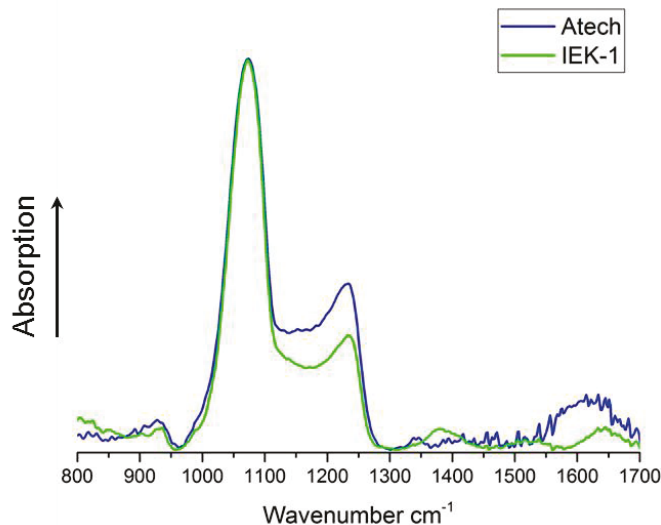


Fig. 83 IR-spectra of SiO<sub>2</sub>-membrane with Atech substrate and with IEK-1 substrate annealed without water vapour

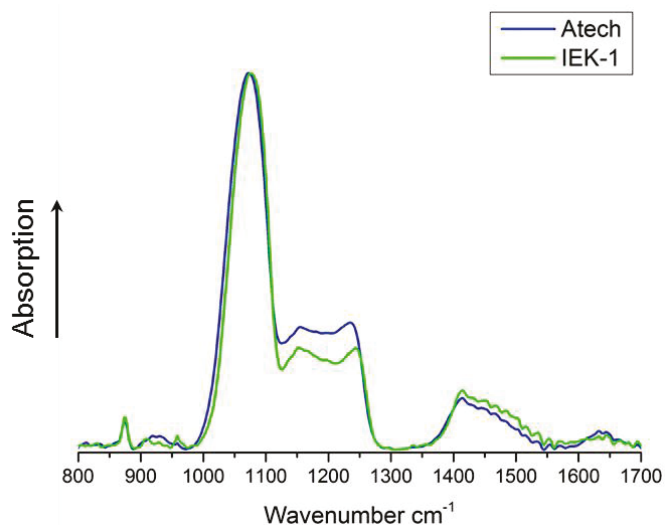


Fig. 84 IR-spectra of SiO<sub>2</sub>-membrane with Atech substrate and with IEK-1 substrate annealed with water vapour

For both SiO<sub>2</sub>-membranes on Atech substrate and IEK-1 substrate, after annealing tests with water vapour, the band at 1240 cm<sup>-1</sup> decreased, suggesting that the amount of Si-O-Si stretching is reduced. Furthermore, there is an obvious increase for bands between 1400 cm<sup>-1</sup> and 1500 cm<sup>-1</sup> indicating an increasing amount of bending O-H bending due to the presence of adsorbed molecular water [71].

The band at about 1630 cm<sup>-1</sup> belongs also to the bending vibration of adsorbed and coordinated water molecules [173]. By the comparison of the intensity of this band at about 1630 cm<sup>-1</sup> for SiO<sub>2</sub>-membrane on Atech substrate and on IEK-1 substrate before annealing with water vapour, it can be concluded that the SiO<sub>2</sub>-membrane on Atech substrate tended to absorb more water molecules. This conclusion could result from the relatively large pores and defects in the SiO<sub>2</sub>-membrane on Atech substrate compared to the IEK-1 substrate.

Furthermore, the wide band between 3200 cm<sup>-1</sup> and 3700 cm<sup>-1</sup> can be seen as three Gaussian contributions: the band at 3250 cm<sup>-1</sup> indicates water absorption; the band at 3450 cm<sup>-1</sup> indicates associated Si-OH; the band at 3640 cm<sup>-1</sup> indicates isolated Si-OH stretching [174-176]. Before annealing with water vapour, the SiO<sub>2</sub>-membrane on Atech substrate absorbed also more water molecules than on IEK-1 substrate, like the band at 1630 cm<sup>-1</sup> (Fig. 85). However, after annealing with water vapour, the amount of absorbed water molecules represented by the intensity of the bands reduced significantly, indicating more water molecules in the SiO<sub>2</sub>-membrane on IEK-1 substrate than that in SiO<sub>2</sub>-membrane on Atech substrate.

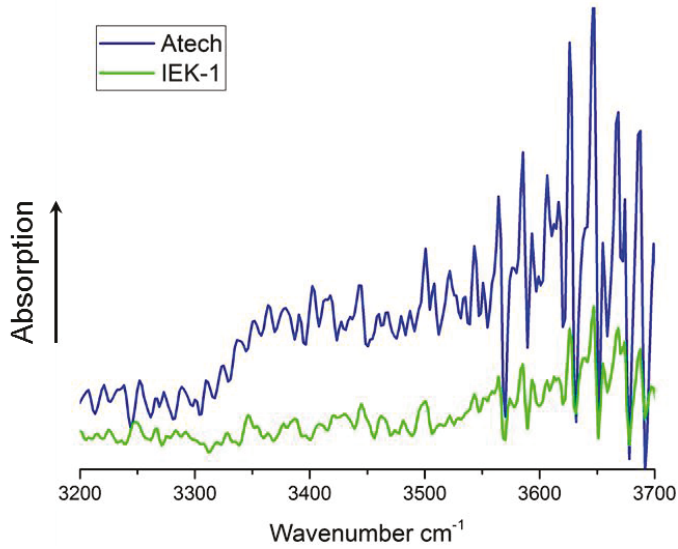


Fig. 85 IR-spectra of SiO<sub>2</sub>-membrane with Atech substrate and with IEK-1 substrate annealed without water vapour

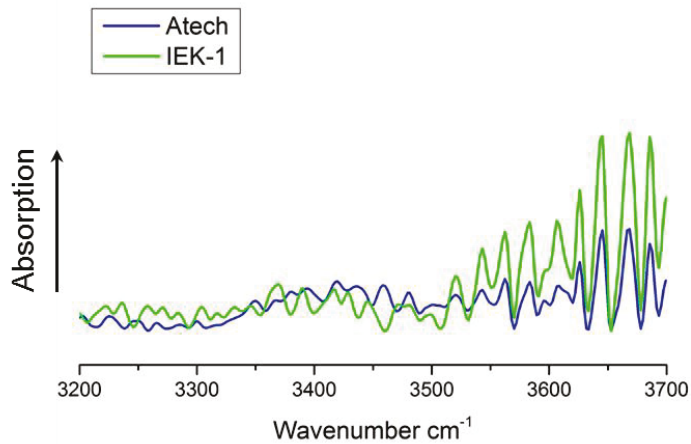


Fig. 86 IR-spectra of SiO<sub>2</sub>-membrane with Atech substrate and with IEK-1 substrate annealed with water vapour

Considering the absolute IR-adsorption intensity, the amount of water molecules in SiO<sub>2</sub>-membrane on IEK-1 substrate rises slightly. The reduction of the amount of water molecules in SiO<sub>2</sub>-membrane on Atech substrate could result from that the humidity in air condensate in the membrane during cooling process after the previous annealing test without water vapour, and the high operating temperatures limiting the adsorption of water molecules in SiO<sub>2</sub>-

membrane despite of the presence of water vapour in the later annealing test. While the SiO<sub>2</sub>-membrane on IEK-1 substrate has larger thickness and defect-free structure as discussed above, thus, the as the temperature increases, the water molecules could be well reserved in the membrane after cooling down.

Other noteworthy IR-bands are at about 875 cm<sup>-1</sup> and 1150 cm<sup>-1</sup>, which increase after annealed with water vapour. Since there is no literature about the group represented by these bands, they could be the OH group from the reaction of Si=O group with H<sub>2</sub>O molecule, like that band at 1410 cm<sup>-1</sup>.

#### 6.4.2 Amino-modified SiO<sub>2</sub>-membrane with ceramic IEK-1 substrate

Fig. 87 shows the comparison of infrared spectrum for the pure SiO<sub>2</sub>-membrane and amino-modified SiO<sub>2</sub>-membrane before annealing with water vapour. The Si-O-Si stretching indicated by the band at 1240 cm<sup>-1</sup> cannot be found in the infrared spectrum of amino-modified SiO<sub>2</sub>-membrane. Furthermore, the main peak at 1080 cm<sup>-1</sup> assigning asymmetric Si-O-Si stretching decrease and undergoes a shift to lower wavenumber. This shift phenomenon of Si-O-Si stretching is also found in carbon-containing SiO<sub>2</sub>-membrane obtained by CVD. In the study of Creatore et al. [174], the band at 1080 cm<sup>-1</sup> is shifted towards higher wavenumber, when the oxygen content increases during the coating process, i.e. the coating layer more SiO<sub>2</sub>-structure. Therefore, the shift of band at 1080 cm<sup>-1</sup> to lower wavenumber could result from the decline of the amount of Si=O group through the anchor of 3-aminopropyl-group on the membrane.

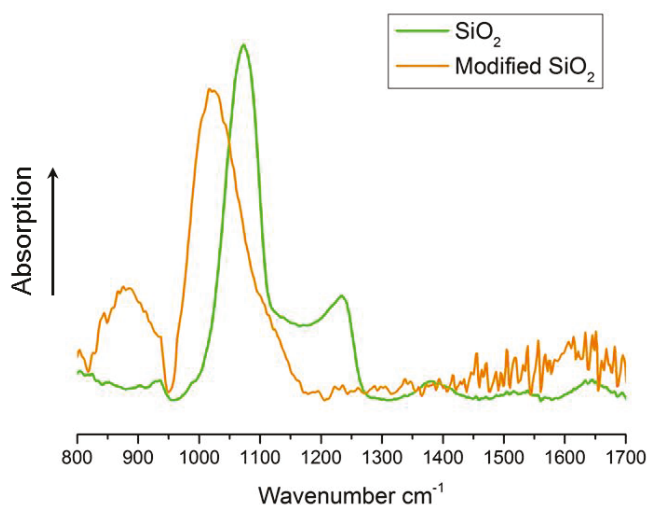


Fig. 87 IR-spectra of SiO<sub>2</sub>-membrane and amino-modified SiO<sub>2</sub>-membrane on IEK-1 substrate annealed without water vapour

Compared with in the infrared spectrum of pure SiO<sub>2</sub>-membrane, the infrared spectrum of amino-modified SiO<sub>2</sub>-membrane has already a significantly intensive band at about 875 cm<sup>-1</sup> before annealed with water vapour. Since the band at 875 cm<sup>-1</sup> could represent OH group as discussed above, this phenomenon could be contribute to the higher affinity and absorption of amino-modified SiO<sub>2</sub>-membrane than that of pure SiO<sub>2</sub>-membrane even at room temperature.

Furthermore, infrared spectrum of amino-modified SiO<sub>2</sub>-membrane appears to have obvious noise signal rather than that of pure SiO<sub>2</sub>-membrane. This could be due to the 3-aminopropyl-group on the membrane which results in a lack of contact between specimen surface and measuring crystal.

Fig. 88 shows the comparison of infrared spectrum for the pure SiO<sub>2</sub>-membrane and amino-modified SiO<sub>2</sub>-membrane before annealing without water vapour. The bands at 875 cm<sup>-1</sup> and 1150 cm<sup>-1</sup> of infrared spectrum of amino-modified SiO<sub>2</sub>-membrane has a significantly higher intensity, this indicates a much higher amount of OH group on the SiO<sub>2</sub>-membrane surface.

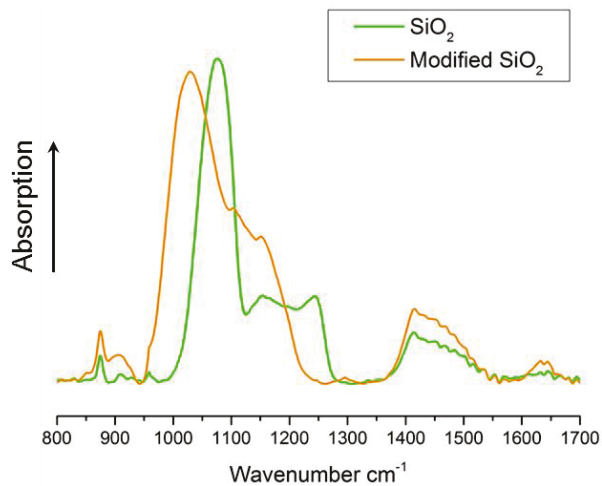


Fig. 88 IR-spectra of SiO<sub>2</sub>-membrane and amino-modified SiO<sub>2</sub>-membrane on IEK-1 substrate annealed with water vapour

However, the increase of band 1410 cm<sup>-1</sup> and 1500 cm<sup>-1</sup> results not only from the increase of band at 1410 cm<sup>-1</sup> due to more OH-group, but also form the increase of band 1385 cm<sup>-1</sup>, which assigns to the formation of bicarbonate [71]. This can also be proved by a slight intense band at 1650 cm<sup>-1</sup> which indicates a stretching C=O group. Furthermore, in Fig. 89, the band between 2960 and 2970 increases indicating the stretching C-H group associated with formaldehyde [71, 177].

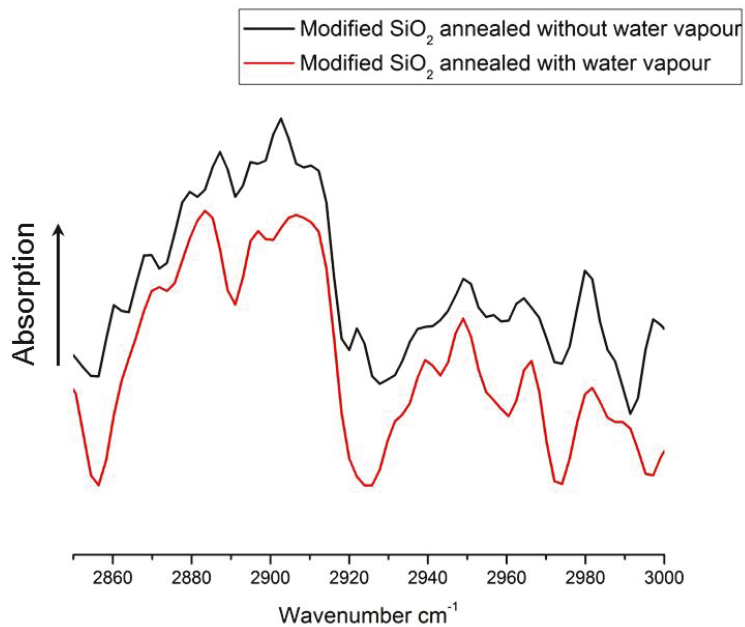


Fig. 89 IR-spectra of amino-modified SiO<sub>2</sub>-membrane on IEK-1 substrate annealed without and with water vapour

The evidence above has proven that bicarbonate has formed from carbon dioxide molecules and one amino-group in the presence of water (Fig. 91). This explains why the CO<sub>2</sub>/N<sub>2</sub> selectivity of amino-modified SiO<sub>2</sub>-membrane is higher in presence of water vapour than without water vapour.

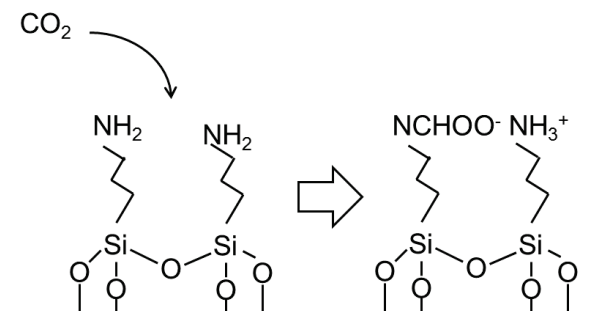


Fig. 90 Reaction of CO<sub>2</sub> on the silica surface with 3-aminopropyl-group [169]

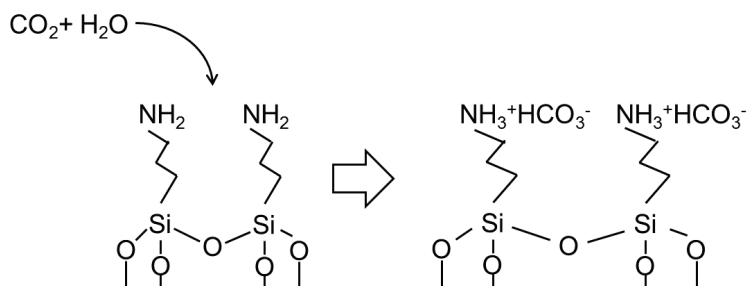


Fig. 91 Reaction of CO<sub>2</sub> and H<sub>2</sub>O on the silica surface with 3-aminopropyl-group [169]



## 7 Conclusions

Within the project METPOREIL, the mechanical and permeation properties of SiO<sub>2</sub>- and amino-modified SiO<sub>2</sub>-membranes deposited on various ceramic and metallic substrates from Atech, IEK-1 and Plansee, were investigated.

Two ceramic substrate materials for SiO<sub>2</sub>-membranes, i.e. produced by Atech and IEK-1 substrate, respectively, were compared regarding the mechanical properties. The statistically evaluated bending tests results revealed that the mechanical properties of the membrane system mainly depend on the microstructure of the substrate materials. The nano-porous substrate yielded significantly higher fracture strength and Young's modulus than the micro-porous Atech substrate, even though both of them had similar porosity. However, the Weibull-Modulus for IEK-1 materials was lower than that of the Atech substrates, indicating a wider spread of the failure relevant flaw population.

In addition, mechanical properties and the microstructural influence were also determined via the aid of indentation tests, which showed for higher loads (larger deformed volumes) good agreement with bending test based Young's moduli.

It was verified that the mechanical properties of the porous materials depended on the contact areas of grains which was explained by a Knudsen's model. The nano-porous material appeared also to be superior in terms of fracture strength and Young's modulus to other membrane substrate materials suggested in literature, indicating the potential of nano-porous materials for the use as porous substrates.

In addition, the mechanical properties of specimens with the porous metallic substrate ITM were tested along with acoustic emission tests, in order to analyse the failure of the coating system. It was determined that micro-cracks emerged at a load of 620 N corresponding to a strain of 0.36 %. At a load of 767 N (strain 0.44 %), cracks grew to the suspension layer. Finally, when the load was increased to 1853 N (strain of 1.12 %), the coating system delaminated. These parameters should be considered for the application of SiO<sub>2</sub>-membranes on porous ITM substrate.

With respect to permeation tests, the gas permeability of various gases through SiO<sub>2</sub>- and amino-modified SiO<sub>2</sub>-membranes were measured with single gas, binary gas mixtures and binary gas mixtures plus water vapour.

The gas transport mechanism of both SiO<sub>2</sub>- and amino-modified SiO<sub>2</sub>-membrane with different substrates was investigated. For SiO<sub>2</sub>-membranes on Atech substrates, the gas molecules were transported by Knudsen's diffusion in single gas permeation tests. Molecular

sieving effects appeared to dominate for the membranes on IEK-1 substrates, especially for small gas molecules like helium and probably also in the case of the CO<sub>2</sub>/N<sub>2</sub> separation, which is related to the refined microstructure and optimized interface quality between substrate and coating system. SiO<sub>2</sub>-membranes on IEK-1 substrates, which were investigated through binary gas permeation tests, exhibited surface diffusion of gas molecules. Furthermore, with the presence of water vapour in the feed gas, the CO<sub>2</sub>/N<sub>2</sub> selectivity was significantly enhanced below 150 °C. However, in such condition, both water molecules anchoring onto the pore wall and group transformation from Si=O group to Si-O-H resulted in the shrinkage of the pores, which led to a decrease of the gas permeation. At the temperatures above 150 °C, the previously mentioned enhancement of CO<sub>2</sub>/N<sub>2</sub> selectivity disappeared.

For amino-modified SiO<sub>2</sub>-membranes on IEK-1 substrates, the CO<sub>2</sub>/N<sub>2</sub> selectivity increased with increasing temperature due to the higher affinity between CO<sub>2</sub> molecules and amino-group on the SiO<sub>2</sub> pore wall. The CO<sub>2</sub>/N<sub>2</sub> selectivity was significantly enhanced with the presence of water vapour, even at temperatures above 150 °C. However, the gas permeation decreased as the pores shrunk due to the same reason as in the case of SiO<sub>2</sub>-membranes on IEK-1 substrates. But contrarily, at 190 °C, the gas permeation with water vapour exceeded that without water vapour, which requires future studies.

The mechanism for the enhancement of the CO<sub>2</sub>/N<sub>2</sub> selectivity under water vapour conditions was also investigated through infrared spectrometry. The number of water molecules and OH-group on amino-modified SiO<sub>2</sub>-membranes was much higher than that on pure SiO<sub>2</sub>-membranes, which proved that there were more C=O groups and C-H groups after annealing under water vapour conditions. This conclusion indicates that the bicarbonate formation from one carbon dioxide molecule and one amino-group with water, partially substitutes the carbamate formation from one carbon dioxide molecule and two amino-groups without water. Thus, the adsorption of carbon dioxide molecules within the membrane was significantly improved.

Future work could focus on the high temperature range (above 190 °C) considering the CO<sub>2</sub>/N<sub>2</sub> selectivity and permeation properties of SiO<sub>2</sub>-membrane and amino-modified SiO<sub>2</sub>-membrane. Furthermore, the reproducibility issue needs to be improved to facilitate the mass production of membrane with high CO<sub>2</sub>/N<sub>2</sub> selectivity.

---

## References

1. Ellett, A.J., *Oxygen permeation and thermo-chemical stability of oxygen separation membrane materials for the oxyfuel process*. Schriften des Forschungszentrums Jülich. Reihe Energie und Umwelt / energy and environment. 2009, Jülich: Forschungszentrum, Zentralbibliothek. 176 S.
2. *International Energy Agency: World Energy Outlook*. 2006.
3. T.F.Stocker, D.Q., *IPCC, Climate Change 2013: The Physical Science Basis. Contribution of Working Group I to the Fifth Assessment Report of the Intergovernmental Panel on Climate Change*. 2013: Cambridge, United Kindom and New York, NY, USA. p. 1535.
4. Hauler, F., *Herstellung und Charakterisierung von keramik- und metallgestützten Membranschichten für die CO<sub>2</sub>-Abtrennung in fossilen Kraftwerken*. Schriften des Forschungszentrums Jülich. Reihe Energie und Umwelt / energy and environment. 2010, Jülich: Forschungszentrum, Zentralbibliothek. XVIII, 178 S.
5. *Bundesministerium für Wirtschaft und Arbeit - Referat Kommunikation und Internet: Forschungs- und Entwicklungskonzept für emissionsarme fossil befeuerte Kraftwerke, Bericht der COORETEC-Arbeitsgruppen*. 2003: Berlin.
6. Göttlicher, G., *Entwicklungsmöglichkeiten der CO<sub>2</sub>-Rückhaltung in Kraftwerken aus thermodynamischer Sicht*. Chemie Ingenieur Technik, 2006. **78**(4): p. 407-415.
7. Hendriks, C., *Carbon dioxide removal from coal fired power plants*. 233 S. Energy and environment ; vol 0001. 1994, Dordrecht: Kluwer Academic Publ.
8. Buhre, B.J.P., et al., *Oxy-fuel combustion technology for coal-fired power generation*. Progress in Energy and Combustion Science, 2005. **31**(4): p. 283-307.
9. Brands, K., *Entwicklung und Charakterisierung eines metallischen Substrats für nanostrukturierte keramische Gastrennmembranen*. Schriften des Forschungszentrums Jülich. Reihe Energie und Umwelt / energy and environment. 2010, Jülich: Forschungszentrum, Zentralbibliothek. VII, 137 S.
10. Bonekamp, B.C., *Chapter 6 Preparation of asymmetric ceramic membrane supports by dip-coating*, in *Membrane Science and Technology*, A.J. Burggraaf and L. Cot, Editors. 1996, Elsevier. p. 141-225.
11. Lashof, D.A. and D.R. Ahuja, *Relative contributions of greenhouse gas emissions to global warming*. Nature, 1990. **344**(6266): p. 529-531.
12. Aaron, D. and C. Tsouris, *Separation of CO<sub>2</sub> from Flue Gas: A Review*. Separation Science and Technology, 2005. **40**(1-3): p. 321-348.
13. Kanniche, M., et al., *Pre-combustion, post-combustion and oxy-combustion in thermal power plant for CO<sub>2</sub> capture*. Applied Thermal Engineering, 2010. **30**(1): p. 53-62.
14. Figueroa, J.D., et al., *Advances in CO<sub>2</sub> capture technology—The U.S. Department of Energy's Carbon Sequestration Program*. International Journal of Greenhouse Gas Control, 2008. **2**(1): p. 9-20.
15. Gibbins, J. and H. Chalmers, *Carbon capture and storage*. Energy Policy, 2008. **36**(12): p. 4317-4322.
16. Descamps, C., C. Bouallou, and M. Kanniche, *Efficiency of an Integrated Gasification Combined Cycle (IGCC) power plant including CO<sub>2</sub> removal*. Energy, 2008. **33**(6): p. 874-881.

17. Metz, B., *IPCC special report on carbon dioxide capture and storage*. 2005, Cambridge: Cambridge Univ. Press. X, 431 S.
18. Amelio, M., et al., *Integrated gasification gas combined cycle plant with membrane reactors: Technological and economical analysis*. Energy Conversion and Management, 2007. **48**(10): p. 2680-2693.
19. Matsuyama, H., et al., *Facilitated transport of CO<sub>2</sub> through various ion exchange membranes prepared by plasma graft polymerization*. Journal of Membrane Science, 1996. **117**(1-2): p. 251-260.
20. Chen, H., et al., *Selective CO<sub>2</sub> Separation from CO<sub>2</sub>-N<sub>2</sub> Mixtures by Immobilized Carbonate-Glycerol Membranes*. Industrial & Engineering Chemistry Research, 1999. **38**(9): p. 3489-3498.
21. Kovvali, A.S. and K.K. Sirkar, *Dendrimer Liquid Membranes: CO<sub>2</sub> Separation from Gas Mixtures*. Industrial & Engineering Chemistry Research, 2001. **40**(11): p. 2502-2511.
22. Wall, T.F., *Combustion processes for carbon capture*. Proceedings of the Combustion Institute, 2007. **31**(1): p. 31-47.
23. Metz, B., et al., *Carbon dioxide capture and storage*. 2005.
24. Czaperek, M., et al., *Gas separation membranes for zero-emission fossil power plants: MEM-BRAIN*. Journal of Membrane Science, 2010. **359**(1-2): p. 149-159.
25. Eiberger, J.S., *Entwicklung von porösen Silica-Membranen zur CO<sub>2</sub>-Abtrennung aus dem Rauchgas fossil befeuerter Kraftwerke*. Schriften des Forschungszentrums Jülich. Reihe Energie und Umwelt / energy and environment. 2014, Jülich: Forschungszentrum, Zentralbibliothek. II, 163 S.
26. E. Fitzer, D.S., *Stickoxid-Emission industrieller Feuerungsanlagen in Abhängigkeit von deren Betriebsbedingungen*. Chemie Ingenieur Technik, 1975. **47**: p. 571.
27. R. Römer, W.L., A. Stoeckel, G. Hemmer, *Beeinflussung der Stickoxid-Bildung aus brennstoffgebundenem Stickstoff durch feuerungstechnische Maßnahmen*. Chemie Ingenieur Technik, 1981. **53**: p. 128-129.
28. Strauß, K., *Kraftwerkstechnik zur Nutzung fossiler, nuklearer und regenerativer Energiequellen*. VDI-Buch. 2009, Berlin, Heidelberg: Springer-Verlag Berlin Heidelberg. online resource.
29. H. Herzog, J.M., A. Hatton, *Advanced post-combustion CO<sub>2</sub> capture*. MIT Energy Initiative, 2009.
30. Favre, E., *Membrane processes and postcombustion carbon dioxide capture: Challenges and prospects*. Chemical Engineering Journal, 2011. **171**(3): p. 782-793.
31. Feron, P., A. Jansen, and R. Klaassen, *Membrane technology in carbon dioxide removal*. Energy Conversion and Management, 1992. **33**(5): p. 421-428.
32. Drioli, E. and M. Romano, *Progress and New Perspectives on Integrated Membrane Operations for Sustainable Industrial Growth*. Industrial & Engineering Chemistry Research, 2001. **40**(5): p. 1277-1300.
33. Mulder, M., *Basic Principles of Membrane Technology*. 1996, Dordrecht: Kluwer Academic Publisher.
34. Lin, Y.S., *Microporous and dense inorganic membranes: current status and prospective*. Separation and Purification Technology, 2001. **25**(1-3): p. 39-55.

35. Koresh, J.E. and A. Sofer, *Molecular sieve carbon permselective membrane. Part I. Presentation of a new device for gas mixture separation*. Separation Science and Technology, 1983. **18**(8): p. 723-734.
36. Burggraaf, A.J., *Chapter 2 Important characteristics of inorganic membranes*, in *Membrane Science and Technology*, A.J. Burggraaf and L. Cot, Editors. 1996, Elsevier. p. 21-34.
37. Hsieh, H.P., *Membranes and Membrane Processes*, in *Inorganic membranes for separation and reactions*. 1996, Elsevier Science B.V.: New York. p. 1-13.
38. Burggraaf, A.J., *Chapter 9 Transport and separation properties of membranes with gases and vapours*, in *Membrane Science and Technology*, A.J. Burggraaf and L. Cot, Editors. 1996, Elsevier. p. 331-433.
39. Hsieh, H.P., *Gas-phase and non-traditional separation applications*, in *Inorganic membranes for separation and reactions*. 1996, Elsevier Science B.V.: New York. p. 249-297.
40. Li, K., *Transport and Separation of Gases in Porous Ceramic Membranes*, in *Ceramic Membranes for Separation and Reaction*. 2007, John Wiley & Sons, Ltd. p. 97-134.
41. J. Rouquerol, D.A., C. W. Fairbridge, D. H. Everett, J. M. Haynes, N. Pernicone, J. D. F. Ramsay, K. S. W. Sing, K. K. Unger, *Recommendations for the characterization of porous solids (Technical Report)*. Pure Appl. Chem., 1994. **66**(8): p. 1739-1758.
42. Burggraaf, A.J. and L. Cot, *Chapter 1 General overview, trends and prospects*, in *Membrane Science and Technology*, A.J. Burggraaf and L. Cot, Editors. 1996, Elsevier. p. 1-20.
43. Pandey, P. and R. Chauhan, *Membranes for gas separation*. Progress in Polymer Science, 2001. **26**(6): p. 853-893.
44. Rautenbach, T.M.a.R., *Gas permeation*, in *Membranverfahren*. 2007, Springer-Verlag: Berlin, Heidelberg, New York. p. 447-504.
45. Rautenbach, T.M.a.R., *Modellierung des Stofftransportes in Membranen*, in *Membranverfahren*. 2007, Springer-Verlag: Berlin, Heidelberg, New York. p. 71-116.
46. Milella, A., et al., *Remote Plasma Deposited Silicon Dioxide - Like Film Densification by Means of RF Substrate Biasing: Film Chemistry and Morphology*. Plasma Processes and Polymers, 2007. **4**(6): p. 621-628.
47. Breck, D.W., *Adsorption by Dehydrated Zeolite Crystals*, in *Zeolite Molecular Sieves - Structure, Chemistry, and Use*. 1974, John Wiley & Sons, Inc.: New York. p. 593-724.
48. Lu, G.Q., et al., *Inorganic membranes for hydrogen production and purification: A critical review and perspective*. Journal of Colloid and Interface Science, 2007. **314**(2): p. 589-603.
49. de Lange, R.S.A., et al., *Permeation and separation studies on microporous sol-gel modified ceramic membranes*. Microporous Materials, 1995. **4**(2-3): p. 169-186.
50. Schramm, O. and A. Seidel-Morgenstern, *Comparing porous and dense membranes for the application in membrane reactors*. Chemical engineering science, 1999. **54**(10): p. 1447-1453.
51. Bouwmeester, H.J.M. and A.J. Burggraaf, *Chapter 10 Dense ceramic membranes for oxygen separation*, in *Membrane Science and Technology*, A.J. Burggraaf and L. Cot, Editors. 1996, Elsevier. p. 435-528.

52. Larbot, A., *Chapter 5 Ceramic processing techniques of support systems for membranes synthesis*, in *Membrane Science and Technology*, A.J. Burggraaf and L. Cot, Editors. 1996, Elsevier. p. 119-139.
53. Tan, X. and K. Li, *Inorganic Membrane Reactors: Fundamentals and Applications*. 2015: John Wiley & Sons.
54. Winningham, T.A. and K. Douglas, *Intermediate transfer layers for nanoscale pattern transfer and nanostructure formation*. 2003, Google Patents.
55. Van Gestel, T., et al., *ZrO<sub>2</sub> and TiO<sub>2</sub> membranes for nanofiltration and pervaporation: Part 1. Preparation and characterization of a corrosion-resistant ZrO<sub>2</sub> nanofiltration membrane with a MWCO < 300*. *Journal of Membrane Science*, 2006. **284**(1): p. 128-136.
56. de Lange, R.S.A., et al., *Microporous SiO<sub>2</sub> and SiO<sub>2</sub>/MO<sub>x</sub> (M=Ti, Zr, Al) for ceramic membrane applications: A microstructural study of the sol-stage and the consolidated state*. *Journal of Sol-Gel Science and Technology*, 1994. **2**(1-3): p. 489-495.
57. Van Gestel, T., et al., *Manufacturing of new nano-structured ceramic-metallic composite microporous membranes consisting of ZrO<sub>2</sub>, Al<sub>2</sub>O<sub>3</sub>, TiO<sub>2</sub> and stainless steel*. *Solid State Ionics*, 2008. **179**(27-32): p. 1360-1366.
58. Moon, H.J., *Development of thin film inorganic membranes for oxygen separation*. Vol. 136. 2012: Forschungszentrum Jülich.
59. Wang, J., et al., *Study of slurry spin coating technique parameters for the fabrication of anode-supported YSZ Films for SOFCs*. *Journal of power sources*, 2007. **164**(1): p. 17-23.
60. Morooka, S. and K. Kusakabe, *Microporous inorganic membranes for gas separation*. *MRS Bulletin*, 1999. **24**(03): p. 25-29.
61. Levy, R.A., et al., *Microporous SiO<sub>2</sub>/Vycor membranes for gas separation*. *Journal of Materials Research*, 1996. **11**(12): p. 3164-3173.
62. Kitao, S. and M. Asaeda. *Gas separation performance of thin porous silica membrane prepared by sol-gel and CVD methods*. in *Key Engineering Materials*. 1992. Trans Tech Publ.
63. de Vos, R.M. and H. Verweij, *High-Selectivity, High-Flux Silica Membranes for Gas Separation*. *Science*, 1998. **279**(5357): p. 1710-1711.
64. Goj, A., et al., *Atomistic Simulations of CO<sub>2</sub> and N<sub>2</sub> Adsorption in Silica Zeolites: The Impact of Pore Size and Shape*. *The Journal of Physical Chemistry B*, 2002. **106**(33): p. 8367-8375.
65. Hochstrasser, G. and J.F. Antonini, *Surface states of pristine silica surfaces: I. ESR studies of Es' dangling bonds and of CO<sub>2</sub>- adsorbed radicals*. *Surface Science*, 1972. **32**(3): p. 644-664.
66. Sartori, G. and D.W. Savage, *Sterically hindered amines for carbon dioxide removal from gases*. *Industrial & Engineering Chemistry Fundamentals*, 1983. **22**(2): p. 239-249.
67. D'Alessandro, D.M., B. Smit, and J.R. Long, *Carbon Dioxide Capture: Prospects for New Materials*. *Angewandte Chemie International Edition*, 2010. **49**(35): p. 6058-6082.
68. Becker, N. and K.K. Unger, *Separation studies of amino acids, proteins and enzymes on bonded 1,2-dihydroxy-, 1,2-hydroxylamino- and amino silica packings*. *Chromatographia*, 1979. **12**(8): p. 539-544.

69. Andersson, J., et al., *Influences of Material Characteristics on Ibuprofen Drug Loading and Release Profiles from Ordered Micro- and Mesoporous Silica Matrices*. Chemistry of Materials, 2004. **16**(21): p. 4160-4167.
70. Leal, O., et al., *Carbon dioxide adsorbent and method for producing the adsorbent*. 1992, Google Patents.
71. Leal, O., et al., *Reversible adsorption of carbon dioxide on amine surface-bonded silica gel*. Inorganica Chimica Acta, 1995. **240**(1-2): p. 183-189.
72. Mani, F., M. Peruzzini, and P. Stoppioni, *CO<sub>2</sub> absorption by aqueous NH<sub>3</sub> solutions: speciation of ammonium carbamate, bicarbonate and carbonate by a <sup>13</sup>C NMR study*. Green Chem., 2006. **8**(11): p. 995-1000.
73. Guizard, C., *Chapter 7 Sol-gel chemistry and its application to porous membrane processing*, in *Membrane Science and Technology*, A.J. Burggraaf and L. Cot, Editors. 1996, Elsevier. p. 227-258.
74. Burggraaf, A.J., *Chapter 8 Fundamentals of membrane top-layer synthesis and processing*, in *Membrane Science and Technology*, A.J. Burggraaf and L. Cot, Editors. 1996, Elsevier. p. 259-329.
75. Scherer, C.J.B.a.G.W., *Film Formation*, in *Sol-gel-science: the physics and chemistry of sol-gel processing*. 1990, Academic Press, Inc.: San Diego. p. 787-838.
76. Malzbender, J. and G. de With, *Cracking and residual stress in hybrid coatings on float glass*. Thin Solid Films, 2000. **359**(2): p. 210-214.
77. Kappert, E.J., et al., *Formation and prevention of fractures in sol-gel-derived thin films*. Soft matter, 2015. **11**(5): p. 882-888.
78. Hench, L.L. and J.K. West, *The sol-gel process*. Chemical Reviews, 1990. **90**(1): p. 33-72.
79. McCool, B.A. and W.J. DeSisto, *Amino - Functionalized Silica Membranes for Enhanced Carbon Dioxide Permeation*. Advanced Functional Materials, 2005. **15**(10): p. 1635-1640.
80. Kim, S., et al., *Tailoring Pore Properties of MCM-48 Silica for Selective Adsorption of CO<sub>2</sub>*. The Journal of Physical Chemistry B, 2005. **109**(13): p. 6287-6293.
81. Kim, J., et al., *Formation, structure, and reactivity of amino-terminated organic films on silicon substrates*. Journal of Colloid and Interface Science, 2009. **329**(1): p. 114-119.
82. Siqueira Petri, D.F., et al., *An Improved Method for the Assembly of Amino-Terminated Monolayers on SiO<sub>2</sub> and the Vapor Deposition of Gold Layers*. Langmuir, 1999. **15**(13): p. 4520-4523.
83. Vandenberg, E.T., et al., *Structure of 3-aminopropyl triethoxy silane on silicon oxide*. Journal of Colloid and Interface Science, 1991. **147**(1): p. 103-118.
84. Ek, S., *Controlled preparation of amino-functionalized surfaces on porous silica by atomic layer deposition*. 2004: Helsinki University of Technology.
85. Puurunen, R.L., *Surface chemistry of atomic layer deposition: A case study for the trimethylaluminum/water process*. Journal of applied physics, 2005. **97**(12): p. 121301.
86. George, S.M., *Atomic layer deposition: an overview*. Chemical reviews, 2009. **110**(1): p. 111-131.
87. Song, C., *Influence of water vapor on silica membranes: Effect of sorption and percolation*. 2005, University of Twente: The Netherlands.

88. Vos, R.d., *High-Selectivity, High-Flux Silica Membranes for Gas Separation: synthesis, transport and stability*, in *Ph.D thesis* 1998, University of Twente: Enschede.
89. Teshima, K., et al., *Gas Barrier Performance of Surface-Modified Silica Films with Grafted Organosilane Molecules*. *Langmuir*, 2003. **19**(20): p. 8331-8334.
90. Capel-Sanchez, M.C., et al., *Silylation and surface properties of chemically grafted hydrophobic silica*. *Journal of Colloid and Interface Science*, 2004. **277**(1): p. 146-153.
91. Rao, A.V. and R. Kalesh, *Organic Surface Modification of TEOS Based Silica Aerogels Synthesized by Co-Precursor and Derivatization Methods*. *Journal of Sol-Gel Science and Technology*, 2004. **30**(3): p. 141-147.
92. Song, C., *Influence of water vapor on silica membranes: Effect of sorption and percolation*. 2005.
93. Wei, Q., et al., *Preparation, hydrogen separation and hydrothermal stability of microporous silica membrane*. *Journal of Inorganic Materials*, 2004. **1**: p. 022.
94. WEI, Q., et al., *Preparation, Characterization and Hydrothermal Stability of Hydrophobic Methyl-modified Silica Membranes [J]*. *Journal of Inorganic Materials*, 2004. **2**: p. 025.
95. Wei, J., G. Pećanac, and J. Malzbender, *Review of mechanical characterization methods for ceramics used in energy technologies*. *Ceramics International*, 2014. **40**(10, Part A): p. 15371-15380.
96. Segal, D., *Chemical synthesis of advanced ceramic materials*. Vol. 1. 1991: Cambridge University Press.
97. Munz, D. and T. Fett, *Mechanisches Verhalten keramischer Werkstoffe: Versagensablauf, Werkstoffauswahl, Dimensionierung*. Vol. 8. 2013: Springer-Verlag.
98. Hammel, E.C., O.L.R. Ighodaro, and O.I. Okoli, *Processing and properties of advanced porous ceramics: An application based review*. *Ceramics International*, 2014. **40**(10, Part A): p. 15351-15370.
99. Sagel-Ransijn, C., et al., *Production of defect-poor nanostructured ceramics of yttria-zirconia*. *Journal of the European Ceramic Society*, 1997. **17**(6): p. 831-841.
100. Foster, A.I., M.L. Sims, and D. Young, *Protective metal oxide films on metal or alloy substrate surfaces susceptible to coking, corrosion or catalytic activity*. 1981, Google Patents.
101. Iniotakis, N., et al., *Hydrogen permeation membrane*. 1987, Google Patents.
102. Zhang, J. and J. Malzbender, *Mechanical characterization of micro- and nano-porous alumina*. *Ceramics International*, 2015. **41**(9, Part A): p. 10725-10729.
103. Lipińska-Chwałek, M., F. Schulze-Küppers, and J. Malzbender, *Strength and elastic modulus of lanthanum strontium cobalt ferrite membrane materials*. *Ceramics international*, 2015. **41**(1): p. 1355-1360.
104. Lipińska-Chwałek, M., L. Kiesel, and J. Malzbender, *Mechanical properties of porous MgO substrates for membrane applications*. *Journal of the European Ceramic Society*, 2014. **34**(10): p. 2519-2524.
105. Baumann, S., et al., *Ultrahigh oxygen permeation flux through supported Ba<sub>0.5</sub>Sr<sub>0.5</sub>Co<sub>0.8</sub>Fe<sub>0.2</sub>O<sub>3-δ</sub> membranes*. *Journal of Membrane Science*, 2011. **377**(1–2): p. 198-205.

106. Serra, J.M., et al., *Oxygen permeation through tape-cast asymmetric all-La<sub>0.6</sub>Sr<sub>0.4</sub>Co<sub>0.2</sub>Fe<sub>0.8</sub>O<sub>3-δ</sub> membranes*. Journal of Membrane Science, 2013. **447**(0): p. 297-305.
107. Pečanac, G., et al., *Strength degradation and failure limits of dense and porous ceramic membrane materials*. Journal of the European Ceramic Society, 2013. **33**(13–14): p. 2689-2698.
108. Vasechko, V., *Thermo-mechanical investigations of reoxidation-stable material concepts for solid oxide fuel cells*. 2014, Aachen, Techn. Hochsch., Diss., 2014.
109. Nam, S.-E., S.-H. Lee, and K.-H. Lee, *Preparation of a palladium alloy composite membrane supported in a porous stainless steel by vacuum electrodeposition*. Journal of Membrane Science, 1999. **153**(2): p. 163-173.
110. Su, C., et al., *Thin palladium film supported on SiO<sub>2</sub>-modified porous stainless steel for a high-hydrogen-flux membrane*. Industrial & engineering chemistry research, 2005. **44**(9): p. 3053-3058.
111. Peters, T.A., et al., *High pressure performance of thin Pd–23%Ag/stainless steel composite membranes in water gas shift gas mixtures; influence of dilution, mass transfer and surface effects on the hydrogen flux*. Journal of Membrane Science, 2008. **316**(1–2): p. 119-127.
112. Rüttinger, M., et al., *Metal-supported cells with comparable performance to anode-supported cells in short-term stack environment*. ECS Transactions, 2011. **35**(1): p. 259-268.
113. De Vos, R.M. and H. Verweij, *Improved performance of silica membranes for gas separation*. Journal of Membrane Science, 1998. **143**(1): p. 37-51.
114. Kusakabe, K., et al., *Pore structure of silica membranes formed by a sol–gel technique using tetraethoxysilane and alkyltriethoxysilanes*. Separation and Purification Technology, 1999. **16**(2): p. 139-146.
115. Tsai, C.-Y., et al., *Dual-layer asymmetric microporous silica membranes*. Journal of membrane science, 2000. **169**(2): p. 255-268.
116. Da Costa, J.D., et al., *Novel molecular sieve silica (MSS) membranes: characterisation and permeation of single-step and two-step sol–gel membranes*. Journal of Membrane Science, 2002. **198**(1): p. 9-21.
117. Pakizeh, M., M. Omidkhah, and A. Zarringhalam, *Synthesis and characterization of new silica membranes using template–sol–gel technology*. International Journal of Hydrogen Energy, 2007. **32**(12): p. 1825-1836.
118. Boffa, V., D. Blank, and J. Ten Elshof, *Hydrothermal stability of microporous silica and niobia–silica membranes*. Journal of Membrane Science, 2008. **319**(1): p. 256-263.
119. Gopalakrishnan, S. and J.C.D. da Costa, *Hydrogen gas mixture separation by CVD silica membrane*. Journal of Membrane Science, 2008. **323**(1): p. 144-147.
120. Oyama, S., et al., *Theory of hydrogen permeability in nonporous silica membranes*. Journal of membrane science, 2004. **244**(1): p. 45-53.
121. Sea, B.-K., K. Kusakabe, and S. Morooka, *Pore size control and gas permeation kinetics of silica membranes by pyrolysis of phenyl-substituted ethoxysilanes with cross-flow through a porous support wall*. Journal of membrane science, 1997. **130**(1): p. 41-52.

122. Xomeritakis, G., C.-Y. Tsai, and C.J. Brinker, *Microporous sol-gel derived aminosilicate membrane for enhanced carbon dioxide separation*. Separation and purification technology, 2005. **42**(3): p. 249-257.
123. Xomeritakis, G., et al., *Tubular ceramic-supported sol-gel silica-based membranes for flue gas carbon dioxide capture and sequestration*. Journal of Membrane Science, 2009. **341**(1-2): p. 30-36.
124. Ostwal, M., et al., *3-Aminopropyltriethoxysilane functionalized inorganic membranes for high temperature CO<sub>2</sub>/N<sub>2</sub> separation*. Journal of Membrane Science, 2011. **369**(1-2): p. 139-147.
125. Sakamoto, Y., et al., *Preparation and CO<sub>2</sub> separation properties of amine-modified mesoporous silica membranes*. Microporous and Mesoporous Materials, 2007. **101**(1-2): p. 303-311.
126. in *Technische Daten der atech Al<sub>2</sub>O<sub>3</sub>*. 2013, ATECH INOVATIONS GMBH: AM WIESENBUSCH 26, 45966 GLADBECK.
127. *Technische Daten der atech Al<sub>2</sub>O<sub>3</sub> - Membranen Typ 1/6*. 2013, ATECH INOVATIONS GMBH: AM WIESENBUSCH 26, 45966 GLADBECK.
128. Besson, S., et al., *Structural study of 3D-hexagonal mesoporous spin-coated sol-gel films*. Journal of Materials Chemistry, 2000. **10**(6): p. 1331-1336.
129. Besson, S., et al., *Phase diagram for mesoporous CTAB-silica films prepared under dynamic conditions*. Journal of Materials Chemistry, 2003. **13**(2): p. 404-409.
130. Besson, S., et al., *A new 3D organization of mesopores in oriented CTAB silica films*. The Journal of Physical Chemistry B, 2000. **104**(51): p. 12095-12097.
131. Abell, A.B., K.L. Willis, and D.A. Lange, *Mercury Intrusion Porosimetry and Image Analysis of Cement-Based Materials*. Journal of Colloid and Interface Science, 1999. **211**(1): p. 39-44.
132. Dang, S.O., *Charakterisierung von asymmetrischen Dünnschichtmembranen aus Ba<sub>0,5</sub>Sr<sub>0,5</sub>Co<sub>0,8</sub>Fe<sub>0,2</sub>O<sub>3-δ</sub> im 3-End-Betrieb*. 2012. p. 44.
133. Bram, M., et al., *Testing of nanostructured gas separation membranes in the flue gas of a post-combustion power plant*. International Journal of Greenhouse Gas Control, 2011. **5**(1): p. 37-48.
134. Malzbender, J. and R.W. Steinbrech, *Fracture test of thin sheet electrolytes for solid oxide fuel cells*. Journal of the European Ceramic Society, 2007. **27**(7): p. 2597-2603.
135. Asmani, M., et al., *Influence of porosity on Young's modulus and Poisson's ratio in alumina ceramics*. Journal of the European Ceramic Society, 2001. **21**(8): p. 1081-1086.
136. Oliver, W.C. and G.M. Pharr, *An improved technique for determining hardness and elastic modulus using load and displacement sensing indentation experiments*. Journal of Materials Research, 1992. **7**(06): p. 1564-1583.
137. Oliver, W.C. and G.M. Pharr, *Measurement of hardness and elastic modulus by instrumented indentation: Advances in understanding and refinements to methodology*. Journal of materials research, 2004. **19**(01): p. 3-20.
138. Brandon, D. and W.D. Kaplan, *Microstructural characterization of materials*. 2013: John Wiley & Sons.
139. Barabash, R.M., et al., *Low-Temperature Fluorination of Silica by a Nonaqueous Solution of NH<sub>4</sub>F*. The Journal of Physical Chemistry A, 2003. **107**(22): p. 4497-4505.

140. Stuart, B.H., *Front Matter*, in *Infrared Spectroscopy: Fundamentals and Applications*. 2005, John Wiley & Sons, Ltd. p. i-xvi.
141. Fischer-Cripps, A.C., *Nanoindentation*. 2002.
142. *Mechanical Properties of Materials*, in *CRC Materials Science and Engineering Handbook, Third Edition*. 2000, CRC Press.
143. Mohanta, K., et al., *Processing and properties of low cost macroporous alumina ceramics with tailored porosity and pore size fabricated using rice husk and sucrose*. Journal of the European Ceramic Society, 2014. **34**(10): p. 2401-2412.
144. Li, X., P. Wu, and D. Zhu, *Properties of porous alumina ceramics prepared by technique combining cold-drying and sintering*. International Journal of Refractory Metals and Hard Materials, 2013. **41**(0): p. 437-441.
145. Wen, C.E., et al., *Compressibility of porous magnesium foam: dependency on porosity and pore size*. Materials Letters, 2004. **58**(3-4): p. 357-360.
146. Isobe, T., et al., *Gas permeability and mechanical properties of porous alumina ceramics with unidirectionally aligned pores*. Journal of the European Ceramic Society, 2007. **27**(1): p. 53-59.
147. Ashizuka, M., et al., *Elastic Modulus, Strength and Fracture Toughness of Alumina Ceramics Containing Pores*. Journal of the Ceramic Society of Japan, 2002. **110**(1282): p. 554-559.
148. Liu, D.-M., *Influence of porosity and pore size on the compressive strength of porous hydroxyapatite ceramic*. Ceramics International, 1997. **23**(2): p. 135-139.
149. Knudsen, F.P., *Dependence of Mechanical Strength of Brittle Polycrystalline Specimens on Porosity and Grain Size*. Journal of the American Ceramic Society, 1959. **42**(8): p. 376-387.
150. Wang, J., *Young's modulus of porous materials*. Journal of Materials Science, 1984. **19**(3): p. 801-808.
151. Wang, S., et al., *Effects of pore size on microstructure, mechanical and dielectric properties of gel casting BN/Si<sub>3</sub>N<sub>4</sub> ceramics with spherical-shaped pore structures*. Journal of Alloys and Compounds, 2013. **581**(0): p. 46-51.
152. Pećanac, G., T. Bause, and J. Malzbender, *Ring-on-ring testing of thin, curved bi-layered materials*. Journal of the European Ceramic Society, 2011. **31**(12): p. 2037-2042.
153. Lee, D., *Studies on hydrogen selective silica membranes and the catalytic reforming of CH<sub>4</sub> with CO<sub>2</sub> in a membrane reactor*. 2003, Virginia Polytechnic Institute and State University.
154. Kanezashi, M. and M. Asaeda, *Hydrogen permeation characteristics and stability of Ni-doped silica membranes in steam at high temperature*. Journal of Membrane Science, 2006. **271**(1-2): p. 86-93.
155. Kitao, S., H. Kameda, and M. Asaeda, *GAS SEPARATION BY THIN POROUS SILICA MEMBRANE OF ULTRA FINE PORES AT HIGH TEMPERATURE*. membrane, 1990. **15**(4): p. 222-227.
156. Uhlhorn, R.J.R., K. Keizer, and A.J. Burggraaf, *Gas and surface diffusion in modified  $\gamma$ -alumina systems*. Journal of Membrane Science, 1989. **46**(2-3): p. 225-241.
157. Bai, C., et al., *Preparation and separation properties of silicalite composite membranes*. Journal of membrane science, 1995. **105**(1): p. 79-87.

158. Li, Y., et al., *Zeolitic imidazolate framework ZIF-7 based molecular sieve membrane for hydrogen separation*. Journal of Membrane Science, 2010. **354**(1–2): p. 48-54.
159. Nair, B.N., et al., *Sol-gel synthesis of molecular sieving silica membranes*. Journal of Membrane Science, 1997. **135**(2): p. 237-243.
160. Hoffmann, J., *Innovative Beschichtungs- und Charakterisierungsmethoden für die nasschemische Herstellung von asymmetrischen Gastrennmembranen auf Basis von SiO<sub>2</sub>*. Schriften des Forschungszentrums Jülich. Reihe Energie und Umwelt / energy and environment. 2013, Jülich: Forschungszentrum, Zentralbibliothek. V, 152 S.
161. Furukawa, S., et al., *Non-equilibrium molecular dynamics simulation study of the behavior of hydrocarbon-isomers in silicalite*. Fluid Phase Equilibria, 2002. **194–197**(0): p. 309-317.
162. Takaba, H., et al., *Molecular dynamics simulation of iso- and n-butane permeations through a ZSM-5 type silicalite membrane*. Journal of Membrane Science, 1997. **134**(1): p. 127-139.
163. Mizukami, K., et al., *Molecular Dynamics Studies of Surface Difference Effect on Gas Separation by Zeolite Membranes*. Japanese Journal of Applied Physics, 2000. **39**(7S): p. 4385.
164. Kusakabe, K., et al., *Formation of a Y-Type Zeolite Membrane on a Porous  $\alpha$ -Alumina Tube for Gas Separation*. Industrial & Engineering Chemistry Research, 1997. **36**(3): p. 649-655.
165. WEI Qi, L.J.-L., SONG Chun-Lin, LIU Wei, CHEN Chu-Sheng, *Preparation, Characterization and Hydrothermal Stability of Hydrophobic Methyl-modified Silica Membranes*. Journal of Inorganic Materials, 2004. **19**(2): p. 417-423.
166. Choi, J.-G., D.D. Do, and H.D. Do, *Surface Diffusion of Adsorbed Molecules in Porous Media: Monolayer, Multilayer, and Capillary Condensation Regimes*. Industrial & Engineering Chemistry Research, 2001. **40**(19): p. 4005-4031.
167. Weh, K., et al., *Permeation of single gases and gas mixtures through faujasite-type molecular sieve membranes*. Microporous and Mesoporous Materials, 2002. **54**(1–2): p. 27-36.
168. Wagner, W. and A. Pruss, *International Equations for the Saturation Properties of Ordinary Water Substance. Revised According to the International Temperature Scale of 1990. Addendum to J. Phys. Chem. Ref. Data 16, 893 (1987)*. Journal of Physical and Chemical Reference Data, 1993. **22**(3): p. 783-787.
169. Hiyoshi, N., K. Yogo, and T. Yashima, *Adsorption characteristics of carbon dioxide on organically functionalized SBA-15*. Microporous and Mesoporous Materials, 2005. **84**(1): p. 357-365.
170. Knowles, G.P., et al., *Aminopropyl-functionalized mesoporous silicas as CO<sub>2</sub> adsorbents*. Fuel Processing Technology, 2005. **86**(14): p. 1435-1448.
171. Olsen, J. and F. Shimura, *Infrared reflection spectroscopy of the SiO<sub>2</sub> - silicon interface*. Journal of applied physics, 1989. **66**(3): p. 1353-1358.
172. Olsen, J.E. and F. Shimura, *Infrared spectroscopy of thin silicon dioxide on silicon*. Applied Physics Letters, 1988. **53**(20): p. 1934-1936.
173. Boehm, H.P., A. V. Kiselev und V. I. Lygin: *Infrared Spectra of Surface Compounds*, John Wiley and Sons, New York und Toronto 1975, XI + 384 Seiten, 182 Abb., Preis: £ 17.60. Berichte der Bunsengesellschaft für physikalische Chemie, 1976. **80**(8): p. 827-827.

- 
174. Creatore, M., et al., *Optical and chemical characterization of expanding thermal plasma-deposited carbon-containing silicon dioxide-like films*. Thin Solid Films, 2008. **516**(23): p. 8547-8553.
  175. Deshmukh, S.C. and E.S. Aydil, *Investigation of SiO<sub>2</sub> plasma enhanced chemical vapor deposition through tetraethoxysilane using attenuated total reflection Fourier transform infrared spectroscopy*. Journal of Vacuum Science & Technology A, 1995. **13**(5): p. 2355-2367.
  176. Agres, L., et al., *Oxygen barrier efficiency of hexamethyldisiloxane/oxygen plasma-deposited coating*. Journal of Applied Polymer Science, 1996. **61**(11): p. 2015-2022.
  177. M. Avram, G.H.M., *Infrared Spectroscopy*. 1972, Wiley-Interscience: New York. p. 342.



## Symbol index

### Latin symbols

A	mm <sup>2</sup>	Active area
D <sub>p</sub>	nm	Diameter of pore
d <sub>N<sub>2</sub></sub>	nm	Kinetic diameter of N <sub>2</sub> molecule
d <sub>CO<sub>2</sub></sub>	nm	Kinetic diameter of CO <sub>2</sub> molecule
d <sub>p</sub>	nm	Pore size
E	GPa	Young's modulus
E <sub>a</sub>	kJ·mol <sup>-1</sup>	Activation energy
E <sub>m</sub>	kJ·mol <sup>-1</sup>	Positive mobility energy
F	mol·s <sup>-1</sup> ·m <sup>-2</sup> ·bar <sup>-1</sup>	Permeation of pure component
F <sub>viscous</sub>	mol·m <sup>-2</sup> ·s <sup>-1</sup> ·Pa <sup>-1</sup>	Poiseuille permeation
F <sub>Kn</sub>	mol·m <sup>-2</sup> ·s <sup>-1</sup> ·Pa <sup>-1</sup>	Knudsen permeation
h	m	Layer thickness or specimen's thickness
J	mol·s <sup>-1</sup> ·m <sup>-2</sup>	Flow rate
M	kg·mol <sup>-1</sup>	Mass of gas molecule
M <sub>a</sub>	kg·mol <sup>-1</sup>	Mass of gas molecule a
M <sub>b</sub>	kg·mol <sup>-1</sup>	Mass of gas molecule b
m	-	Weibull modulus
P	-	Porosity
P <sub>L</sub>	Pa	Pressure of liquid Hg
P <sub>m</sub>	Pa	Average pressure through the membrane
Q <sub>st</sub>	kJ·mol <sup>-1</sup>	Isosteric adsorption heat
R	J·K <sup>-1</sup> ·mol <sup>-1</sup>	Gas constant = 8.31446 J·K <sup>-1</sup> ·mol <sup>-1</sup>
r <sub>1</sub>	mm	Radius of load ring
r <sub>2</sub>	mm	Radius of support ring
r <sub>3</sub>	mm	radius of the specimen
$\bar{r}$	m	Modal pore radius
T	K	Absolute temperature
x	-	Material fraction in feed mixture
y	-	Material fraction in sweep mixture

### Greek symbols

α	-	Selectivity of gas separation
---	---	-------------------------------

$\alpha_{\text{CO}_2/\text{N}_2(\text{ideal})}$	-	Selectivity of ideal Knudsen diffusion for $\text{CO}_2/\text{N}_2$
$\alpha_{\text{He}/\text{CO}_2(\text{ideal})}$	-	Selectivity of ideal Knudsen diffusion for He/ $\text{CO}_2$
$\alpha_{\text{He}/\text{N}_2(\text{ideal})}$	-	Selectivity of ideal Knudsen diffusion for He/ $\text{N}_2$
$\alpha_{\text{Knudsen a/b}}$	-	Selectivity of gas molecules a and b
$\Delta F$	N	Force
$\Delta f$	N	Deflection
$\varepsilon$	%	Porosity
	-	Strain
$\eta$	$\text{N}\cdot\text{s}\cdot\text{m}^{-2}$	Gas viscosity
$\theta$	$^\circ$	Contact angle of liquid Hg
$\mu_{\text{Kn}}$	-	Form factor
$\mu_p$	-	Reciprocal sinuousness of the pores
$\nu$	-	Poisson 's ratio
$\bar{v}$	$\text{m}\cdot\text{s}^{-1}$	Average molecule tempo
$\pi$	3.14	
$\sigma$	MPa	Surface tensile stress of liquid Hg
$\zeta_c$	MPa	Fracture strength
$\zeta_0$	MPa	Characteristic fracture stress

### Abbreviations

ALD	Atomic layer deposition
APTMS	(3-Aminopropyl) triethoxysilane
BSCF	$(\text{BaSr})(\text{CoFe})\text{O}_{3-\delta}$
CCS	Carbon capture and storage
CGO	$\text{Ce}_{0.9}\text{Gd}_{0.1}\text{O}_{2-\delta}$
CVD	Chemical vapour deposition
EBSD	Electron backscatter diffraction
EDS	Energy-dispersive X-ray spectroscopy
IR	Infrared spectroscopy
ITM	Intermediate- Temperature- Metal
LSCF	$(\text{LaSr})(\text{CoFe})\text{O}_{3-\delta}$
PTES	Phenylethoxysilane
RT	Room tmperature
SE	Secondary electron
SEM	Scanning electron microscope

SOFC	Solid oxide fuel cell
TEOS	Tetraethyl orthosilicate
8YSZ	8% yttrium-partially-stabilized zirconia

---

## Figure index

Fig. 1 Schematic diagram of a power plant with the pre-combustion process (Source: Vattenfall). .....	6
Fig. 2 Schematic diagram of a power plant with oxyfuel process (Source: Vattenfall). .....	7
Fig. 3 Schematic diagram of a power plant with the post-combustion process (Source: Vattenfall). .....	9
Fig. 4 Two gas separation method with membrane: Dead-end-method (left) and Cross-flow-method (right). .....	10
Fig. 5 Principal relationship between separation factor and permeation [42]. .....	12
Fig. 6 Gas separation mechanism in porous membranes: a) Knudsen-diffusion, b) molecular sieving, c) surface diffusion, d) capillary condensation [9]. .....	13
Fig. 7 Structure of a graded porous membrane [9]. .....	17
Fig. 8 Schematic function principle of a modified silica pore wall. ....	18
Fig. 9 Reaction of CO <sub>2</sub> and H <sub>2</sub> O on the silica surface with 3-aminopropyl-group [70, 71]. ..	19
Fig. 10 Overview of sol-gel processes for the production of the inorganic membrane layers [73]. .....	20
Fig. 11 Schematic drawing of dip coating process [75]: (a) immersing of the substrate, (b) keeping the substrate in the sol, (c) depositing and draining of the sol, (d) drying of the solvent. ....	21
Fig. 12 Schematical drawing of vertical dip coating (left) and horizontal dip coating (right). ..	21
Fig. 13 Atomic layer deposition (ALD) of the amino-propyl-siloxane layer [84] .....	23
Fig. 14 Example of a Weibull diagram .....	26
Fig. 15 Structure of membrane with Atech substrate. ....	31
Fig. 16 Structure of membrane with IEK-1 substrate. ....	32
Fig. 17 Structure of membrane with ITM substrate. ....	34
Fig. 18 Schematic structure of the single gas testing system .....	35
Fig. 19 Schematic representation of the permeation test facility. ....	36
Fig. 20 Screen shot of the process monitoring software. ....	37
Fig. 21 Recipient of permeation measurement set-up for micro-porous membranes. ....	38
Fig. 22 Schematc drawing of cross-section and photo of the heating box. ....	38
Fig. 23 Installation of recipient into the brackets. ....	39
Fig. 24 Installation of the recipient and brackets into the insulated box. ....	40
Fig. 25 Complete installation of the recipient in the heating box. ....	40
Fig. 26 Heating progress for a 230 °C set point of the heating box for the metallic recipient. ..	41
Fig. 27 Schematic of a quadrupole mass spectrometer (source: Pfeiffer Vacuum). ....	42
Fig. 28 The set-up of long term annealing experiments. ....	43
Fig. 29 Schematic representation of the stability test set-up, with 1) the gas bottles, 2) the mass flow meters, 3) the water-flow meter, 4) the water container, 5) the flow controller unit, 6) the ceramic sample holder, 7) the gas bubblers, 8) the tube furnace and 9) the quartz glass tubes. ....	44
Fig. 30 Set-up of the ring-on-ring bending test (source: IEK-2, FZJ). ....	45
Fig. 31 Acoustic emission testing unit (AMSY-5, Vallen Systeme GmbH) .....	48
Fig. 32 Schematic principle of set-up of ring-on-ring bending test combined with acoustic emission testing unit (source: IEK-2, FZJ). ....	48
Fig. 33 Combination of ring-on-ring bending testing unit and acoustic emission testing unit (source: IEK-2, FZJ). ....	49

Fig. 34 Schematic representation of a typical indentation load-displacement [137].....	50
Fig. 35 Fracture surface of specimen with Atech substrate (source: IEK-1).....	53
Fig. 36 SEM images of cross section of the specimen side to be coated (left) and coated (right) .....	54
Fig. 37 left: $\gamma$ -Al <sub>2</sub> O <sub>3</sub> -interlayer with modified silica layer on top [25].....	54
Fig. 38 SEM image of cross section of the ITM substrate with two 8YSZ suspension layers (source: IEK-1).....	55
Fig. 39 Porosity and pore size distribution of Atech and IEK-1 substrates measured by mercury porosimetry.....	55
Fig. 40 Weibull-plot of fracture strengths of all specimens with Atech substrate .....	56
Fig. 41 SEM-image of fracture surfaces of Atech substrate after ring-on-ring bending test (fracture stress = 37 MPa) .....	58
Fig. 42 Weibull-plot of fracture strengths of all the specimens with IEK-1 substrate .....	58
Fig. 43 SEM image close to the interlayer for fractured specimen with IEK-1 substrate after ring-on-ring bending test under the loading configuration “SiO <sub>2</sub> membrane on tensile side” (stress: left 92 MPa, right 213 MPa) .....	60
Fig. 44 SEM image close to interlayer for fractured specimen with IEK-1 substrate after ring- on-ring bending test under the load configuration “SiO <sub>2</sub> membrane on compressive side” (stress: left 103 MPa, right 171 MPa) .....	60
Fig. 45 SEM image close to the interlayer for fractured specimen with Atech substrate after ring-on-ring bending test under the loading configuration “SiO <sub>2</sub> membrane on tensile side” (stress: left 31 MPa, right 48 MPa) .....	61
Fig. 46 SEM image close to interlayer for fractured specimen with Atech substrate after ring- on-ring bending test under the load configuration “SiO <sub>2</sub> membrane on compressive side” (stress: left 28 MPa, right 54 MPa) .....	61
Fig. 47 Defects in the suspension layer of the specimens with Atech substrates.....	62
Fig. 48 Loading and unloading curves of nano-indentation test on Atech substrate and IEK-1 substrate.....	62
Fig. 49 Indentation mark on the cross section of the IEK-1 substrate.....	62
Fig. 50 Young’s moduli of IEK-1 substrates measured by nano-indentation test as the function of indentation depth.....	63
Fig. 51 Young’s moduli of Atech substrates measured by nano-indentation test as the function of indentation depth.....	64
Fig. 52 Weibull plot of fracture strengths of all specimens with Atech and IEK-1 substrates, respectively.....	65
Fig. 53 Polished cross-sections and fracture surfaces, (a) (b) IEK-1 substrate, (c) (d) Atech substrate.....	67
Fig. 54 Effect of proe size and porosity on the flexural strength on porous alumina compacts [143] .....	67
Fig. 55 Simple cubic array and unit cell [150] .....	68
Fig. 56 Sequence of events upon densification [150].....	69
Fig. 57 Loading and unloading curves of ring-on-ring bending test with metal substrates coated with 8YSZ suspension layer.....	72
Fig. 58 Specimens (diameter 39 mm) consisting of metal substrate and suspension layer after ring-on-ring bending tests: (a) suspension layer on tensile side (1000 N), (b) suspension layer on compressive (1000 N), (c) suspension layer on tensile side with maximal load of 2000 N.....	72

Fig. 59 Deformation of uncoated, partially coated and completely coated specimen as a function of time .....	74
Fig. 60 Deformation and acoustic emission signals of uncoated, partially coated and completely coated specimen as a function of time .....	75
Fig. 61 Schematic cutting way of specimen after deformation testing.....	75
Fig. 62 Cross-section SEM images of specimen consisting of metal substrate and suspension layer .....	76
Fig. 63 Cross-section SEM images of completely coated specimen with metal substrate, suspension layer, interlayer and silica membrane. ....	77
Fig. 64 Permeation of He, CO <sub>2</sub> and N <sub>2</sub> as single gas through the membrane on an Atech substrate at various temperatures as function of kinetic diameter of gas molecules. .	79
Fig. 65 Permeation of He, CO <sub>2</sub> and N <sub>2</sub> as single gas through a silica membrane on IEK-1 substrate at various temperatures as function of kinetic diameter of gas molecules. .	81
Fig. 66 Helium permeation as single gas through silica membrane on a -1 substrate for feed partial pressures of 4 bar and 1 bar at various temperatures.....	83
Fig. 67 Cross-sectional SEM images of the coated side (left: coated Atech substrate, right: coated IEK-1 substrate). ....	84
Fig. 68 Permeation of CO <sub>2</sub> and N <sub>2</sub> through the silica membrane on a IEK-1 substrate at various temperatures and under various feed pressures.....	85
Fig. 69 Selectivity of CO <sub>2</sub> /N <sub>2</sub> under various differential pressures as the function of temperature .....	86
Fig. 70 Schematic principle of the CO <sub>2</sub> and N <sub>2</sub> migration in the porous silica membrane. ...	87
Fig. 71 Permeation of CO <sub>2</sub> and N <sub>2</sub> with and without water vapour through specimen with a IEK-1 substrate at different temperatures and under various pressures. ....	88
Fig. 72 Selectivity of CO <sub>2</sub> /N <sub>2</sub> under various differential pressures as the function of temperature .....	89
Fig. 73 Permeances of CO <sub>2</sub> and N <sub>2</sub> single gases through amino-modified SiO <sub>2</sub> -membrane as a function of temperature ( $\Delta p = 4$ bar).....	92
Fig. 74 Permeances of CO <sub>2</sub> and N <sub>2</sub> as gas mixture through amino-modified SiO <sub>2</sub> -membrane as a function of temperature.....	93
Fig. 75 Schematic principle of the CO <sub>2</sub> and N <sub>2</sub> migration in the amino-modified porous silica membrane .....	94
Fig. 76 Selectivity of CO <sub>2</sub> /N <sub>2</sub> under various differential pressures as the function of temperature .....	94
Fig. 77 Permeances of CO <sub>2</sub> and N <sub>2</sub> as gas mixture with water vapour through amino-modified SiO <sub>2</sub> -membrane as a function of temperature.....	95
Fig. 78 Selectivity of CO <sub>2</sub> /N <sub>2</sub> in permeation tests with binary gas mixture under various differential pressures as the function of temperature.....	95
Fig. 79 The concentration of CO <sub>2</sub> in the permeate gas measured by binary gas mixture permeation tests as function of temperature (Feed gas: 85% N <sub>2</sub> , 15 % CO <sub>2</sub> ).....	96
Fig. 80 The influence of water vapour amount on the permeances of CO <sub>2</sub> and N <sub>2</sub> at 170 °C. 97	
Fig. 81 Permeation of He, CO <sub>2</sub> and N <sub>2</sub> as single gas through the membrane on ITM porous metal substrate at various temperatures as function of kinetic diameter of gas molecules ( $\Delta p = 4$ bar), without pre-deformation .....	98
Fig. 82 Permeation of He, CO <sub>2</sub> and N <sub>2</sub> as single gas through the membrane on ITM porous metal substrate at various temperatures as function of kinetic diameter of gas molecules ( $\Delta p = 4$ bar), with pre-deformation of 100 $\mu\text{m}$ .....	100

Fig. 83 IR-spectra of SiO <sub>2</sub> -membrane with Atech substrate and with IEK-1 substrate annealed without water vapour .....	101
Fig. 84 IR-spectra of SiO <sub>2</sub> -membrane with Atech substrate and with IEK-1 substrate annealed with water vapour .....	102
Fig. 85 IR-spectra of SiO <sub>2</sub> -membrane with Atech substrate and with IEK-1 substrate annealed without water vapour .....	103
Fig. 86 IR-spectra of SiO <sub>2</sub> -membrane with Atech substrate and with IEK-1 substrate annealed with water vapour .....	103
Fig. 87 IR-spectra of SiO <sub>2</sub> -membrane and amino-modified SiO <sub>2</sub> -membrane on IEK-1 substrate annealed without water vapour.....	104
Fig. 88 IR-spectra of SiO <sub>2</sub> -membrane and amino-modified SiO <sub>2</sub> -membrane on IEK-1 substrate annealed with water vapour.....	105
Fig. 89 IR-spectra of amino-modified SiO <sub>2</sub> -membrane on IEK-1 substrate annealed without and with water vapour .....	106
Fig. 90 Reaction of CO <sub>2</sub> on the silica surface with 3-aminopropyl-group [169].....	106
Fig. 91 Reaction of CO <sub>2</sub> and H <sub>2</sub> O on the silica surface with 3-aminopropyl-group [169]....	107

## Table index

Table 1 Kinetic diameter and molecule mass of selected gases [47].	15
Table 2 Comparison of the mechanical properties of the different ceramic substrate materials	27
Table 3 Parameters of porous ITM at room temperature [108].	27
Table 4 Data of selected silica membranes from literatures.	28
Table 5 Data of selected amino-modified silica membranes from literatures.	29
Table 6 The results of the CO <sub>2</sub> /N <sub>2</sub> mixed gas (CO <sub>2</sub> = 20%) permeation tests for Al <sub>2</sub> O <sub>3</sub> substrate and mesoporous silica membranes before and after modification [125].	30
Table 7 Main manufacturing parameters of coating layers on Atech ceramic substrates.	31
Table 8 Main manufacturing parameters of coating layers and IEK-1 ceramic substrates.	33
Table 9 Main manufacturing parameters of coating layers on ITM metallic substrates.	33
Table 10 Various specimens under different annealing condition	43
Table 11 Loading configuration and number of tested specimens with Atech substrate investigated in ring-on-ring bending test	46
Table 12 Loading configuration and number of tested specimens with IEK-1 substrate investigated in ring-on-ring bending test	47
Table 13 Number of specimens for pre-bending tests	49
Table 14 Number of specimens for bending tests with acoustic emission tests	49
Table 15 Pore size from substrate to suspension 2 of Atech substrate (Source: IEK-1)	53
Table 16 Results of ring-on-ring bending test of specimens with Atech substrate in various loading configurations and calculated Weibull parameters (characteristic fracture stress and Weibull modulus)	57
Table 17 Results of ring-on-ring bending test of specimen with IEK-1 substrate tested in various loading configurations and calculated Weibull parameters (characteristic fracture stress and Weibull modulus)	59
Table 18 Young's modulus of $\alpha$ -Al <sub>2</sub> O <sub>3</sub> [142].	64
Table 19 Characteristic fracture stresses, Weibull moduli and Young's moduli for Atech and IEK-1 substrates.	66
Table 20 Comparison of the mechanical properties of the different substrate materials	70
Table 21 Young's modulus and deformation of various specimens.	73
Table 22 Load and deformation of completely coated specimens during bending test (coating system on tensile side)	78
Table 23 Selectivities of CO <sub>2</sub> /N <sub>2</sub> at different temperatures (selectivity of ideal Knudsen gas transport is 0.8).	79
Table 24 Permeation of He, CO <sub>2</sub> and N <sub>2</sub> as single gas through silica membrane on Atech substrate ( $\Delta p=2$ bar).	80
Table 25 Permeation of He, CO <sub>2</sub> and N <sub>2</sub> as single gas through the silica membrane on IEK-1 substrate.	81
Table 26 Selectivity of silica membrane on IEK-1 substrate for gas separation He/CO <sub>2</sub> , He/N <sub>2</sub> and CO <sub>2</sub> /N <sub>2</sub> .	82
Table 27 Permeances of H <sub>2</sub> , CO <sub>2</sub> , N <sub>2</sub> , in the single gas tests at 220 °C [158].	82
Table 28 Permeation rates of helium, CO <sub>2</sub> and N <sub>2</sub> and selectivities of He/CO <sub>2</sub> , He/N <sub>2</sub> and CO <sub>2</sub> /N <sub>2</sub> through uncoated IEK-1 substrate at T = 25 °C and $\Delta p = 1$ bar.	84
Table 29 Permeation trend with increasing temperature (mol·s <sup>-1</sup> ·m <sup>-2</sup> ·Pa <sup>-1</sup> / K·10 <sup>-9</sup> ).	88

Table 30 Partial pressure of water vapour in gas mixture (condensation pressure of water vapour 1.01 bar at 100 °C).....	90
Table 31 Partial pressure of water vapour in gas mixture (condensation pressure of water vapour is 2.7 bar at 130 °C) .....	96
Table 32 Permeation of He, CO <sub>2</sub> und N <sub>2</sub> as single gas through silica membrane on ITM porous metal substrate and the selectivity of silica membrane for gas separation CO <sub>2</sub> /N <sub>2</sub> , without pre-deformation .....	99
Table 33 Permeation of He, CO <sub>2</sub> und N <sub>2</sub> as single gas through silica membrane on ITM porous metal substrate and the selectivity of silica membrane for gas separation CO <sub>2</sub> /N <sub>2</sub> , with pre-deformation .....	100

## Acknowledgements

First of all, I would like to express my gratitude to Univ. Prof. Dr.-Ing. Lorenz Singheiser for providing me this opportunity to accomplish my PhD thesis in the institute for Energy and Climate Research (IEK-2) of Forschungszentrum Jülich.

I would also like to thank my initial supervisors Univ. Prof. Dr.-Ing. Tilmann Beck and Prof. Dr. Torsten Markus for their guidance and suggestions.

My sincere thanks are given to my supervisor Dr. Jürgen Malzbender for his kind support and patient guidance to my work. Without his help it would be impossible for me to finish this doctoral thesis.

Additionally, I appreciate sincerely the help from project partners: PD Dr. Martin Bram, Dr. Corinna Reetz and Dr. Jan Eiberger in IEK-1 for their supply of specimens; Mr. Jürgen Collienne and Mr. Klaus-Peter Hollfeld for their construction and modification of permeation instruments.

I am very thankful to the institute colleagues without the support of whom the work could not be done only by myself: Dr. Egbert Wessel and Dr. Daniel Grüner for the SEM analysis; Mr. Volker Gutzeit and Mr. Jörg Bartsch for the metallographic investigations; Mr. Josef Mönch, Ms. Tatjana Osipova, Mr. Ralf Küppers and Dr. Goran Pećanac for the mechanical testing; Mr. Max Borzиков for the annealing tests.

I am also very grateful to my group colleagues Dr. David Henriques and Mr. Florian Thaler who have provided me significantly scientific support.

Last my thanks would go to my beloved wife for her continuous support and encouragement to my work and life throughout these years.



Band / Volume 298

**12th Carolus Magnus Summer School on  
Plasma and Fusion Energy Physics**

edited by Kristel Crombé (2015), 468 pp  
ISBN: 978-3-95806-107-1

Band / Volume 299

**Optical near-field investigations of photonic structures  
for application in silicon-based thin-film solar cells**

A. M. Ermes (2015), vi, 157 pp  
ISBN: 978-3-95806-108-8

Band / Volume 300

**Strom- und Gasmaktdesign zur Versorgung  
des deutschen Straßenverkehrs mit Wasserstoff**

M. Robinius (2015), VI, 255 pp  
ISBN: 978-3-95806-110-1

Band / Volume 301

**Alterung von Vakuum-plasmagespritzten MCrAlY-Schutzschichten  
und ihre Wechselwirkung mit Nickel- und Cobalt-basierten  
 $\gamma/\gamma'$ -Superlegierungen**

P. J. Terberger (2015), IX, 149 pp  
ISBN: 978-3-95806-113-2

Band / Volume 302

**Verbundvorhaben ELFA Effiziente Luftfahrzeuge**

Brennstoffzellensysteme zur Energieerzeugung BREZEN –  
Teilprojekt: Kerosinaufbereitung

R. Peters, J. Meißner, J. Pasel, R. C. Samsun, D. Stolten  
(2016), viii, 84 pp  
ISBN: 978-3-95806-114-9

Band / Volume 303

**Cavity-Ringdown-Spektroskopie zur Untersuchung der Rolle  
höherer Stickoxide für den nächtlichen Schadstoffabbau in der  
unteren Atmosphäre**

S. Schrade (2016), II, 118 pp  
ISBN: 978-3-95806-116-3

Band / Volume 304

**Thermo-mechanical Properties of Mixed Ionic-Electronic  
Conducting Membranes for Gas Separation**

V. K. Stournari (2016), 167 pp  
ISBN: 978-3-95806-117-0

Band / Volume 305

**Untersuchungen zu suspensionsplasmagespritzten  
Wärmedämmschichtsystemen**

N. Schlegel (2016), X, 136 pp  
ISBN: 978-3-95806-118-7

Band / Volume 306

**Laser processing for the integrated series connection  
of thin-film silicon solar cells**

B. Turan (2016), xii, 188 pp  
ISBN: 978-3-95806-119-4

Band / Volume 307

**Development and Application of a Multiscale Model  
for the magnetic Fusion Edge Plasma Region**

F. Hasenbeck (2016), 190 pp  
ISBN: 978-3-95806-120-0

Band / Volume 308

**Emissions of Biogenic Volatile Organic Compounds and  
Ozone Balance under Future Climate Conditions**

C. Wu (2016), VI, 105 pp  
ISBN: 978-3-95806-121-7

Band / Volume 309

**Computerunterstützte Auslegung eines Brennstoffzellen-Batterie-  
Hybridsystems für die Bordstromversorgung**

C. Krupp (2016), iii, 207 pp  
ISBN: 978-3-95806-124-8

Band / Volume 310

**Influence of H<sub>2</sub>O, HCl and H<sub>2</sub>S on the Release and  
Condensation of Trace Metals in Gasification**

M. Benito Abascal (2016), XIX, 172 pp  
ISBN: 978-3-95806-125-5

Band / Volume 311

**Mechanical and Thermochemical Properties of Nano-structured  
Membranes for Gas Separation in Fossil-fired Power Plants**

J. Zhang (2016), II, 134 pp  
ISBN: 978-3-95806-126-2



**Energie & Umwelt /  
Energy & Environment  
Band / Volume 311  
ISBN 978-3-95806-126-2**

